UNIVERSITY OF CALIFORNIA
Los Angeles

Interactions of Relativistic Electrons with Relativistic Plasma Waves

A dissertation submitted in partial satisfaction of the
requirements for the degree Doctor of Philosophy
in Physics

by

Ronald Leslie Williams

1992

The dissertation of Ronald Leslie Williams is approved.

Francis F. Chen

Walter N. Gekelman

Charles Kennel

Chan Joshi, Committee Co-Chair

John M. Dawson, Committee Co-Chair

University of California, Los Angeles

1992

To M. Lucile Williams and Roselyn E. Williams

Contents

List of Figures

List of Tables

ACKNOWLEDGEMENTS

I would like to thank my research advisor, Professor Chan Joshi, for his support, guidance, and encouragement and for teaching me how to do research. I would like to thank Professor John Dawson for starting me in this research direction, for many insightful discussions, and for his guidance and support from beginning to end. I thank Tom Katsouleas for the many lively discussions on the theoretical and computational aspects of these projects and I thank Chris Clayton for the many frank discussions on the experimental aspect of these projects; I enjoyed and appreciate their close collaboration. I thank Professor Frank Chen for the insight I gained from him, especially during thought provoking group seminars. I thank Professor Charles Kennel and Professor Walter Gekelman for their support and interest in my work.I thank Warren Mori for the many helpful ideas on the beat wave accelerator and plasma undulator, and David Whittum for critically reviewing my work on the plasma lens. I thank all the research and staff members of the Laser Plasma Group for their valuable contributions to this work; especially Mrs. Maria Guerrero for her cheerful and professional administrative support. I thank my many friends and fellow graduate students who helped to make this experience enjoyable, and I thank my many family members for the sacrifices, support and encouragement which made this effort possible.

VITA

March 11, 1947	Born, Tallahassee, Florida
1969	B.S., Engineering Science Florida State University
1969-1974	Engineer Department of the Navy
1974-1978	Research Assistant Cornell University
1978	M.S., Electrical Engineering Cornell University
1978-80	Member of the Technical Staff Hughes Research Laboratories
1980-92	Research/Teaching Assistant University of California, Los Angeles
1983	M.S., Physics University of California, Los Angeles

PUBLICATIONS

R. L. Williams, C. E. Clayton, C. Joshi, and T. Katsouleas. The Motion of Relativistic Electrons Through Transverse Relativistic Plasma Waves. *Rev. Sci. Instrum.*, **61 (10)**, 3037 (1990).

R. L. Williams, C. E. Clayton, C. Joshi, T. Katsouleas, and W. B. Mori. Relativistic Wave-Particle Interactions in the Plasma Beatwave Accelerator. *Laser and Particle Beams,* **8 (3)**, 427-449 (1990).

R. L. Williams, C. E. Clayton, C. Joshi, T. C. Katsouleas and W. B. Mori. Theory and Experiments on the Generation of Spontaneous Emission using a Plasma Wave Undulator: A Progress Report. *SPIE Proc. on Free-Electron Lasers and Applications,* Series P, Edited by D. Prosnitz, bf Vol. 1227, 48 (1990).

T. Katsouleas and R. Williams. Studies of Beam Spot Size Compression in an Adiabatic Plasma Lens. *Proc. U.S./Japan Workshop on Non-Linear Beam Dynamics and Accelerator Mechanisms,* Tsukuba, Japan, Oct. 21-24, 1990.

C. Clayton, C. Joshi, W. Leemans, K. Marsh and R. Williams. Beat Wave Development Work. In Advanced Accelerator Concepts, *AIP Conference Proceedings No. 193* edited by C. Joshi (AIP, New York, 1985), p. 130.

C. Joshi, C. E. Clayton, K. Marsh, R. Williams, W. Leemans and M. T. Shu. Test Particle Injection in Relativistic Plasma Waves Driven by Two Co-Propagating Laser Beams. *SPIE Symposium on O.E. Lase 1988,* Jan. 10-17, 1988, Anaheim, CA.

C. E. Clayton, C. Joshi, W. P. Leemans, K. A. Marsh, M. T. Shu and R. L. Williams. Get Title. *Proc. of 1988 Linear Accelerator Conference,* Oct. 3-7, 1988, Williamsburg, VA.

D. Umstadter, R. Williams, C. E. Clayton, and C. Joshi. Observation of Steepening in Electron Plasma Waves Driven by Stimulated Raman Scattering. *Phys. Rev. Letter,* **59**, 292-295 (1987).

C. Joshi, C. E. Clayton, K. Marsh, R. Williams and W. Leemans. Experimental Work at UCLA on the Plasma Beat Wave Accelerator. Proceedings of Workshop on New Developments in Particle Acceleration Techniques, Orsay, France, July 1987, *CERN Publication 87-11,* Oct. 1987, Vol. 2, p. 351-360.

R. L. Stenzel, R. L. Williams, R. Aguero, K. Kitazaki, A. Ling, T. McDonald and J. Spitzer. Novel Directional Ion Energy Analyzer. *Rev. Sci. Instrum.,* **53(7)**, 1027 (1982).

W. S. Williamson, C. R. Dulgeroff and R. L. Williams. 8-cm Engineering Model Thruster Technology: A Review of Recent Developments. Princeton/AIAA/DGLR *14th International Electric Propulsion Conference,* Princeton, NJ, Oct. 30-Nov. 1, 1979, p. 1.

ABSTRACT OF THE DISSERTATION

Interactions of Relativistic Electrons with Relativistic Plasma Waves

by

Ronald Leslie Williams
Doctor of Philosophy in Physics
University of California, Los Angeles, 1992
Professor John M. Dawson, Co-Chair
Professor Chan Joshi, Co-Chair

The interactions of relativistic electrons with relativistic plasma waves are studied by examining three novel applications: a high gradient particle accelerator, an electron beam diagnostic of relativistic plasma waves, and an undulator for producing coherent short wavelength radiation. The focusing of a high energy particle beam in a ramped density plasma lens for use in future high energy e^+e^- colliders is also examined.

The trapping threshold, energy gain, phase evolution, beam focusing and energy spectrum are found for particles accelerated in the laser plasma beatwave accelerator, plasma wakefield accelerator, and laser wakefield accelerator schemes in which accelerating gradients on the order of 10's to 100's of giga-Volts per meter may exist. The limits due to beam emittance and plamsa wave width are found for the measurement of relativistic plasma wave amplitude and wavelength using a relativistic electron beam as a diagnostic. The short wavelength ($\approx 1\mu$m) coherent spontaneous radiation, particle bunching, stimulated radiation, and radiation gain are found for modest energy electrons (≈ 4 MeV) injected into a 1 cm long, 100 μm period plasma wave undulator which is shown to behave similar to a free electron laser undulator. The compression of high energy beams to very small spot sizes and the reduction in chromatic aberrations in the ramped density plasma lens are found to be sensitive to beam and lens matching which is determined by adjusting the Courant-Snyder accelerator parameters.

Chapter 1

Introduction

Particles can be accelerated over a much shorter distance to high energies in a compact high-gradient plasma wave accelerator than in a vacuum acceleration structure. A particle beam can emit much higher frequency radiation in a compact short period plasma wave undulator than in a vacuum magnetic undulator device. A high energy particle beam can be compressed to a much smaller spot size in a density ramped plasma lens than in a traditional magnetic lens immersed in vacuum. These separate novel concepts of injecting particles into a medium to accelerate them, to make them radiate and to focus them are based on the large amplitude electrostatic fields that can exist in a plasma medium.

The direction of these electrostatic fields can be aligned in a dense plasma by injecting intense electromagnetic (EM) radiation (laser) beams or intense short relativistic particle beams (electron bunches), which results in the excitation of relativistic plasma waves (RPWs). The successful application of RPWs in particle acceleration and radiation generation experiments requires a thorough understanding of the interactions between the particles and waves, which has been the motivation for the work of this dissertation. The plasma lens, although not necessarily based on RPWs, also utilizes the large amplitude fields found in plasmas, and the methods for studying RPW's can be applied to plasma lenses.

The amplitude of the plasma electrostatic field can be estimated using Gauss' law which gives $E = m_o c\omega_p/e \approx \sqrt{n_o}$ Volts/cm, where m_o is the rest mass of the plasma electrons, c is the speed of light, the plasma frequency is $\omega_p = \sqrt{4\pi n_o e^2/m_o}$, and n_o is the background plasma density in cm^{-3}. Plasma densities on the order of 10^{17} to 10^{18} cm^{-3} are typical for the accelerator, undulator and lens applications considered herein. The plasma wave is relativistic because it has a phase velocity approximately equal to the speed of light. The phase velocity of the plasma wave is equal to the group velocity of the EM radiation or particle bunch that excites the wave. In this work, the transients associated with plasma wave growth are assumed to be absent so that the plasma wave amplitude is constant during the time the particles transit through it.

The particles that are injected into either the plasma accelerator, undulator or lens also move at approximately the speed of light and do not have collisions with the background plasma particles. The injected particles are assumed not to interact with each other because they constitute a tenuous beam. The density of the electrons in the bunch is assumed to be less that the density of the background plasma in the plasma accelerator and plasma undulator. The density of the electron bunch is greater than the background plasma density in the plasma lens considered herein, and this is called the underdense plasma lens case. The length of the plasma wave accelerator or undulator considered herein is on the order of one to ten millimeters, so that the time during which the electron is accelerated or radiation is produced is on the order of 3 to 30 picoseconds.

In the plasma wave accelerator, relativistic electrons are injected into, become trapped by and travel in synchronism with the wave while gaining energy from the wave's electrostatic potential at the rate of 10's to 100's of gigaelectronVolts/meter.

The limits for electron trapping and energy gain are presented herein. The plasma wave has a finite width and the effects of the resulting radial fields which provide focusing and defocusing are included. In the numerical simulations, a short beam (bunch) of electrons, with emittance, is injected into the plasma wave at various phases and radial positions in an attempt to approximate experimental conditions and to obtain an energy spectrum of the accelerated electrons. The results are general and apply to most plasma wave acceleration experiments underway around the world, however the parameters of several experiments, in particular the UCLA beatwave experiments, are used as examples.

RPWs have very short wavelengths and high equivalent magnetic fields, typically on the order of 100 μm and one megaGauss, which make them attractive for use as electron undulators. The electrons are injected perpendicular to the plasma wave and its longitudinal electrostatic fields oscillate the electrons back and forth which causes them to radiate electromagnetic waves. The plasma wave used for the undulator is basically the same as the plasma wave used for the accelerator except that it is wider in order that more undulations occur. The resonance condition for free electron lasers also holds for the plasma wave undulator. The wiggle wavelength is equivalent to the plasma wave wavelength so that $\lambda_r = \lambda_w/2\gamma_2 = \lambda_p/2\gamma_2$, where λ_r, λ_w and λ_p are the wavelengths of the radiation, wiggler (or undulator) and plasma wave, respectively, and γ is the relativistic factor of the electron. An advantage of the short wavelength plasma wave undulator is that it would allow a modest energy electron beam, for example tens of MeV, to generate coherent radiation having wavelengths on the order of a few nanometers using a compact apparatus. Normally, very high energy electron beams (GeV range) at large accelerator centers are needed to obtain radiation wavelengths in the nanometer range using longer period magnet undulators.

In order to get coherent radiation from the undulator, the electrons in the bunch need to radiate coherently. The motion of the electron bunch as it passes transversely through the plasma wave is studied in detail in order to see if the electrons get scattered out of the beam by the electrostatic fields. It is found that the longitudinal electrostatic field has a significant spreading effect on the electron bunch but does not disrupt the beam's coherence necessarily. This spreading effect appears after the electron bunch has exited the plasma wave and could be used as a diagnostic of the amplitude and wavelength of the longitudinal plasma wave fields. Limits on the use of the electron bunch as a diagnostic due to beam emittance and plasma wave width are presented. A spatial grating in the electron distribution occurs as the injected electron energy is increased.

The radiation from the electrostatic plasma wave undulator is derived starting from the calculation of the electron trajectories using perturbation techniques. The results can be extended to the *ac* FEL by letting the value of the plasma wave wavevector go to zero. The spontaneous radiation, as a function of angle and frequency, from electrons drifting through the plasma wave is calculated. Then an electromagnetic wave is added which results in electron bunching, stimulated radiation and gain. Approximate analytical results are compared to three dimensional simulations.

In high energy e^+e^- colliders the beams can be injected into plasma lenses which focus the particles to very small spot sizes (submicron dimensions) at the interaction point. Very small spot sizes will be required in future colliders in order to increase the beam luminosity (intensity) and thus the collision rate. The large focusing force in the plasma lens is due to the large ion space-charge electrostatic fields which are exposed when the electron beam expels background electrons from its path. Background electrons are attracted into the positron beam's path, which also results in large focusing fields. The rapid particle focusing in plasma lenses can result in synchrotron radiation emission, energy loss, and thus chromatic aberrations which can put a limit on the minimum spot size attainable. Density ramped plasma lenses in which the beam is gradually squeezed to a small spot size in order to reduce the radiation and aberration problems are examined herein. The rate of spot size compression versus rate of plasma density increase, lens nonuniformity, and beam energy spread is discussed.

In Chapter 2 the plasma wave based particle accelerator is discussed in detail. In Chapter 3 the use of electron bunch spreading as a diagnostic of the plasma wave fields is discussed. In Chapter 4 the radiation from electrons passing through the plasma undulator is discussed. In Chapter 5 the spot size compression of a high energy electron beam passing through a density ramped plasma lens is discussed. In Chapter 6 are the conclusions. Appendix A contains tables of data pertinent to laser plasma beatwave acceleration experiments. In Appendix B are comments on simulations of accelerated electron energy spectra for three types of plasma sources used in the UCLA laser plasma beatwave acceleration experiment. In Appendix C is a description of a sensitive electron energy data acquisition system used in the UCLA laser beatwave acceleration experiments. In Appendix D are comments on the Osaka University plasma beatwave acceleration experiment. In Appendix E is discussed modified simulation results of the UCLA the beatwave acceleration experiment which occurs when the plasma wave has a spatial profile (inhomogeneity) in the longitudinal direction is included in the simulations. In Appendix F is discussed a modification to the plasma undulator results which occur when plasma wave nonlinearities (harmonics) are included in the simulations.

Chapter 2

Studies of Relativistic Wave-Particle Interactions in Plasma-Based Collective Accelerators

2.1 Introduction

Recently, relativistic plasma waves excited by either a laser beam or an electron bunch, have been under intense study because of their potential in accelerating particles at a very rapid rate [1]. Such plasma waves with phase velocities almost equal to that of light form the basis of at least three collective accelerator schemes, each distinguished by the method used for the excitation of such waves. In the plasma beat wave accelerator (PWBA), two parallel laser beams are co-propagated into an underdense plasma [2] [3]. The difference frequency of the lasers is chosen to match the plasma frequency, so that the pondermotive force of the beating pattern resonantly builds up a relativistic plasma wave. Alternatively, intense plasma waves can be excited by using a relativistic electron bunch, since the energy density in existing electron bunches can be comparable to, or exceed that of the most powerful of today's laser beams. In the plasma wake field accelerator (PWFA), a dense compact electron bunch is sent through a high density plasma [4]. The space charge force of such a bunch displaces the plasma electrons and leaves behind a wake of plasma oscillations. The phase velocity of this wake is the same as that of the driving bunch, approximately c. Instead of using an electron bunch, one could use an extremely short but intense laser pulse as in the laser wake field accelerator (LWFA), to excite the plasma wave which will have a phase velocity equal to the group velocity of the intense laser pulse [2] [5] [6].

The maximum accelerating fields of such plasma waves scale as $\sqrt{n_0}$ Volts/cm where n_0 is the plasma density in cm^{-3}. In all three acceleration schemes, PBWA, PWFA and LWFA, the acceleration mechanism is the same. A trailing relativistic electron bunch, appropriately phased in the potential well of the plasma wave, can remain in synchronism with it for a long time and be accelerated. Experiments are being carried out at UCLA [7] [8], Rutherford Appleton Laboratory (RAL, United Kingdom [9]), Institute of Laser Engineering (ILE, Japan [10]), Ecole Polytechnique (EC, France [11]), INRS (Canada [12]), and Atomic Energy of Canada Limited (AECL, Canada [13]) on the reproducible excitation of such plasma waves using the beat wave technique and on the controlled acceleration of injected particles. Experiments at Argonne National Laboratory [14] have clearly demonstrated the excitation of the plasma wake fields using an electron bunch while a similar experiment is underway at KEK (Japan [15]). An experiment on the LWFA is being planned at the Lawrence Livermore National Laboratory (LLNL [16]).

The work of this chapter is motivated by a flurry of experimental activity in the area of plasma based collective accelerators. We present one-, two- and three-dimensional studies of relativistic wave particle dynamics to illustrate both the details of the acceleration mechanism, and to estimate the energy spectra of accelerated electrons. Whenever possible, we take UCLA and RAL experiments as examples. We note that one dimensional simulations of single frequency and beat wave heating have previously been carried out using a Vlasov code [17] and also one and two dimensional simulations of beat heating have been carried out using a particle in cell code [18]. This work differs from previous works in that here we concentrate on dynamics of externally injected rather than self-trapped particles.

2.2 One Dimensional Model of Particle Acceleration by Plasma Waves

The main features of the acceleration process can be illustrated using a simple one-dimensional (1-D) sinusoidal plasma wave model and by solving for the electron motion in the rest frame of the wave. We define zero phase at the potential minimum of the wave in the wave frame. For reference, figure 2.1 is an idealization of a particle in the potential of the wave as seen in the wave frame, and also defines the location of zero phase. An electron that moves or slips in the negative phase direction (i.e., has a negative wave frame velocity as shown by the arrow in figure 2.1 has a lab frame velocity that is less than the wave's phase velocity and the opposite is true for electrons moving in the positive phase direction.

We treat the plasma wave as being linear (no significant harmonic components) and unaffected by the injected particles. This is appropriate in the limit of small wave amplitudes and small number of injected electrons such that beam loading effects can be neglected [19]. These assumptions are valid for all the current experiments. Consider for instance the UCLA beat wave acceleration experiment. The fractional plasma wave amplitude is $\epsilon \leq 0.10$, so we can assume a sinusoidal wave. (The fractional plasma wave amplitude, or fractional density modulation, is

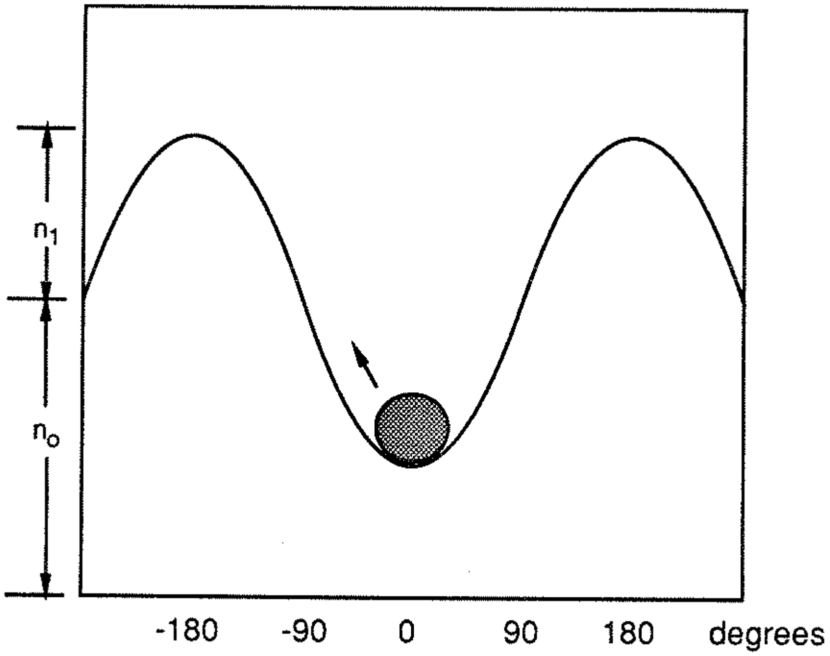

Figure 2.1: Idealization of 1-D plasma wave potential and electron in the wave frame. Fractional plasma wave amplitude is $\epsilon = n_1/n_0$.

$\epsilon = n_1/n_0$, where n_1 is the density fluctuation of the wave and n_0 is the background plasma density, as shown in figure 2.1.) Also, the number of injected electrons is less than 10^6 which is much smaller than the 1-D beam loading limit given by $N \approx 5 \times 10^5 \epsilon \sqrt{n_0} A \approx 10^8$ where A is the plasma wave cross sectional area (cm^2) and $\epsilon = 5\%$.

We first examine limits on the energy of electrons trapped in a plasma wave potential and then solve the 1-D relativistic equation of motion to obtain the variation of electron energy between the limits. These results are general, however we take particular examples of the PBWA experiments at UCLA which use a CO_2 laser which can lase on several different wavelength combinations and at RAL which use a Nd:glass laser. The plasma wave has a relativistic Lorentz factor, γ_p, which is related to its phase velocity, v_p, by

$$\gamma_p = \sqrt{1 - \frac{v_p^2}{c^2}} \quad \text{and} \quad \frac{v_p}{c} = \sqrt{1 - \frac{\omega_p^2}{\omega^2}} = \beta_p \tag{2.1}$$

and ω_p is the plasma frequency and ω is the laser frequency. In one of the UCLA experiments, the 9.6 μm and 10.27 μm lines of a CO_2 laser are used to excite a plasma wave which has γ_p equal to 13.7, whereas in the RAL experiment, the 1.05 μm and 1.06 μm lines of Nd:YLF and Nd:YAG oscillators are used to excite a wave having γ_p equal to 94.5. Table A.1 of Appendix A is a list of lasers currently used in beatwave acceleration experiments. Table A.2 is a comparison of beatwave accelerator properties. Appendices B and E contain comments on another UCLA beatwave experiment in which γ_p equals 9.7. Appendix D contains comments on the Osaka University experiment in which γ_p equals 9.7 also.

The energy of the injected electron is γ_o in the lab frame and is $\gamma' = \gamma_p\gamma_o(1 - \beta_p\beta_o)$ in the wave frame where β_p and β_o are the lab frame velocities of the wave and electron normalized to c, respectively. (Primed quantities are wave frame quantities.) The wave frame "trapping condition" is that the electron's kinetic energy must be less than the potential energy of the wave or $(\gamma' - 1)m_oc^2 \leq e\phi'$, where m_o is the electron rest mass, e is the electron charge and ϕ' is the potential of the wave in the wave frame [20]. The lab frame trapping condition is obtained by writing ϕ' in terms of lab frame quantities and using the invariance of the plasma wave's longitudinal field, $\overline{E}' = \overline{E}$, the transformation of the longitudinal wave vector, $\overline{k} = \overline{k}'\gamma_p$, and the transformation of the energy from the wave frame back to the lab frame, $\gamma = \gamma_o\gamma'(1 + \beta_p\beta')$. We then obtain the minimum and maximum lab frame energies for an electron trapped in the plasma wave:

$$\gamma_{min} = \gamma_p(1 + \Gamma\epsilon\gamma_p\beta_p^2)\left\{1 - \beta_p\sqrt{1 - \frac{1}{(1 + \Gamma\epsilon\gamma_p\beta_p^2)^2}}\right\} \tag{2.2}$$

$$\gamma_{max} = \gamma_p(1 + \Gamma\epsilon\gamma_p\beta_p^2)\left\{1 + \beta_p\sqrt{1 - \frac{1}{(1 + \Gamma\epsilon\gamma_p\beta_p^2)^2}}\right\} \tag{2.3}$$

where $\Gamma = (1 + \cos\theta_o)$ and θ_o is the phase at which the electron is injected into the plasma wave. Figure 2.2(a) is a plot of γ_{min} and γ_{max} versus fractional plasma wave amplitude for different values of γ_p, corresponding to the experiments considered. In plotting these curves we have assumed that the electron is injected at $\theta_o = 0$ or the potential minimum of the wave for electrons. In a plasma wave of amplitude ϵ, a trapped electron will have an energy between the upper (γ_{max}) and lower (γ_{min}) curves. The monotonically decreasing curves, γ_{min}, are the minimum thresholds for trapping of electrons by a plasma wave of a certain amplitude, ϵ. Electrons having energies less than γ_{min} will slip backward out of the wave's potential well and are not trapped. For fractional plasma wave amplitudes greater than about $\epsilon = 10\%$, the trapping thresholds do not vary much for plasma waves having γ_p's that differ by almost an order of magnitude. The increasing curves, γ_{max}, are the maximum energies an electron can have in a plasma wave of a given amplitude. Electrons having energies greater than γ_{max} will slip forward out of the potential well and are not trapped. Approximations to equations 2.2 and 2.3 for $\epsilon \geq 0.01$, $\beta = 1$, and $\theta < 180$ degrees are

$$\gamma_{min} \approx \frac{\gamma_p}{2\,(1 + \Gamma\epsilon\gamma_p)} \tag{2.4}$$

$$\gamma_{max} \approx \gamma_p\left[2\,(1 + \Gamma\epsilon\gamma_p) - \frac{1}{2(1 + \Gamma\epsilon\gamma_p)}\right]. \tag{2.5}$$

For $\epsilon \geq 4\%$, the second term in γ_{max} can be ignored.

Figure 2.2(b) is a plot of γ_{min} and γ_{max} versus ϵ for three sample values of θ_o, and illustrates the variation in energy for an electron injected and extracted at different phases in the potential well moving with a $\gamma_p = 13.7$. As expected, the family of curves for γ_{min} (the lower curves) shows that an electron injected at the wave's potential minimum ($\theta = 0$) has the lowest trapping threshold energy compared to an electron injected at any other phase in the potential well. This is because the wave potential available for trapping must be greater than the electron's kinetic energy in the wave frame. If the electron is injected at positions that are higher in the well where the potential available for trapping is less, the electron's wave frame kinetic energy must be less for it to be trapped. This reduction in wave frame kinetic energy transforms to an increase in lab frame kinetic energy for trapping to occur. This assumes that the electrons are injected with γ_o less than the plasma wave's γ_p.

The family of curves for γ_{max} (the upper curves in figure 2.2(b)) shows that an electron extracted at the wave's potential minimum ($\theta = 0$) reaches a higher energy than an electron extracted at any other phase in the potential well. For cases in which the electron stops being accelerated before reaching the potential minimum (or after slipping beyond the minimum), the final energy actually attained depends on the amount of net potential through which it has fallen in the wave frame.

The maximum energy gained by an electron having an arbitrary injection energy in a given plasma wave is not the maximum possible energy attained by an electron in that plasma wave. The maximum possible energy is gained only by the electron that is injected having the minimum trapping threshold energy. This is because the electron at the minimum threshold energy slips backward in the waveframe all the way to the peak of the potential and can then gain kinetic energy corresponding to the height of the potential well. Other electrons are turned around sooner and

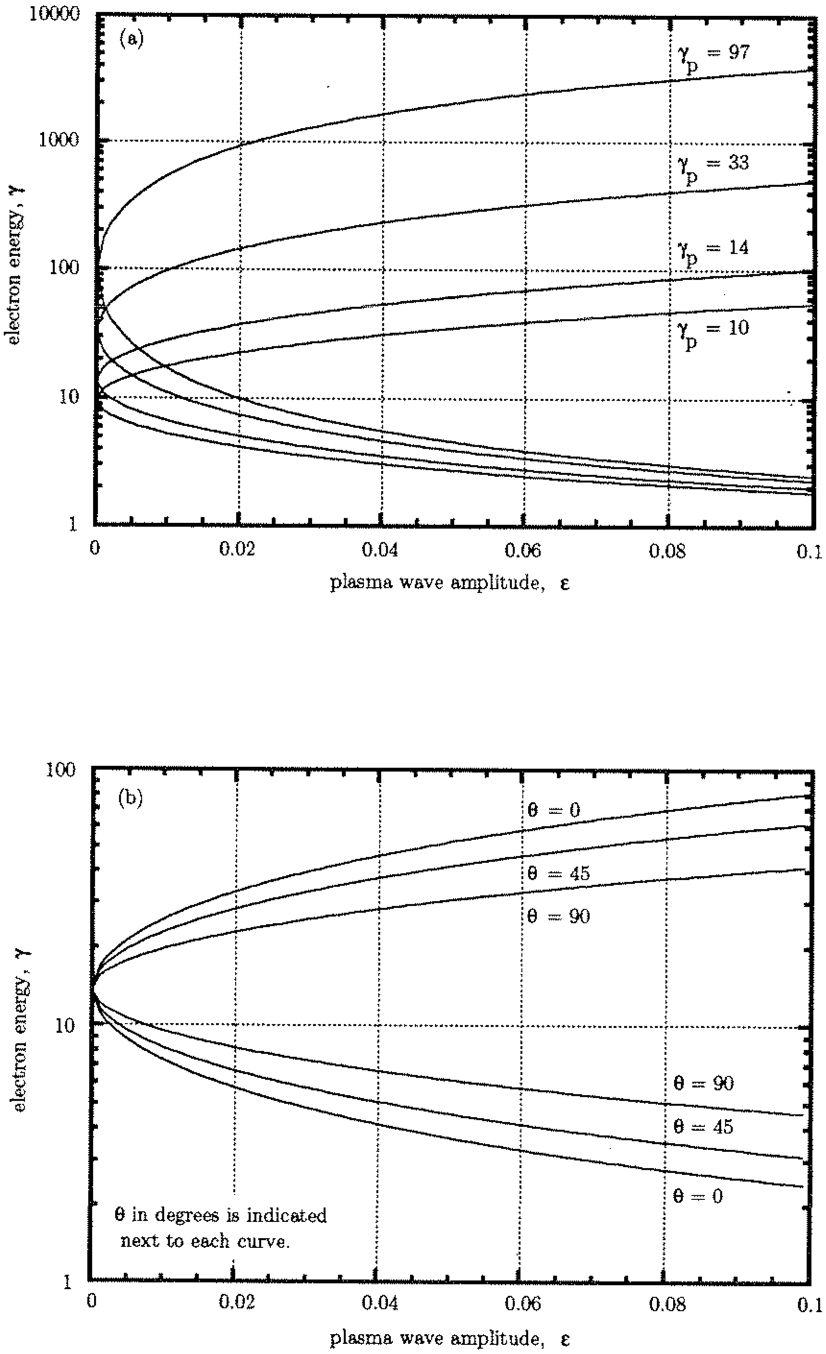

Figure 2.2: Electron trapping threshold and maximum energy for (a) four values of gamma phase, γ_p, and (b) three values of injection and extraction phases, θ.

therefore do not slide down the full potential well. In order to find the maximum energy attained by an electron having an arbitrary initial lab frame energy, we transform the arbitrary lab energy to the wave frame, add the maximum energy the electron gains from the wave, and transform this back to the lab frame. We obtain

$$\gamma = \gamma_p \left[\gamma_p \gamma_o (1 - \beta_p \beta_o) + \Gamma \epsilon \gamma_p \beta_p^2\right] \left\{ 1 + \beta_p \sqrt{1 - \frac{1}{(\gamma_p \gamma_o (1 - \beta_p \beta_o) + \Gamma \epsilon \gamma_p \beta_p^2)^2}} \right\} \tag{2.6}$$

which depends on the electron injection energy, γ_o, and is plotted versus ϵ in figure 2.3(a), along with a plot of γ_{max}, for injection at $\theta_o = 0$. The maximum energy the electron gains from the wave, as used in the above, was found by injecting the electron at $\theta_o = 0$ and calculating its final energy after being trapped and upon returning to $\theta = 0$. As the energy of the injected electron increases, the maximum energy attained decreases for trapped electrons, and the amplitude of the plasma wave required to trap that electron decreases.

We can approximate equation 2.6, in the limits $\epsilon \geq 1\%$, $\beta \approx 1$ and $\theta < 180\,\text{deg}$, for trapped electrons by

$$\gamma \approx \gamma_p \left[\left(\frac{\gamma_o}{\gamma_p} + \frac{\gamma_p}{\gamma_o} + 2(1 + \cos\theta)\epsilon\gamma_p \right) - \frac{1}{\left(\frac{\gamma_o}{\gamma_p} + \frac{\gamma_p}{\gamma_o} + 2(1 + \cos\theta)\epsilon\gamma_p \right)} \right] \tag{2.7}$$

and for untrapped electrons by

$$\gamma \approx \frac{\gamma_p}{\left(\frac{\gamma_o}{\gamma_p} + \frac{\gamma_p}{\gamma_o} - 2(1 + \cos\theta)\epsilon\gamma_p \right)}. \tag{2.8}$$

With the approximations $\gamma_p \gg 1$ and $\theta_o = 0$, we obtain the usual expression $\gamma \approx \gamma_o + 4\epsilon\gamma_p^2$ for energy gained by the trapped electrons.

The lower branches of the family of curves in figure 2.3(a) show that electrons can gain small amounts of energy although they are not trapped. This is because they are slowed down a little by the potential in the wave frame before slipping backwards out of the potential well. This decrease in backward velocity in the wave frame transforms to energy gain in the laboratory frame. The maximum energy that an untrapped, and below injection threshold, electron can ever attain corresponds to γ_p. That is, if the electron just reaches the rim of the potential well and comes to rest there with zero kinetic energy, then its energy in the laboratory frame is γ_p. However, if the electron is attracted back into the well, then it is trapped and the energy gain jumps to a maximum value given by γ_{max}, and this is the jump in energy shown in figure 2.3(a).

Figure 2.3(b) shows the maximum electron energy attainable versus ϵ for electrons having the same injection energy, but injected at three different phases in a plasma wave having $\gamma_p = 13.7$. This figure shows that the magnitude of the plasma wave required for trapping and the maximum energy a trapped electron can attain both increase as the injection phase increases away from $\theta_o = 0$. Also, the maximum energy attainable by an electron increases with fractional plasma wave amplitude when the electron is injected at a position that is above the potential minimum, i.e. for cases in which $\theta_o \neq 0$ the energy curves have positive slopes as shown by the 45 and 90 degree examples. The reason for this is that the maximum possible kinetic energy is attained when the electron reaches the potential minimum while moving forward in the wave. Therefore in this case an electron injected at the potential minimum must return to its initial position at the potential minimum for all amplitudes of trappable plasma waves. But an electron injected at a position above the potential minimum must return to its initial position plus slip through an additional potential to reach the potential minimum and thus attain its maximum possible energy. This amount of additional potential through which the electron must fall to reach the potential minimum varies with the amplitude of the plasma wave, and accounts for the increase in maximum electron energy with increasing fractional plasma wave amplitude for electrons injected above $\theta_o = 0$. For similar reasons, the slope of the energy curve increases as the injection phase increases away from $\theta_o = 0$.

In order to find the electron energy actually attained for the case in which the electron is accelerated for an arbitrary time and may be injected and extracted at arbitrary phases, we solve the single electron relativistic equation of motion.

$$\frac{dP}{dt} = \frac{d\gamma m_o v}{dt} = eE \sin\left(k_p z - \omega_p t + \theta_o\right) \tag{2.9}$$

where

$$\gamma = \frac{1}{\sqrt{1 - \frac{v^2}{c^2}}} \tag{2.10}$$

$P =$ electron's momentum

$v =$ electron's velocity

$z, t =$ wave propagation direction, time

$k_p =$ plasma wave number

$\theta_o =$ initial phase.

The equation of motion can be rewritten in terms of coupled equations for the lab frame energy, γ, and wave frame phase, ξ, as follows and solved numerically [21].

$$\frac{d\gamma}{dt} = \frac{eE}{m_o c}\sqrt{1 - \frac{1}{\gamma^2}}\ \sin(\xi + \theta) \tag{2.11}$$

ONEIS

$$\frac{d\xi}{dt} = ck_p\sqrt{1 - \frac{1}{\gamma^2}} - \omega_p \tag{2.12}$$

$F(\gamma)$

$g(\xi)$

$\xi = k_p z - \omega_p t$

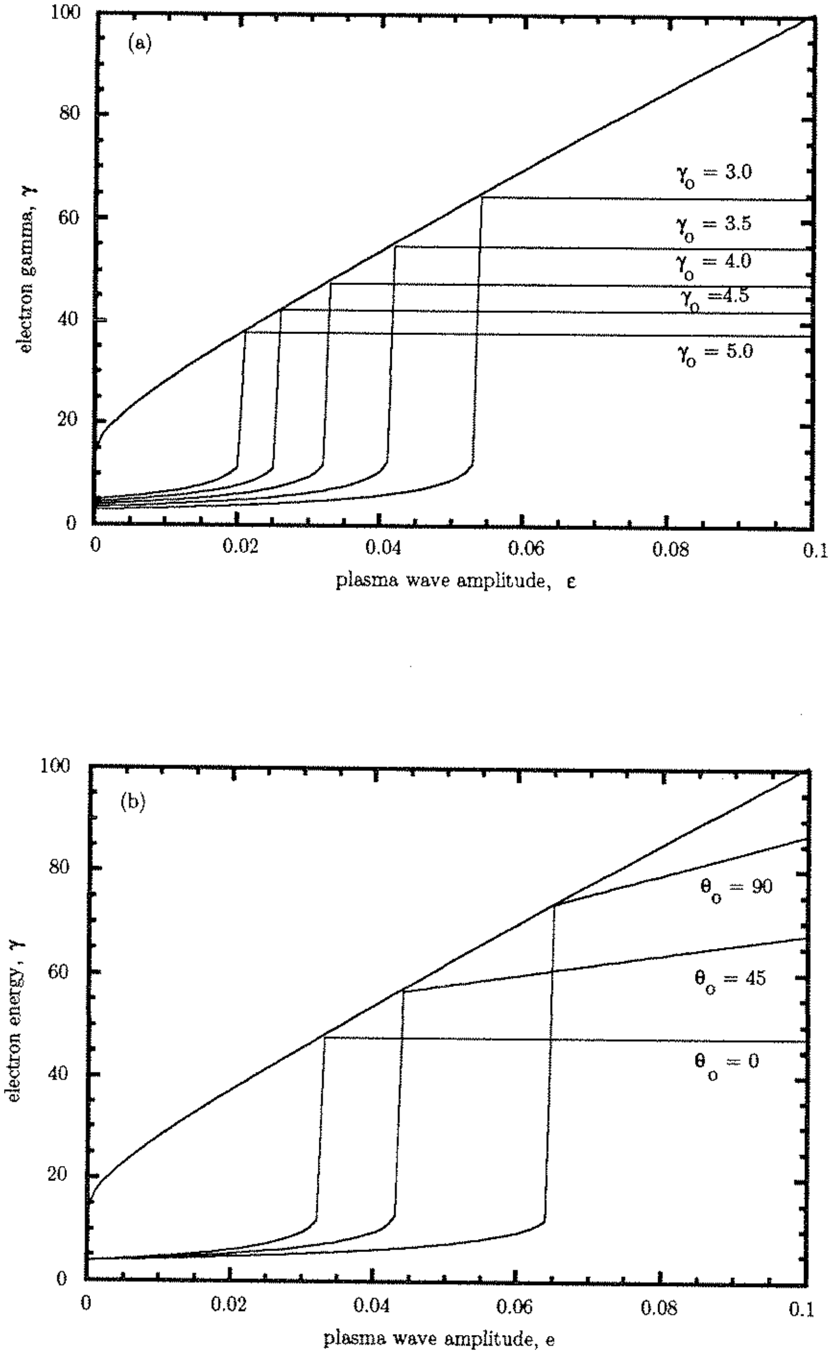

Figure 2.3: Accelerated electron energies for (a) five different injection energies and (b) three different injection phases.

$$\xi = k_p z - \omega_p t. \tag{2.13}$$

The solutions to equations 2.11 and 2.12 are shown in figure 2.4, which is a plot of γ versus ξ for two trapped and two untrapped electrons that are injected at $\theta_o = 0$ into a plasma wave having $\gamma_p = 13.7$. In order to examine the general case, the values selected for the electron's γ_o are greater than and less than γ_p, and are arbitrary except that $\gamma_o = 4$ is the energy of electrons injected in the UCLA experiments [7][8]. In order to exhibit the evolution of the orbits in time, the thick lined portions of the curves represent the progression of the electrons up to the time they are extracted, which is 75 plasma wave periods ($2\pi/\omega_p$ and which corresponds to a 1 cm (462 c/ω_p) acceleration length for this case. The thin lined portions of the orbits represent the continuation of the orbits for a time of 365 plasma wave periods, which is approximately the time for the $\gamma_o = 4$ electron to complete one closed orbit. This line convention is followed also in figures 2.5(a) and 2.5(b). The outer closed orbit is that of a trapped electron having initial energy γ_o less than γ_p, and the inner closed orbit is that of an electron having γ_o greater than γ_p. The orbit for the electron having γ_o equal to γ_p is a point in the center of the closed orbits, i.e., that electron neither gains nor loses energy when it is injected at $\theta_o = 0$. The upper and lower passing orbits are for untrapped electrons having γ_o greater than γ_{max} and less than γ_{min}, respectively.

On the outer closed orbit in figure 2.4, the electron starts at $\theta_o = 0$ at the potential minimum upon injection. Then it slips swiftly backwards in phase (toward negative phase) gaining only a small amount of energy until it is reflected at the turning point and is trapped. This turning point occurs after about 3 to 4 mm (139 to 185 c/ω_p) of acceleration distance in the lab frame for this example. The electron then slips forward in phase slowly and continues to gain energy until it reaches a

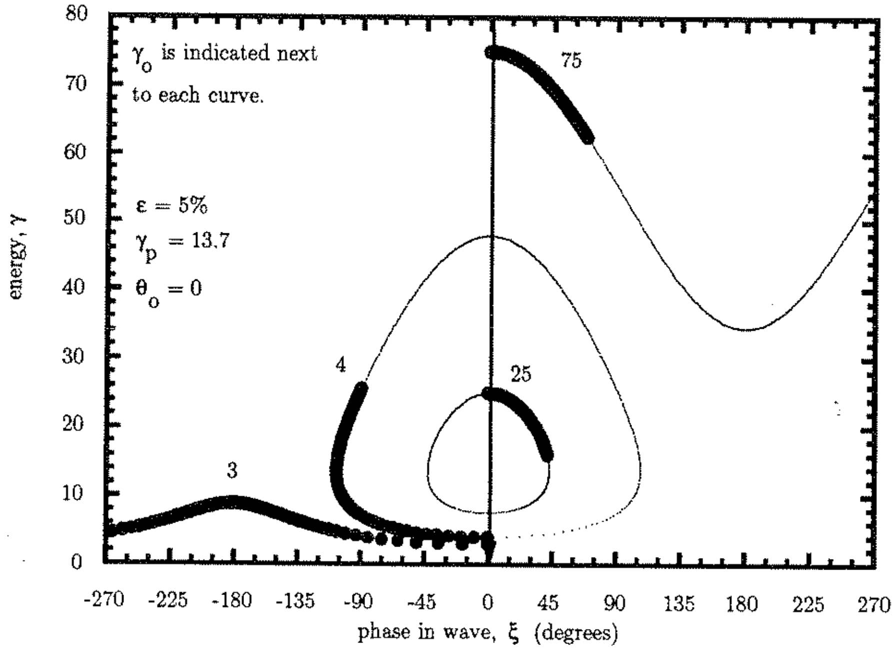

Figure 2.4: Variation of lab frame energy with wave frame phase for two trapped electrons ($\gamma_0 = 4$ and 25) and two untrapped electrons ($\gamma_0 = 3$ and 75).

maximum energy at the extraction phase (thick line). For a longer acceleration distance (thin line) an electron would continue gaining energy until it reached the maximum, corresponding to being at the potential minimum and having a positive velocity in the wave frame. As the electron climbs up the other side of the well, it has positive phase relative to the wave's minimum and experiences a decelerating field, loses energy, and reverses its direction at the turning point. It loses more energy as it returns to its initial $\theta = 0$ injection point where its lab frame kinetic energy is a minimum, corresponding to being at the potential minimum and having a negative velocity in the wave frame. The explanation of the inner closed orbit is similar to the above, except that the electron initially slips forward in phase while losing energy.

Figure 2.5(a) is a plot of the electron's lab frame energy (γ) versus acceleration distance for the two trapped and two untrapped electrons which differ according to γ_o. Figure 2.5(a) is figure 2.4 plotted versus z instead of ξ, using equation 2.13. The figure shows that as an electron's γ_o approaches the wave's γ_p, the maximum energy gained decreases and the time to reach maximum energy decreases. Also shown is that the electron gains approximately 25 MeV in about 2.5 cm, or a gain of 1 GeV per meter.

Figure 2.5(b) is a plot of wave frame phase, ξ, versus acceleration distance, z, for the same four electrons, and shows that the deeply trapped electron, $\gamma_o = 4$ in this case, spends most of the time moving forward between turning points. Comparison of figures 2.5(a) and 2.5(b) shows that energy gain occurs only when the trapped electrons are in the wave's negative phase region.

The transition of the electron trajectories in phase space from being untrapped to trapped as the injection energy increases is shown in figure 2.6, in which the injection energy is varied in small increments. Clearly, the $\gamma_o = 3.0$ electron is untrapped as seen from its passing or sinusoidal orbit whereas the $\gamma_o = 3.2$ electron is just trapped, and the phase space separatrix occurs between the two. This is in agreement with the energy gain vs fractional plasma wave amplitude curve shown in figure 2.3(a) for the case of $\epsilon = 5\%$.

Figure 2.7 is a comparison of phase space trajectories for a single electron ($\gamma_o = 4$ and $\theta_o = 0$) when it is not trapped by a small plasma wave having $\epsilon = 3\%$ and when it is trapped by larger plasma waves having $\epsilon = 5\%$ and 10%. This shows that the two larger plasma waves will accelerate the electron to the same maximum energy, and that as the plasma wave amplitude increases, the phase excursion decreases as expected. However, the 10% wave will accelerate the electron to the maximum energy in about half the acceleration distance as the 5% wave since the r.m.s. accelerating field for the 10% wave is that much higher than the 5% wave.

Figure 2.8 is a comparison of phase space trajectories for a single electron that

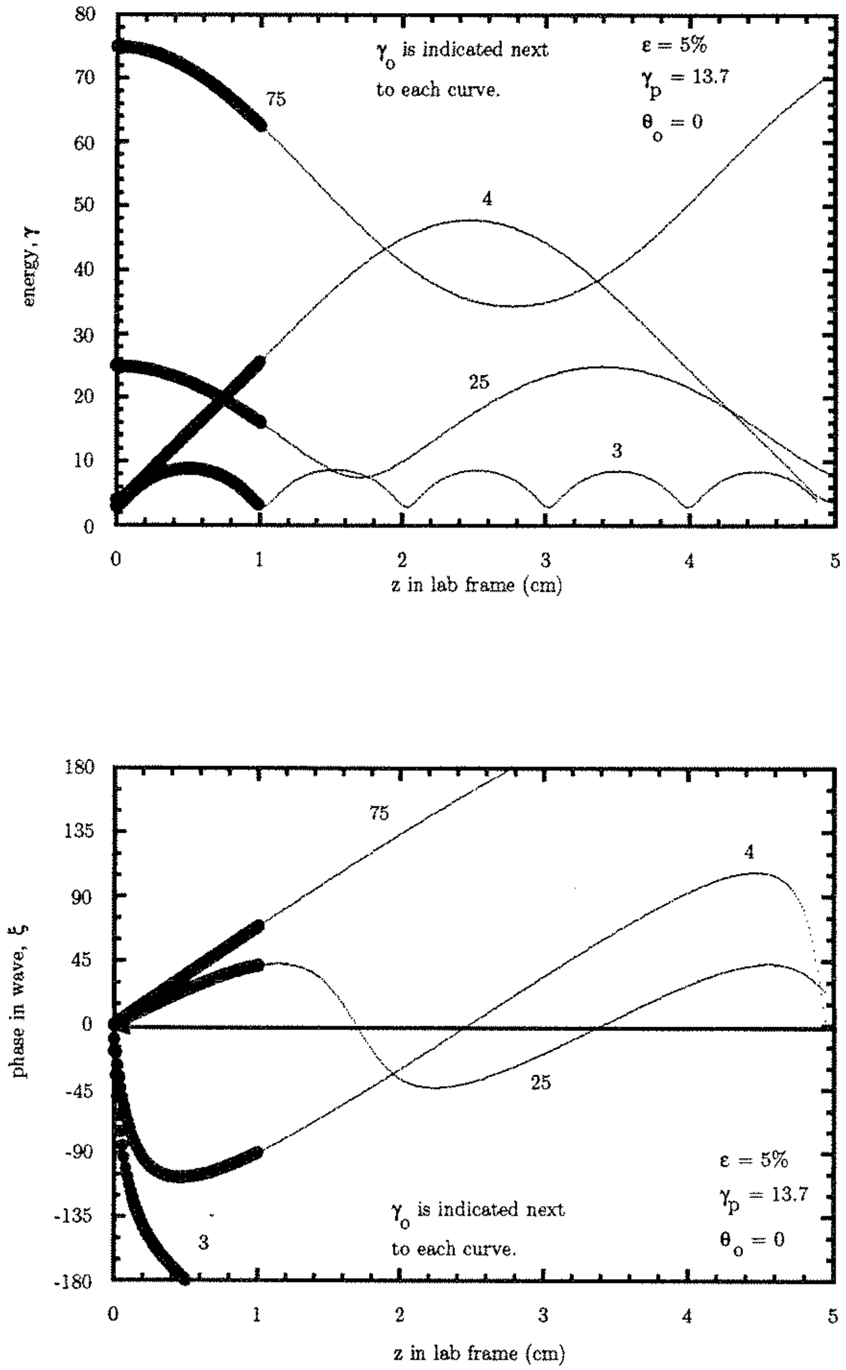

Figure 2.5: Variation of lab frame energy with (a) acceleration distance and (b) phase for two trapped electrons ($\gamma_0 = 4$ and 25) and two untrapped electrons ($\gamma_0 = 3$ and 75).

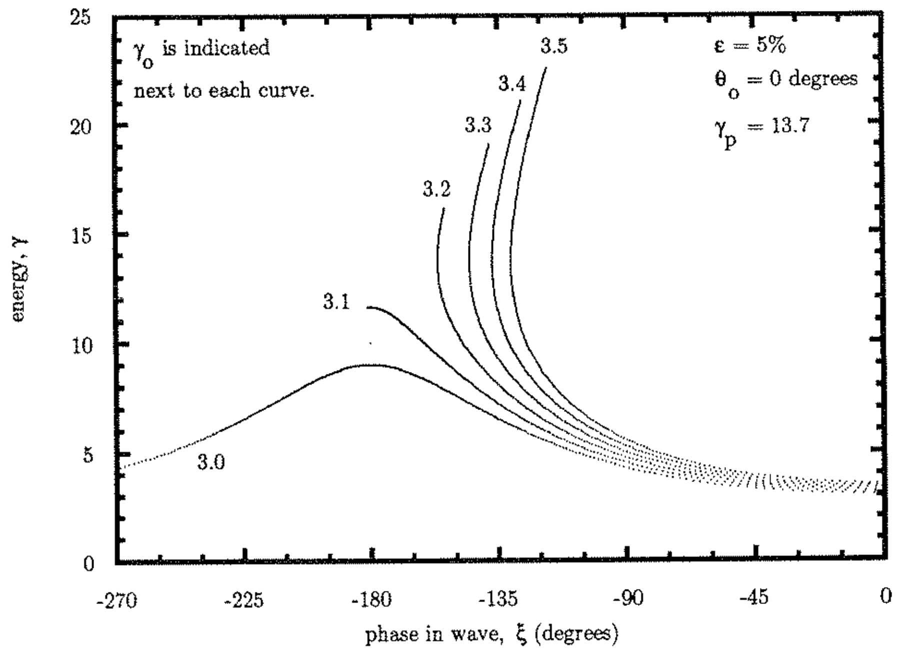

Figure 2.6: Phase space diagram for an electron injected with different energies near the trapping threshold, and showing the transition to trapping.

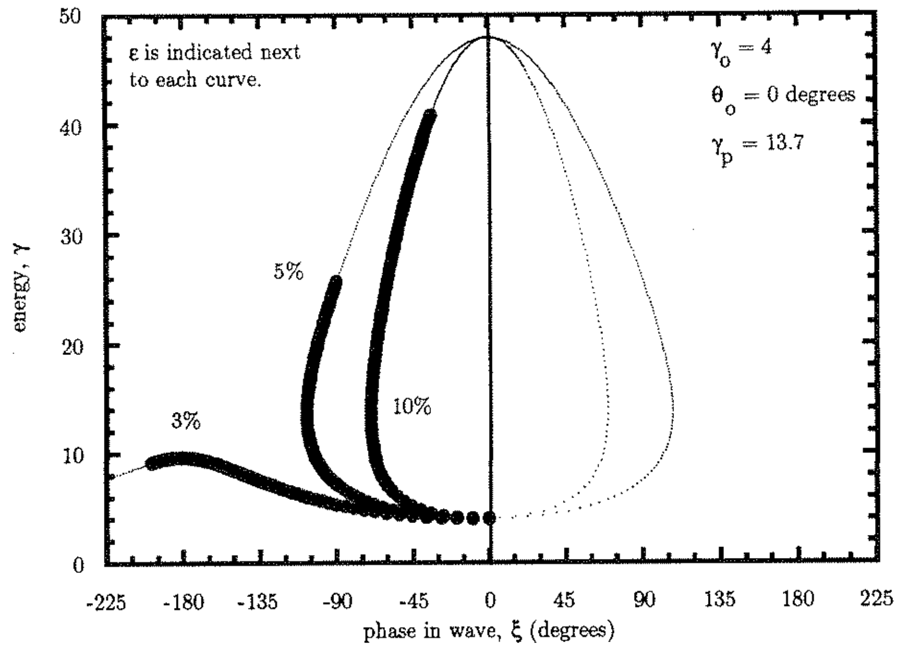

Figure 2.7: Phase space diagram for an electron injected into plasma waves having different amplitudes.

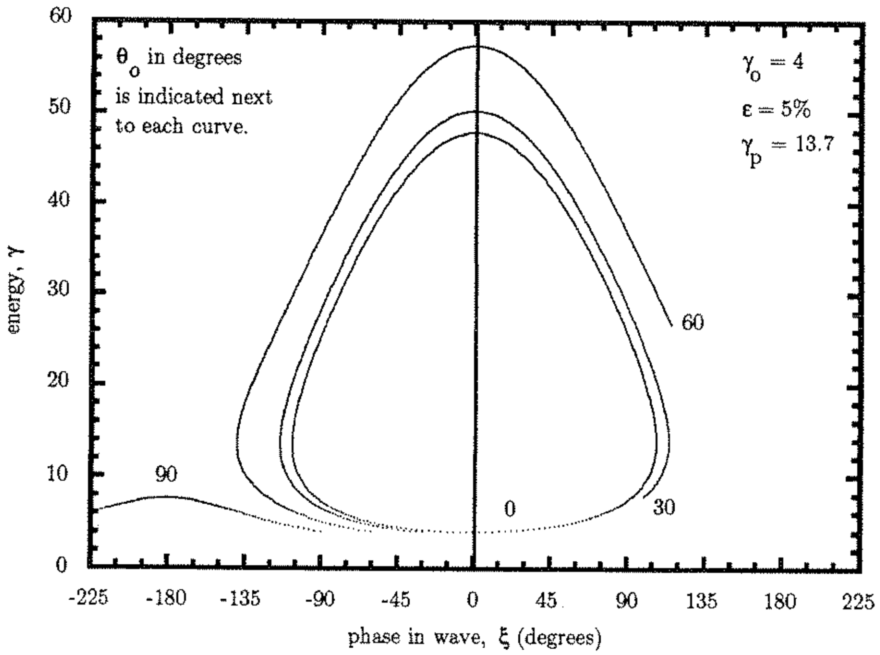

Figure 2.8: Phase space diagram for an electron injected at four different phases in the plasma wave.

is injected at different phases in the plasma wave, $\theta = 0$, 30, 60 and 90 degrees. The trajectory of the electron injected at $\theta = 0$ is plotted for one complete orbit which is about 365 plasma wave periods. The other trajectories are plotted for the same length of time, however they do not make complete orbits as indicated. The 90 degree orbit is untrapped, and the 60 degree orbit attains the highest energy of the three.

Figure 2.9 is a comparison of lab frame energy, γ, vs lab frame distance, z, for an electron trapped by two plasma waves having different γ_p's. The γ_p's of the plasma waves used are 33.0 and 94.5 for the laser wavelength combinations 10.3 & 10.6, and 1.05 & 1.06 μm, respectively. Much larger maximum energies and longer acceleration lengths are obtained for the larger γ_p*'s*, as expected since the trapped electrons stay in synchronism with the wave for a longer time. The injected electron's initial energy is chosen to be $\gamma_o = 5.5$, which is trapped by both

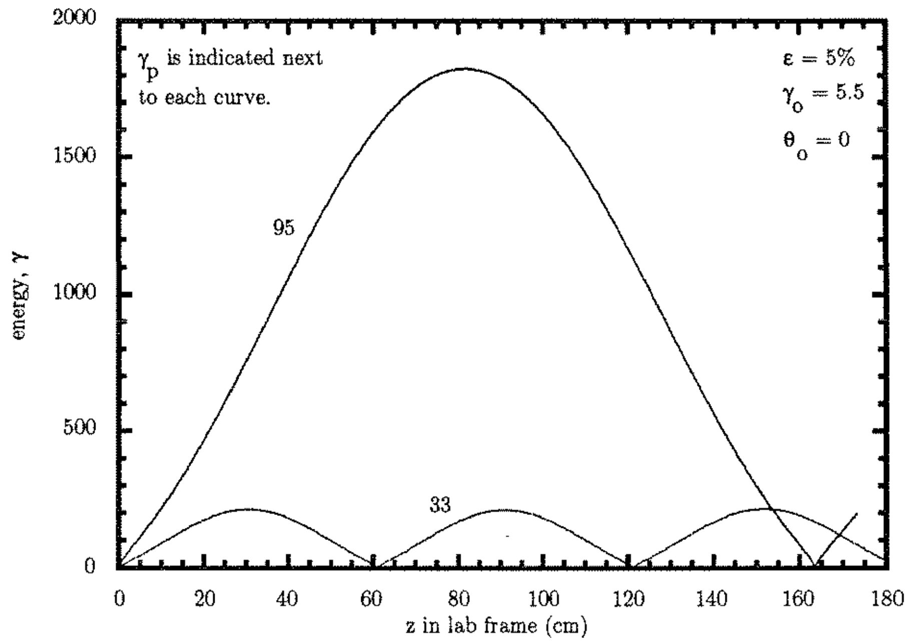

Figure 2.9: Variation of lab frame energy with versus acceleration distance for two gamma phase values.

the $\gamma_o = 33$ and 94.5 plasma waves. (The $\gamma_o = 4$ electron is not used in this example because it would not be trapped by the $\gamma_p = 94.5$ plasma wave if injected at $\theta_o = 0$). The maximum energy and the acceleration length obtained by numerical calculation (figure 2.9) is in agreement with the theoretical values listed in Table A.2.

In the PBWA experiments[7][8], no attempt is made to control the individual electron's injection and extraction phases since the plasma wave's accelerating buckets are typically submillimeter in length and are overlapped by many electrons in the approximately 1 cm long bunch. We therefore examine the case in which electrons are uniformly injected at all phases in order to obtain an accelerated electron energy spectrum. We recalculated the $\gamma_o = 4$ trajectory shown in figure 2.4 and plotted only the end point, (γ, ξ). Then the initial phase was shifted by a small increment, and the trajectory was recalculated and again only the end point was plotted. Figure 2.10(a) is the resulting plot of the electron final energies versus initial injection phase for an acceleration time of 75 plasma wave periods. The figure shows that significant energy gain occurs only for those electrons injected within about 80 deg of either side of $\theta = 0$. Recall however that all electrons gain energy only in the wave's negative phase region. The other electrons are untrapped, but may gain small amounts of energy. The figure also shows that the peak energy gain occurs for electrons injected having a small negative initial phase (about -25 deg to -35 deg). The shape of this curve and the phase corresponding to the peak energy vary as the acceleration length changes.

Figure 2.10(b) is a plot of the distribution of final phases versus initial phase and is expanded to show the peak of the trapping region. Also shown is a dotted line, having slope $= +1$, which represents the initial phase distribution. We see that all the trapped electrons have bunched into phases that are more negative than about -90 degrees. This bunching leads to a strong modulation of the initially uniform electron beam at $\omega_p/2\pi$ (typically greater than terahertz frequencies) producing electron microbunches that are subpicosecond in duration. Also, we find that, for electrons injected at phase points that are symmetric about $\theta_o = 0$, the negative phase trajectory reaches a more positive final phase than the positive phase trajectory, for this case in which the simulation was run for a time of 75 plasma wave periods. The untrapped electrons may reach very large negative (positive) phases because they continue to slip backward (forward) in and out of many successive plasma waves.

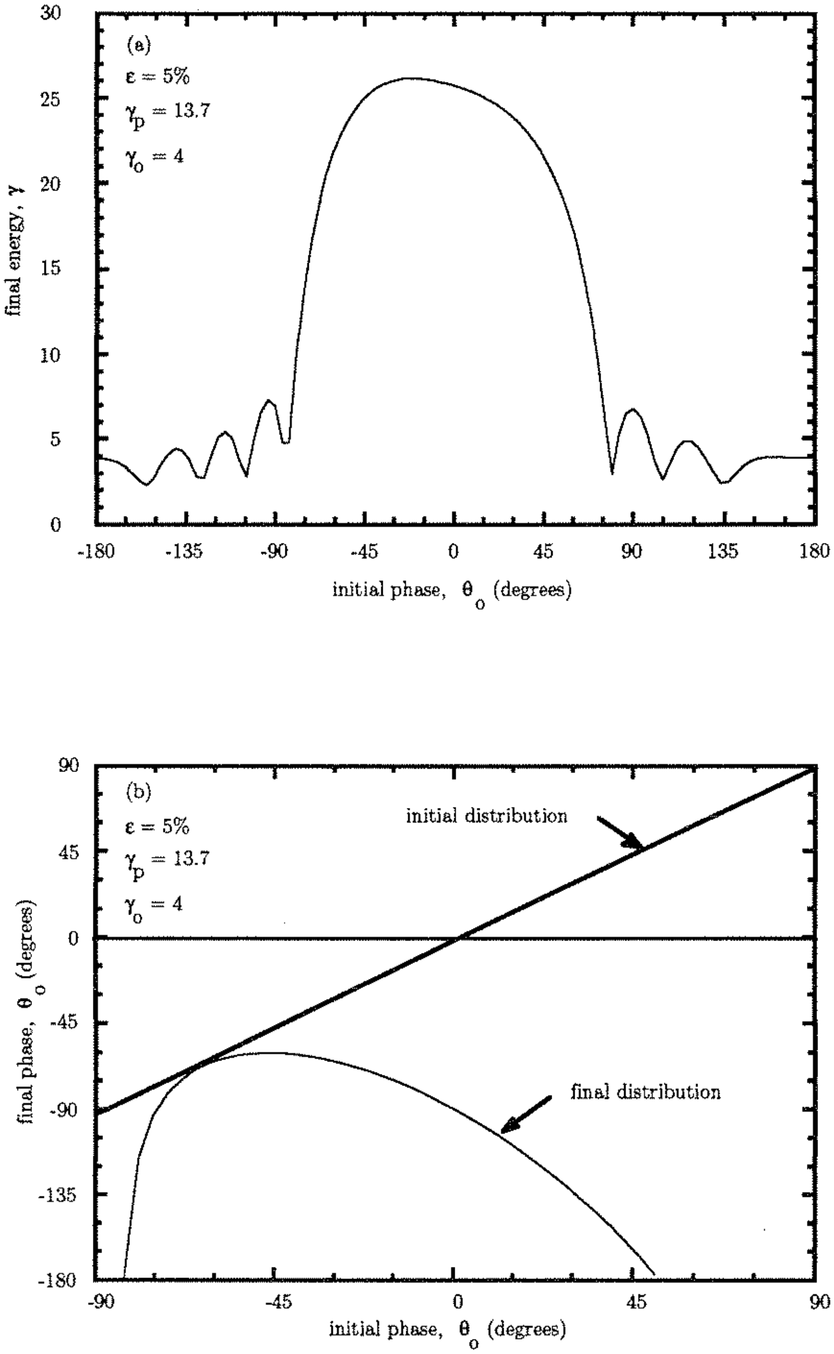

Figure 2.10: Variation of (2) final electron energy and (b) final electron phase in the plasma wave with phase of injection in the plasma wave.

2.3 Influence of Radial Fields on Focusing and Defocusing of Injected Particles: Two Dimensional Model

In the plasma beat wave accelerator, the pump laser beams have transverse intensity variations and finite spot sizes which are comparable in magnitude to the wavelength of the relativistic waves that they excite. Similarly, in the plasma wake field accelerator the "drive" electron bunch is typically c/ω_p wide. In both cases the plasma waves that are excited have strong transverse electric fields as well as strong accelerating, longitudinal electric fields. These fields are 90 deg out of phase with one another [22] and both have the same spatial periodicity. These radial fields exert strong focusing and defocusing forces on off-axis particles [23]. At first glance therefore we might expect only those particles that spend most of their time in both the accelerating and focusing phases of the wave to survive. In this section we extend our 1-D analysis to two dimensions (2-D) to investigate the combined effects of radial and longitudinal fields of the plasma wave on the injected particles. Although the particular case considered here is that of a beat driven plasma wave, the model is readily extended to the PWFA by appropriate choice of the radial electric field $E_r(r, z, t)$.

We assume Gaussian radial profiles for the laser pump beams, the resultant plasma wave and the injected electron beam. The expressions for the radial and longitudinal fields of the plasma wave for Gaussian pump beams are given by [24]

$$E_z(r, z, t) = +\frac{m_o c\,\omega_p \alpha_{em}}{e} e^{\frac{-2r^2}{R^2}} \left[\omega_p t \cos(k_p z - \omega_p t) - \cos k_p z \sin \omega_p t\right] \tag{2.14}$$

$$E_r(r,z,t) = -\frac{4m_o c\,\omega_p \alpha_{em} r}{e k_p R^2} e^{\frac{-2r^2}{R^2}} \left[\omega_p t \sin(k_p z - \omega_p t) - 2(1 - \cos\omega_p t) - \sin k_p z \sin\omega_p t\right] \tag{2.15}$$

where

$z =$ longitudinal coordinate

$r =$ radial coordinate measured from centerline of beam

$R =$ laser beam mean radius

$\alpha_{em} = \left(\frac{eE_{em}}{2m_o\omega_{em}c}\right)^2$ is related to the square of the quiver velocity of the background electrons in the laser field

$E_{em} =$ amplitude of the laser pump field

$\omega_{em} =$ laser pump frequency.

The electron equation of motion solved in the simulation is the vector form of equation 2.14 where

$$\overline{v} = \overline{v}_r + \overline{v}_z \tag{2.16}$$

$$\overline{E} = \overline{E}_r + \overline{E}_z \tag{2.17}$$

$$\overline{P} = \overline{P}_r + \overline{P}_z \tag{2.18}$$

in addition

$$\overline{P} = \gamma m_o \overline{v} \tag{2.19}$$

$$\overline{v} = \frac{\overline{P}}{m_o\sqrt{1 + \frac{P^2}{m_o^2 c^2}}} \tag{2.20}$$

$$\frac{dr}{dt} = v_r \quad and \quad \frac{dz}{dt} = v_z \tag{2.21}$$

The above expressions for E_r and E_z were derived using a linear fluid model in which the secular growth of the plasma wave was taken into account, and which appears as the $\omega_p t$ term that multiplies the sin and cos terms [24]. In this study the plasma wave is assumed to have been previously excited and has reached a maximum value which is constant for the duration of the transit time of the electrons. The assumption was made that ϵ times the maximum amplitude of the longitudinal field on axis was equal to the wave breaking field, $E_{wb} = m_o c \omega_p / e$, and thus the time for the field to reach this amplitude was $t = 1/\alpha_{em}\omega_p$. Therefore the secular growth factor, $\omega_p t$, was replaced with $1/\alpha_{em}$ in the simulations. From the amplitude of E_r on axis, $\epsilon\, m_o c\, \omega_p / e$, we see that ϵ in this notation is the peak wave field normalized to the cold wave breaking field, $m_o c\, \omega_p / e$.

The simulations were run for 75 plasma wave periods which permitted resolution of variations in the electron trajectories, energy and phase which occur early on in a finite length $\gamma_p = 13.7$ beatwave experiment. The radial width of the laser beam used in the example we give below is smaller than that of the electron beam, therefore the Gaussian variation of the electron's density across the width of the plasma wave is small. This is also likely to be the case in other experiments although our model permits many other choices for the transverse variations of either the electron beam density or the plasma wave fields. Figure 2.11 is a plot of the radial widths of the laser beam, plasma wave and electron beam, as measured in one of the UCLA beatwave experiment [8]. The plasma wave overlaps a small fraction of the electron beam, and the ratio of the cross sectional areas at the minimum waist is approximately 0.03. Figure 2.12 illustrates the radial variation of plasma wave fields, E_r and E_z, near the axis and at an arbitrary position in phase. Both E_r and E_z can be positive and negative, meaning that they can be focusing or defocusing, and accelerating or decelerating, respectively. Note that while the absolute value of E_z is maximum on axis, E_r is zero on axis and peaks off axis. Also E_r can be

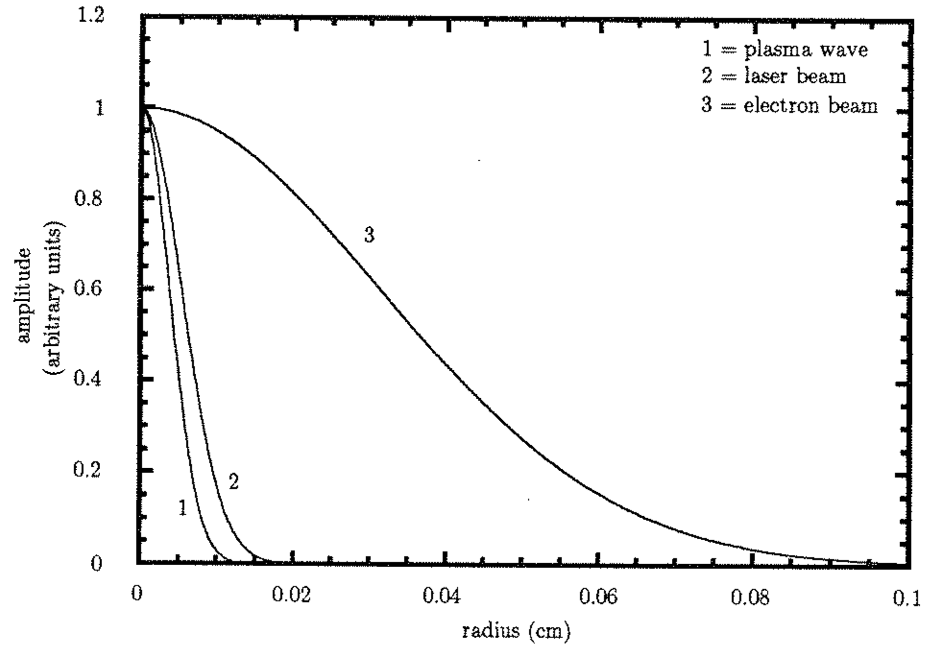

Figure 2.11: Comparison of the measured Gaussian widths of the lasers, plasma wave and electron beam in the original UCLA beatwave experiment.

comparable to E_z particularly as the plasma wave's transverse dimension approaches its wavelength. On a longer time scale involving ion motion this strong radial electric field makes the plasma wave unstable against transverse breakup and causes the so called resonant self-focusing of the laser beams.

Figure 2.13 illustrates the longitudinal variation of E_r and E_z. It also shows the axial positions where the longitudinal field is accelerating or decelerating and where the radial field is focusing or defocusing. The region from -90 to 0 degrees is both focusing and accelerating and is the ideal phase region in which the electrons should be located for attaining maximum acceleration.

The electron trajectories (radial versus longitudinal positions) were calculated for a $\gamma_p = 13.7$ plasma wave and are plotted in figures 2.14(a) and 2.14(b) as a function of the fractional plasma wave amplitude ($\epsilon = 5\%$ and 10%, respectively). The electrons are injected at $\theta_o = 0$ and all have $\gamma_o = 4$. Electron trajectories

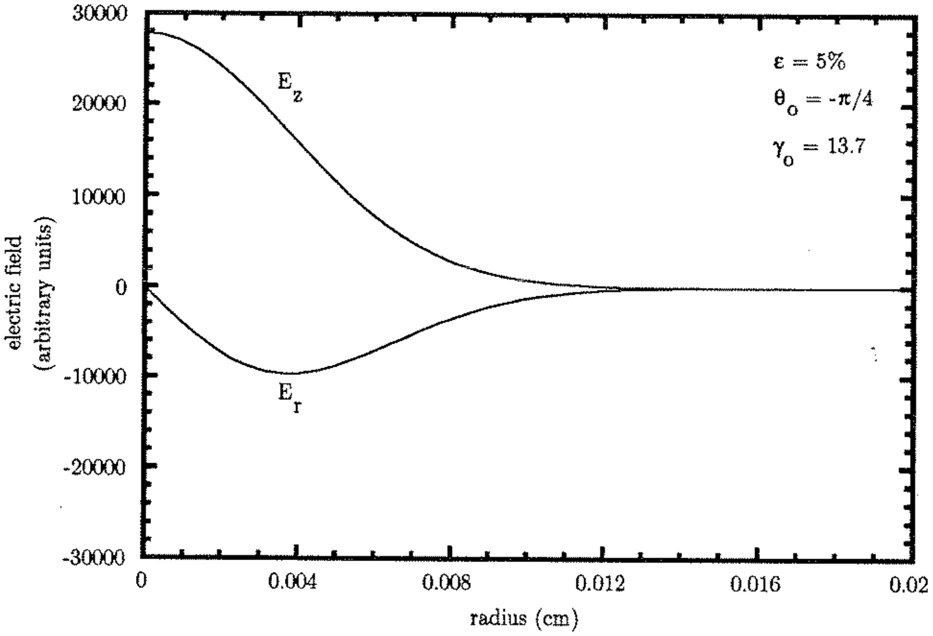

Figure 2.12: Typical radial variation of the longitudinal and radial components of the beatwave fields at an arbitrary phase.

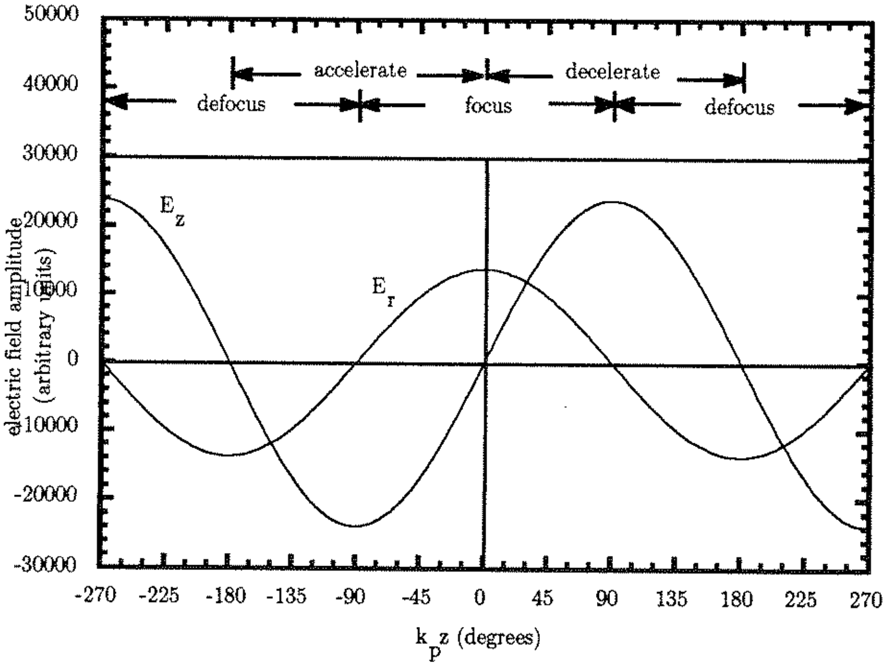

Figure 2.13: Longitudinal variation of the longitudinal and radial components of the beatwave fields, showing the accelerating, decelerating, focusing and defocusing regions.

that oscillate about the axis are focused. Figure 2.14(a) shows the trajectories for electrons injected into a 5% plasma wave, and having radii that vary from 0 to 50 μm (2.3 c/ω_p). These trajectories do not oscillate about the axis, but make one crossing. The electrons are injected at $\theta_o = 0$ where the focusing is strongest, which explains the sharp bending of the trajectories toward the axis at the start of acceleration. However, the electrons move eventually into the negative phase region where the focusing gradually weakens and becomes defocusing past 90 degrees. Although the electrons eventually get defocused, they are continually in the acceleration region while moving in the negative phase region, which will result in some acceleration for electrons injected at $r \leq 10$ μm before they eventually get deflected from the beam. If the accelerated electrons are extracted at this point they will emerge with a very large angular spread although they were injected exactly parallel to the axis.

Figure 2.14(b) shows the trajectories for electrons injected into a $\epsilon = 10\%$ plasma wave, and having radii that vary from 0 to 50 μm. Electrons having initial radii out to about 30 μm oscillate about the axis and are trapped. The figure shows that the period of this oscillation increases and the amplitude of the oscillation decreases in the lab frame as these electrons accelerate. The 40 μm trajectory appears as if it will cross the axis after a longer acceleration distance. Whether or not this 40 μm trajectory will get trapped will likely depend on the relative strengths of the radial and longitudinal fields at the various radii that it traverses.

The variation of the electron trajectory as a function of initial electron energy was also investigated. It was found that as the injection energy of the trapped electrons increases, the period of oscillation decreases and the amplitude of oscillation decreases. These oscillations are nothing more than the classical betatron oscillations in an accelerating cavity.

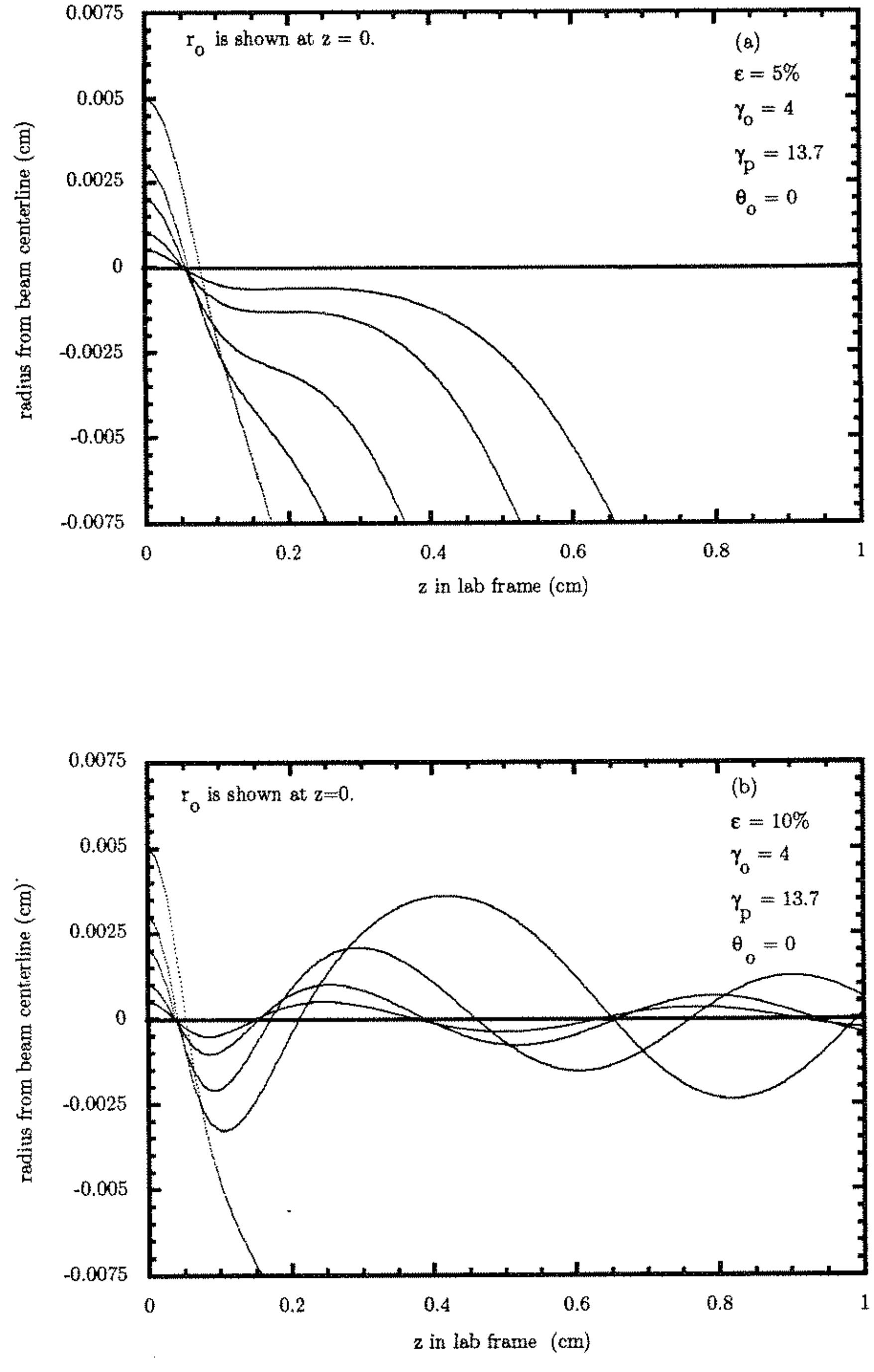

Figure 2.14: Variation of electron trajectories with radius of injection in a 2-D plasma wave for (a) $\epsilon = 5\%$ and (b) $\epsilon = 10\%$.

Figure 2.15 (a) and 2.15 (b) show trajectories for electrons injected at a particular radius ($r = 20\ \mu$m), energy $\gamma_o = 4$ and with injection phases varying in four equal steps from $\theta = -\pi/2$ to $+\pi/2$. Figure 2.15 (a) shows that none of these electrons is trapped in the $\epsilon = 5\%$ wave. However the electron injected at $\theta = +\pi/4$ stays close to the axis long enough to gain some energy. The electron injected at $\theta = -\pi/2$ spends most of its initial acceleration time in the region where defocusing is getting stronger, and therefore is immediately deflected away from the axis. The other electrons ($\theta = -\pi/4$ through $+\pi/2$) are initially focused since they spend the initial part of their acceleration time in the focusing region. Figure 2.15 (b) shows that, in the $\epsilon = 10\%$ plasma wave, only the electron injected at $\theta = 0$ deg is trapped and is expected to gain significant energy. All other electrons start or slip back into defocusing regions. The $\theta = +\pi/4$ electron makes two crossings of the axis before being deflected and is therefore expected to gain a small amount of energy.

2.4 Influence of Beam Emittance: Three Dimensional Model

The previous studies showed that the electrons which are accelerated to high energies ideally have initial transverse positions that are close to the plasma wave symmetry axis and are injected near the zero phase point (potential minimum) the wave. In this section we investigate the effects that transverse momentum has on the number of electrons accelerated and on the amount of energy they gain. A three dimensional (3-D) plasma wave model is used to predict the energy, momentum, and radial and phase distributions of electrons that have been injected into a relativistic plasma wave. Emittance is used to obtain the electron beam's angular spread and thus to give the electrons random initial momenta in the x and y directions.

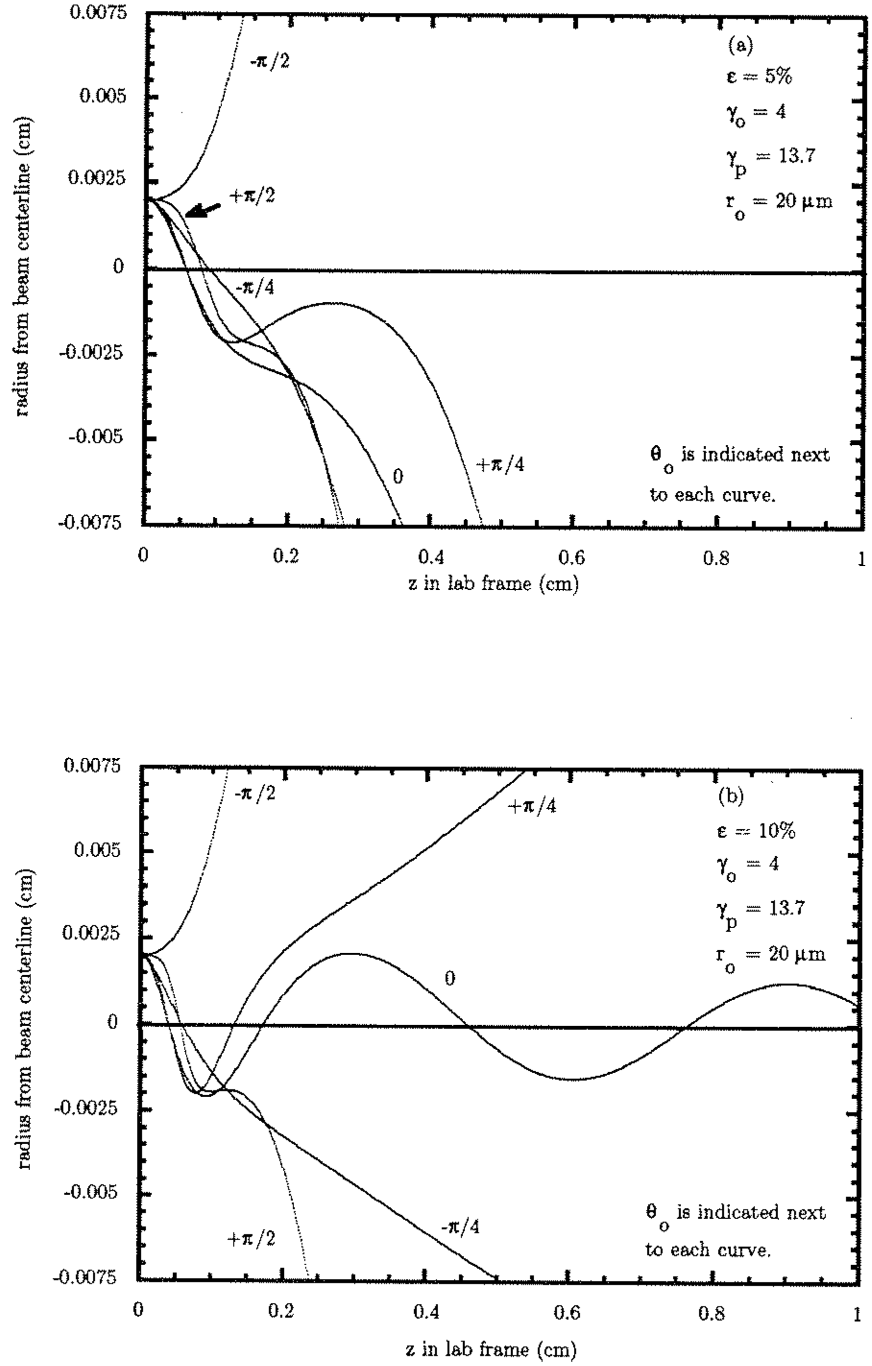

Figure 2.15: Variation of electron trajectories with injection phase in a 2-D plasma wave for (a) $\epsilon = 5\%$ and (b) $\epsilon = 10\%$.

The equation of motion solved in the simulation is the vector form of equation 2.9 with three components of $\overline{v}$, $\overline{E}$, and $\overline{P}$ where

$$E_z(r,z,t) = +\frac{m_o c\,\omega_p \alpha_{em}}{e} e^{\left(\frac{-2r^2}{R^2}\right)} \left[\omega_p t \cos(k_p z - \omega_p t) - \cos k_p z \sin \omega_p t\right] \tag{2.22}$$

$$E_x(r,z,t) = -\frac{4 m_o c\,\omega_p \alpha_{em} x}{e k_p R^2} e^{\left(\frac{-2r^2}{R^2}\right)} \left[\omega_p t \sin(k_p z - \omega_p t) - 2(1 - \cos \omega_p t) - \sin k_p z \sin \omega_p t\right] \tag{2.23}$$

$$E_y(r,z,t) = -\frac{4 m_o c\,\omega_p \alpha_{em} y}{e k_p R^2} e^{\left(\frac{-2r^2}{R^2}\right)} \left[\omega_p t \sin(k_p z - \omega_p t) - 2(1 - \cos \omega_p t) - \sin k_p z \sin \omega_p t\right] \tag{2.24}$$

and

$x =$ displacement of electron from x axis of wave

$y =$ displacement of electron from y axis of wave

$$\frac{dx}{dt} = v_x, \quad \frac{dy}{dt} = v_y \quad and \quad \frac{dz}{dt} = v_z. \tag{2.25}$$

We solved for P_x, P_y, P_z, x, y, and z using a leap-frog scheme.

In order to simulate the random initial coordinates of individual electrons in the injected beam, a random selection technique was used to set the initial conditions. A uniform pseudorandom number generator was used to select the injection phase (between −180 and +180 deg) of each electron in the wave. A Gaussian pseudorandom number generator, with a standard deviation equal to the radius of the electron beam (0.044 cm or 20.1 c/ω_p) as shown in figure 2.11, was used to select each electron's x and y coordinates relative to the axis of the plasma wave. A Gaussian pseudorandom number generator, with a standard deviation equal to the electron beam's angular spread (0.045 radians) which was obtained from the emittance, was used to select σ_x and σ_y which were then used to find the initial transverse momenta of each electron as follows.

$$P_x = \sigma_x P_z \quad \text{and} \quad P_y = \sigma_y P_z. \tag{2.26}$$

The emittance used in the simulation was 20π mm-mrad which corresponds to the value estimated for the UCLA experiments within a factor of two [8]. In the simulations 250,000 electrons were injected into a $\gamma_p = 13.7$ beatwave. Each electron was injected having $\gamma_o = 4$ and the fractional plasma wave amplitude was $\epsilon = 10\%$. The simulation duration corresponded to the time for a reference electron to reach its maximum possible energy provided it was injected on axis at phase equal to zero. This time was approximately 117 $(2\pi/\omega_p)$, which corresponds to an acceleration length of approximately 1.5 cm $(690c/\omega_p)$ for the reference electron. At the end of the simulation the accelerated electrons were counted and their initial and final energies, momenta and coordinates were analyzed. The results are shown in the histogram of figure 2.16 and scatter graphs of figures 2.17, 2.18 and 2.19. Each point on the scatter graphs represents the data for one electron.

The number of electrons accelerated into each energy bin for the cases of with and without emittance is displayed in figure 2.16. Each energy bin was $\Delta\gamma = 2$ wide. The histogram shows that in either case a group of electrons was accelerated from γ_o up to the energy range $14 \leq \gamma \leq 20$ and another group was accelerated to the higher range $44 \leq \gamma \leq 62$ centered at $\gamma \approx 54$. Considering that the acceleration length is approximately 1.5 cm, electrons in the higher energy group experienced an effective accelerating gradient of approximately 1.7 GV/m. The inclusion of

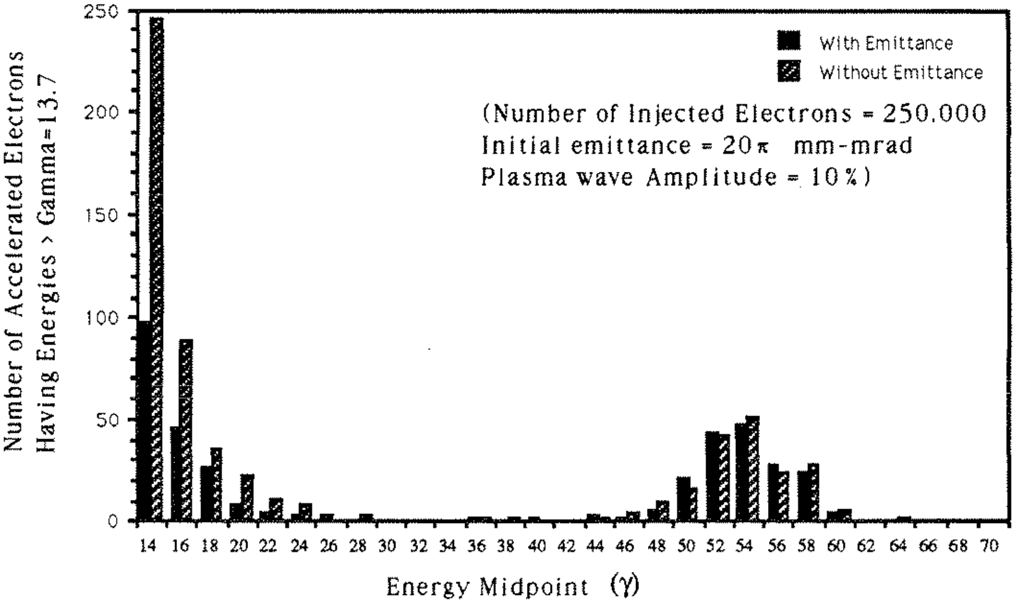

Figure 2.16: Accelerated electron energy spectrum for electrons having $\gamma_o = 4$ injected into a $\gamma_p = 13.7$ plasma wave and accelerated for 117 plasma periods for cases with and without initial emittance. This acceleration time is the time for a particle injected on axis with zero phase to reach maximum energy.

an emittance of 20π mm-mrad in the simulation reduced the number of electrons accelerated into the higher energy group by as much as a factor of two for some higher energy bins, and by as much as a factor of five in some lower energy bins. Of the 250,000 electrons injected into the simulation which included emittance, approximately 124 were accelerated into the higher energy bins, 84 were accelerated into the lower energy bins shown in the histogram and an additional 2444 electrons were accelerated into the $\gamma = 8$, 10 and 12 bins which are not shown in the figure. The remainder of the 250,000 electrons were either decelerated, or did not experience acceleration above the $\gamma = 6$ energy bin. The electrons in the higher energy bins centered about $\gamma \approx 54$ in the histogram clearly are trapped by the plasma wave, however it is not clear that the electrons in the lower energy bins are trapped or untrapped. The 1-D analysis of trapping (see figure 2.3(a)) showed that the maximum energy for untrapped electrons is $\gamma \approx 13.7$, which is equal to the plasma wave's γ_p. Note that only those electrons with energies greater than $\gamma_p = 13.7$ are plotted in figure 2.16. Also, only those electrons with in a 8° cone angle that could be collected and detected by the UCLA apparatus are plotted in the histogram.

Figure 2.17(a) is a scatter diagram of the accelerated electron energies (γ) versus final phases (θ) in the plasma wave at time $t \approx 117$ $(2\pi/\omega_p)$. Data for electrons having energies below $\gamma \approx 8$ are not shown. All of the electrons were randomly distributed between -180 and +180 degrees at $t = 0$. At $t \approx 117$ $(2\pi/\omega_p)$ most of the electrons have slipped backward in phase beyond -180 degrees and are untrapped. These untrapped electrons have been accelerated to energies greater than $\gamma = 8$ but less than $\gamma \approx 13.7$, which is the maximum predicted by the 1-D analysis. Most of these untrapped electrons are drifting, except for the few that may gain or loose energy due to being within the spatial width of the narrow 150 μm (6.9 c/ω_p) wide plasma wave. In the trapped electron phase region ($> -180\,\mathrm{deg}$) there exist low energy electrons having energies extending down below $\gamma \approx 13.7$ and which may later become trapped and gain energy or untrapped and slip backward in phase. The highest energy trapped electron distribution extends from phase approximately equal to -45 to 0 and has a peak of $\gamma \approx 60$ at a phase of approximately $-30\,\mathrm{deg}$. This distribution of high energy electrons should continue to gain energy as it moves forward in phase, and start to loose energy after passing $\theta = 0$. The reference electron is at phase equal to zero and has energy $\gamma \approx 48$ in the figure.

Figure 2.17(b) is a scatter diagram of the electron transverse positions ($x\,\omega_p/c$) versus final phases (θ) in the plasma wave. The highest energy trapped electrons form a narrow beam on axis having a maximum diameter of approximately 85 μm (4 c/ω_p) as shown on the right in the figure. The untrapped electrons (having $\theta < -90\,\mathrm{deg}$) are drifting backward in the wave frame and are shown bunched into groups in the figure. The bunching is due to the electrons being accelerated or

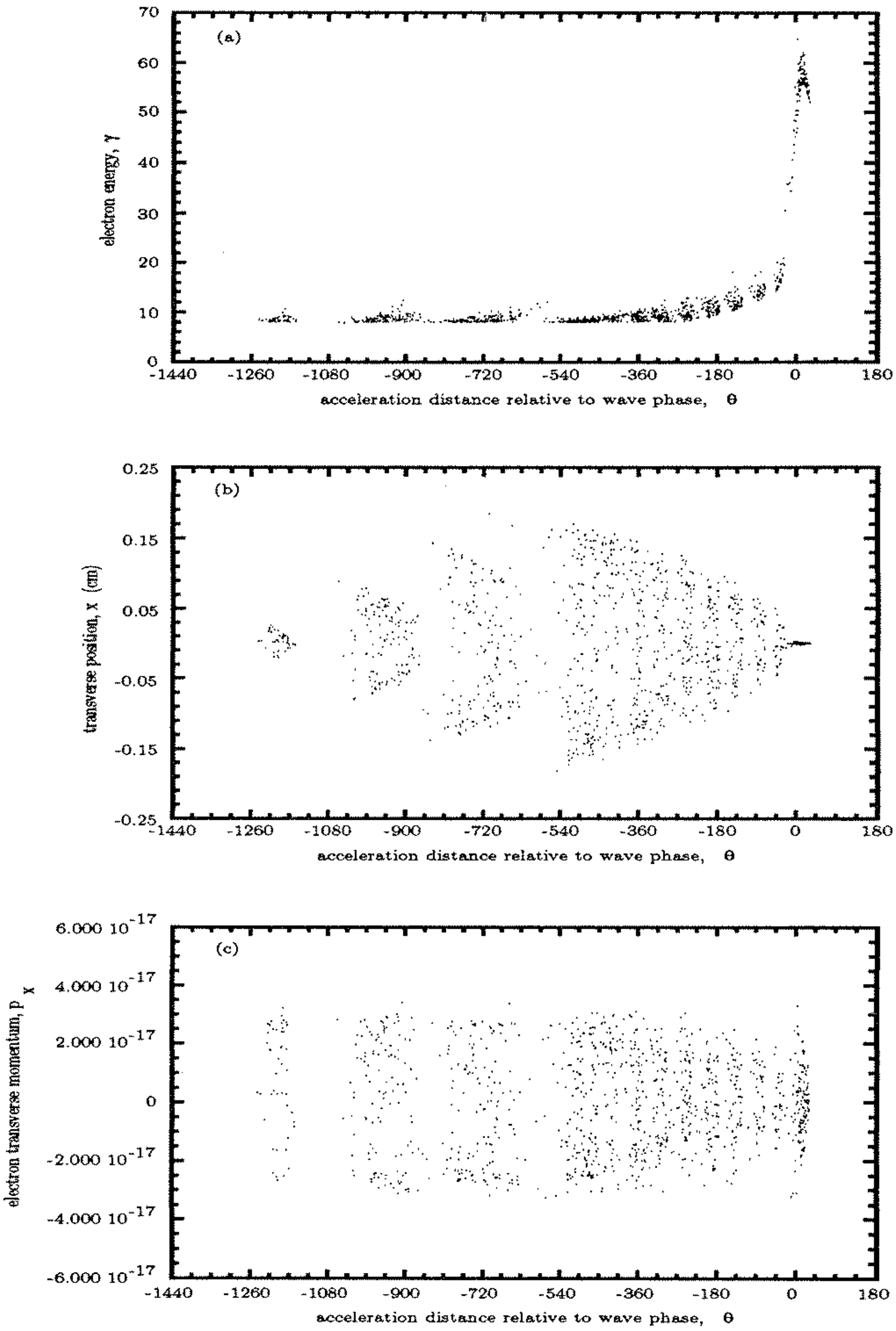

Figure 2.17: Scatter diagram of electron energies and positions at end of acceleration. (a) Energy versus longitudinal position relative to initial wave's final position, (b) transverse position vs longitudinal position (b) transverse momentum vs longitudinal position.

decelerated by the longitudinal electric fields of the plasma wave at an earlier time. In order for the untrapped electrons to have gained energies up to a maximum of $\gamma = 13.7$ (as shown in figure 2.17(a)) and to become bunched in space (as shown in figure 2.17(b)), they needed to have been previously very close to or have crossed through the narrow plasma wave at the axis before drifting out to large radii. For the case of zero emittance, only those electrons originally located within or close to the plasma wave will be accelerated, and most of these will eventually drift out to large radii. For the case which includes emittance, those electrons that were originally located at large radii in the electron beam, and far from the plasma wave, may have a small probability of crossing through the plasma wave provided their initial transverse momenta (due to emittance) direct them toward the axis. In addition, the inclusion of emittance may cause electrons originally located near the plasma wave to not be accelerated to high energies due to having initial momenta which direct them away from the plasma wave. These factors, along with the fact that the plasma wave intercepts a very small area of the electron beam (3%), account for the small fraction of the total number of electrons that get accelerated.

Figure 2.17(c) is a scatter diagram of the electron transverse momenta, P_x/mc, versus final phases (θ) in the plasma wave. The high energy trapped electrons have a spread in momenta due to their oscillatory motion although they form a narrow beam. The untrapped electrons have alternating large and small absolute values of momenta due to previously being in the region of focusing or defocusing radial electric fields as they interacted with the plasma wave.

Figure 2.18 is a scatter diagram of the electron energies (γ) versus transverse positions ($x\,\omega_p/c$). This figure shows the spread in energies of the electrons located within the narrow high energy beam. The electrons in the range $8 \leq \gamma \leq 20$ have a distribution of radii that decreases from approximately 2 mm to 0.2 mm (92 c/ω_p

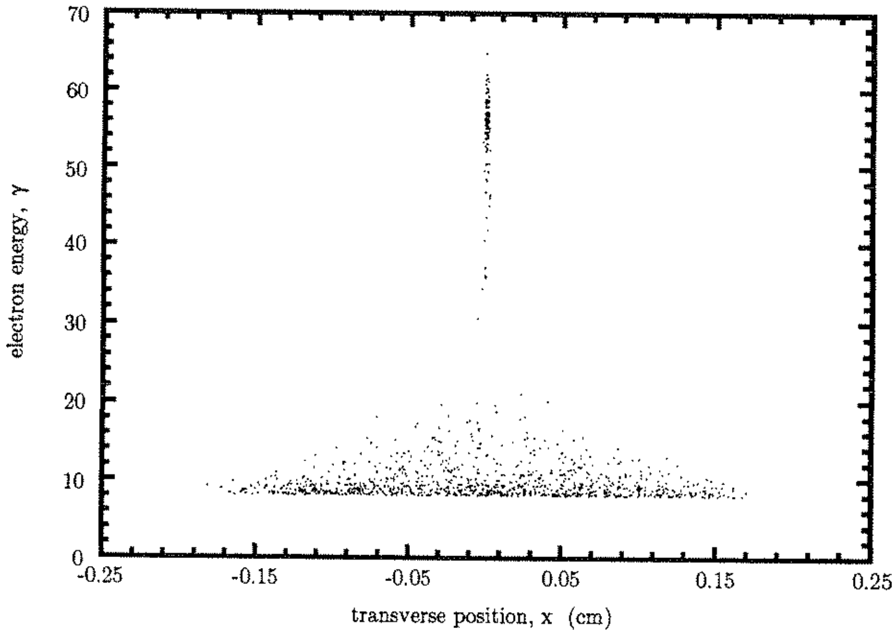

Figure 2.18: Scatter diagram of electron energies vs transverse positions. The higher energy electrons, ($\gamma > 20$), are within a beam full width of $2\lambda_p$ and are trapped in the plasma wave. Lower energy electrons are drifting at constant energies at larger radii.

to 9.2 c/ω_p) as the energy decreases through the range. The electrons at wide radii located outside of the plasma wave are drifting with constant energy.

Figure 2.19 is a phase space scatter diagram showing the electron transverse momenta (P_x/mc) versus transverse positions ($x\,\omega_p/c$). The plots show data for electrons in energy bins centered at $\gamma = 10.5$, 22.5 and 55 and each bin has a width of $\Delta\gamma = 5$, 15 and 18, respectively. Figure 2.19(a) for the $\gamma = 10.5$ bin shows that electrons are basically in thin diverging hollow cone that is denser near the inner surface and diffuse near the outer surface. groups that have different angular orientations. Figure 2.19(b) shows the phase space scatter data for electrons in the $\gamma = 22.5$ bin, and also indicates that these electrons are diverging, but in a very narrow cone. Figure 2.19(c), with the x axis expanded, shows the $\gamma = 55$ data which indicate that the electrons are located very near and on both sides of the

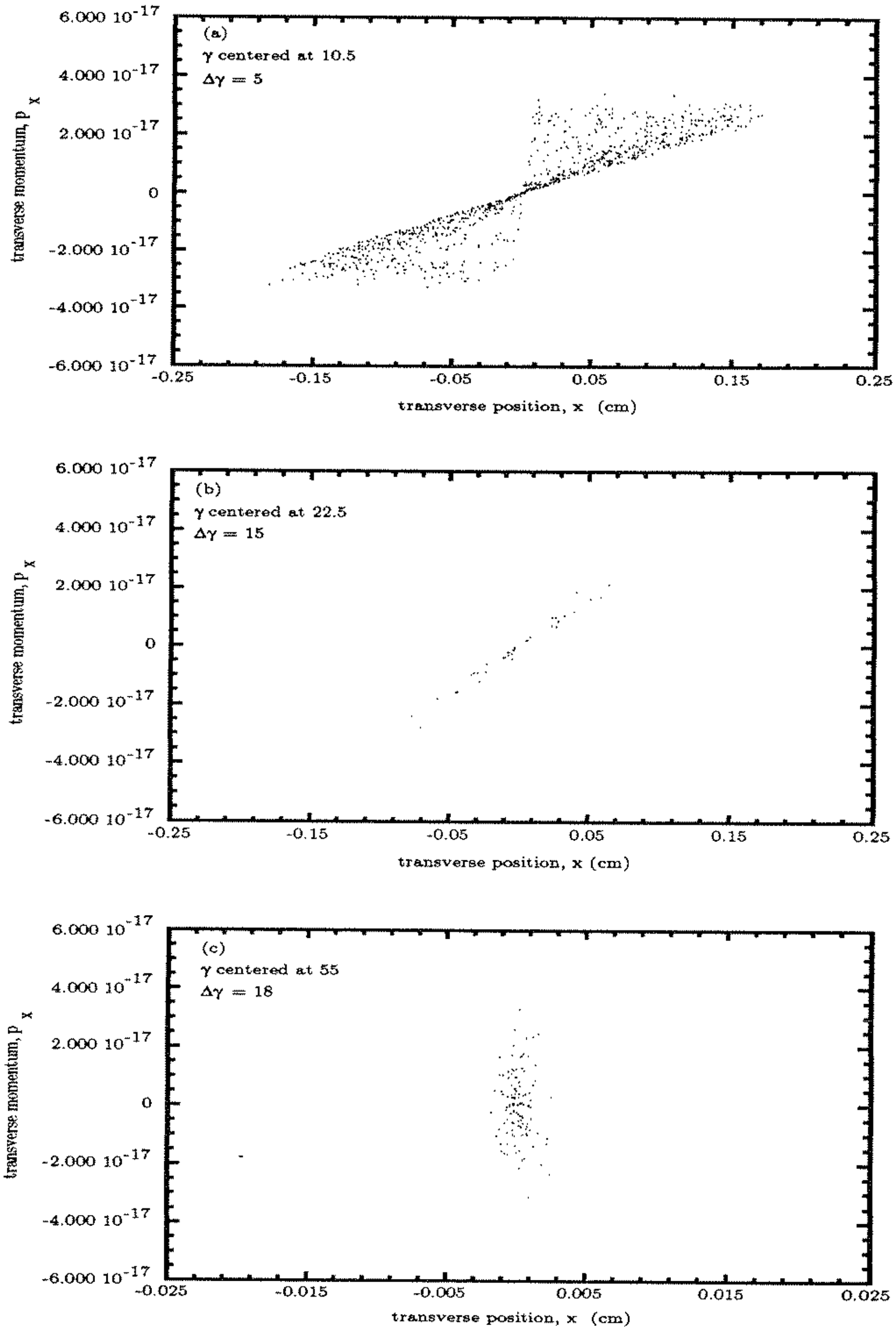

Figure 2.19: Scatter diagram of electron energies and positions at end of acceleration. (a) Energy versus longitudinal position relative to initial wave's final position, (b) transverse position vs longitudinal position (b) transverse momentum vs longitudinal position.

x axis and that the electrons are converging and diverging as they oscillate about the axis. As shown by the trajectories of figure 2.14(b) these trapped electrons are executing betatron oscillations.

We have also considered a case in which the product of the acceleration length and plasma wave amplitude is held constant while varying both the acceleration length and plasma wave amplitude. The reason for considering this case is that an alternative signature for the existence of the beat driven plasma wave is the generation of Stokes and anti-Stokes satellites copropagating with the incident laser beams. The absolute intensities of the first stokes and anti-Stokes satellites are directly related to the number of scatterers in the scattering volume which in turn is proportional to $(n_1/n_o)A_s \cdot L$. Here $A_s \cdot L$ is the scattering volume with cross section A_s and length L. Since n_1/n_o is proportional to $\overline{E}$ this technique yields the $\overline{E} \cdot \overline{L}$ product rather than $\overline{E}$. In one version of the UCLA experiments, the wave amplitude-acceleration length product, $\overline{E} \cdot \overline{L}$, has been estimated from light scattering techniques [8] and used in these simulations to predict the electron output. In this case the plasma source used was a theta pinch (see Appendix B). Three $\overline{E} \cdot \overline{L}$ products were used as follows.

$$\overline{E} \cdot \overline{L} = 0.013, \ \frac{0.013}{\sqrt{2}} \ \text{and} \ \frac{0.013}{2} \quad \text{cm} \tag{2.27}$$

Where $\overline{E}$ is the dimensionless electric field $eE/m_o c\omega_p$. The largest value of 0.013 corresponds to the maximum $\overline{E} \cdot \overline{L}$ achieved experimentally using the theta pinch plasma source. From Raman scattering measurements the interaction length is thought to be at least 0.075 cm. Therefore for each value of $\overline{E} \cdot \overline{L}$, three values of L were used: 0.075, 0.150, and 0.300 cm. The data from these simulations are summarized in figure 2.20 which shows the number of electrons accelerated into the

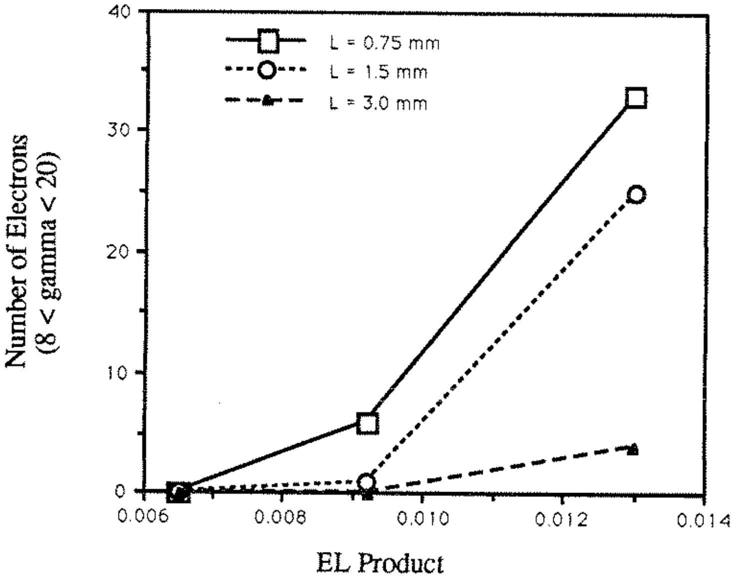

Figure 2.20: Number of detectable accelerated electrons ($8 < \gamma < 20$) versus $E \cdot L$ product and acceleration length for the UCLA experiment. Only those electrons emerging from the plasma wave within a cone angle of 8° are counted.

spectrometer detection window ($8 \leq \gamma \leq 20$). (See Appendix C for a description of the spectrometer.) The largest number of accelerated electrons are obtained in the case of the shortest acceleration length and consequently the largest plasma wave. In the best case, the ratio of accelerated to injected electrons is $33/25000 \approx 1.3 \times 10^{-3}$.

Appendix A is a collection of tables containing data pertaining to beatwave acceleration experiments. Appendix B contains brief comments on the theta pinch, arc and gas jet plasma sources used at various times in the UCLA beatwave acceleration experiments, along with example energy spectra for each source. Appendix C contains a description of a sensitive electron detection apparatus designed to detect single electrons which was used in the UCLA beatwave experiments. In Appendix D are brief comments on the Osaka University's plasma beatwave acceleration experiments. In Appendix E is a description of one method of including plasma wave spatial inhomogeneities in the numerical simulations of the beatwave accelerator, and one example is given for the UCLA gas jet plasma source.

2.5 Summary

Computational models have been used to examine the laser plasma beatwave acceleration experiment and to give physical insight into how relativistic electrons interact with plasma waves that are propagating with a phase velocity that is almost the speed of light. These models will be extremely useful in designing plasma wave experiments and interpreting their results. The model are idealized, however, and the inclusion of such things as temporal effects, plasma wave harmonics and plasma non-uniformity would lead to even a smaller fraction of the injected electrons being accelerated in an experimental situation. These additional effects should be addressed in future research on plasma wave accelerators.

Chapter 3

Studies of Transverse Motion of Relativistic Electrons Through Relativistic Plasma Waves

3.1 Introduction

The measurement of relativistic plasma waves (RPWs) is a difficult task and, aside from Thomson scattering, there are no well established diagnostic techniques [27]. In this chapter, the scattering of an injected relativistic electron bunch by the RPW as a diagnostic technique, which may complement Thomson scattering, is investigated using numerical simulations. In the preceding chapter, 2-D and 3-D numerical models were used to study electron acceleration and to predict the electron energy spectrum in the laser-plasma beatwave accelerator, wherein electron bunches were injected parallel to the plasma wave's velocity [25]. In the present chapter, the same numerical models are used to study the motion of electron bunches which are injected in the direction that is transverse to the plasma wave velocity.

The electron scattering results of the present chapter are important not only for diagnostic purposes [29], but also for the plasma wave undulator scheme [28] which will be discussed in Chapter 4. For the plasma wave undulator's radiation to be coherent, the electron bunch must remain spatially coherent as it passes through the RPW. This places limits on both the electron bunch and RPW. The determination of these limits and their effects on the plasma undulator was the original motivation for the work of this chapter.

The RPWs discussed herein are considered to be excited by laser beatwaves (optical mixing) as in the UCLA experiments, and their properties are described in Table A.2. The waves have typical density fluctuations of up to approximately 10% of the background density ($n_o = 10^{16}$ to 10^{17} cm^{-3}). Two interchangeable notations are used to describe the amplitude of the plasma wave density fluctuation, ϵ and a_w. The ϵ was used in Chapter 2 in the laser plasma beatwave study while a_w, also called the wiggle parameter in the free electron laser literature, is used in this chapter and in Chapter 4.

3.2 Model and Assumptions

The model assumes that the longitudinal fields of the plasma wave are periodic in the z (wave propagation) direction, and that the maximum value of the field is constant. The transverse fields have a Gaussian profile in the directions perpendicular to z. The fields vary in time at the plasma frequency. The velocities of the electrons and the phase velocity of the plasma wave are approximately equal to the speed of light. The space charge repulsion among the electrons is considered negligible. The a_w is considered small and the wave is linear. A wide plasma wave (approximately 100 plasma wave wavelengths (λ_p) wide) was used in these simulations because many undulations were desired for the plasma undulator radiation study. In the preceding laser-plasma beatwave study of Chapter 2, the plasma wave's full Gaussian width was approximately one λ_p, and the resulting large radial field had a strong effect on the electron trajectories, which approximated the situations found in plasma wave acceleration experiments [8]. Later in this chapter we will comment on the trajectories of electrons injected transversely through narrow (one λ_p) plasma waves.

3.3 Single Electron Trajectories - Two Dimensional Model Results

Examples of the 2-D plasma wave field and the trajectory of a single electron drifting transversely through a plasma wave are shown in figure 3.1. Figure 3.1(a) is the plasma wave field as seen by the electron as it drifts transversely across the plasma wave. The wave moves from bottom to top in the figure. Figure 3.1(b) is the trajectory of the electron going across the plasma wave, moving from left to right in the figure. The major features of the trajectory are: (a) the electron is wiggled in the direction of the longitudinal plasma wave field, (b) the electron has a small drift in the direction of the plasma wave velocity, and (c) as it exits the plasma wave the electron is deflected away at an angle from its initial direction of motion either upward or downward in the figure depending periodically on its phase of injection. All of these effects are due to the plasma wave's longitudinal electric field. The electron bunch's drift, which is generally just a fraction of a micron, would be difficult to measure in the laboratory. However, the deflection angle, which could result in large changes in the direction of an individual electron's trajectory after it exits the plasma wave, varies with the electron's injection position and energy, and also varies with the plasma wave's properties. The deflection angle depends on the phase at which the electron enters and exits the plasma wave, and therefore is influenced by the electrostatic field at the edges of the plasma wave which is weaker than the fields at the center of the wave. In an experimental situation, electrons in a bunch would enter the plasma wave at all phases and radii, and there would be a distribution of deflections, which appears as a change in the shape and size of the beam's cross section, or "spot". These changes will be studied using the 3-D simulations of the following section.

A qualitative summary the observed results of varying the plasma wave and electron beam parameters in the 2-D simulation is as follows. Increasing the plasma wave's amplitude causes the drift, deflection angle and wiggle amplitude to increase, but the wiggle period remains the same. Increasing the plasma wave's Gaussian width causes the drift and deflection angle to increase, but wiggle amplitude and period remain the same. Increasing the electron's injection energy causes the drift, deflection angle and wiggle amplitude to decrease, but the wiggle period remains the same. Increasing the plasma wave's wavelength causes the drift to increase and the deflection angle to increase.

3.4 Electron Bunch Spot Size Variations - Three Dimensional Model Results

In the 3-D simulation results discussed in this section, the electron bunch contains 5,000 particles which have a uniform random distribution along the direction (y) of the bunch's velocity and have a Gaussian random distribution in the directions transverse (x, z) to the bunch's velocity. The plasma wave's velocity is in the z direction. The Gaussian half width of the electron bunch and plasma wave are approximately 0.050 cm and 0.50 cm, respectively. The electron bunch is 10 mm

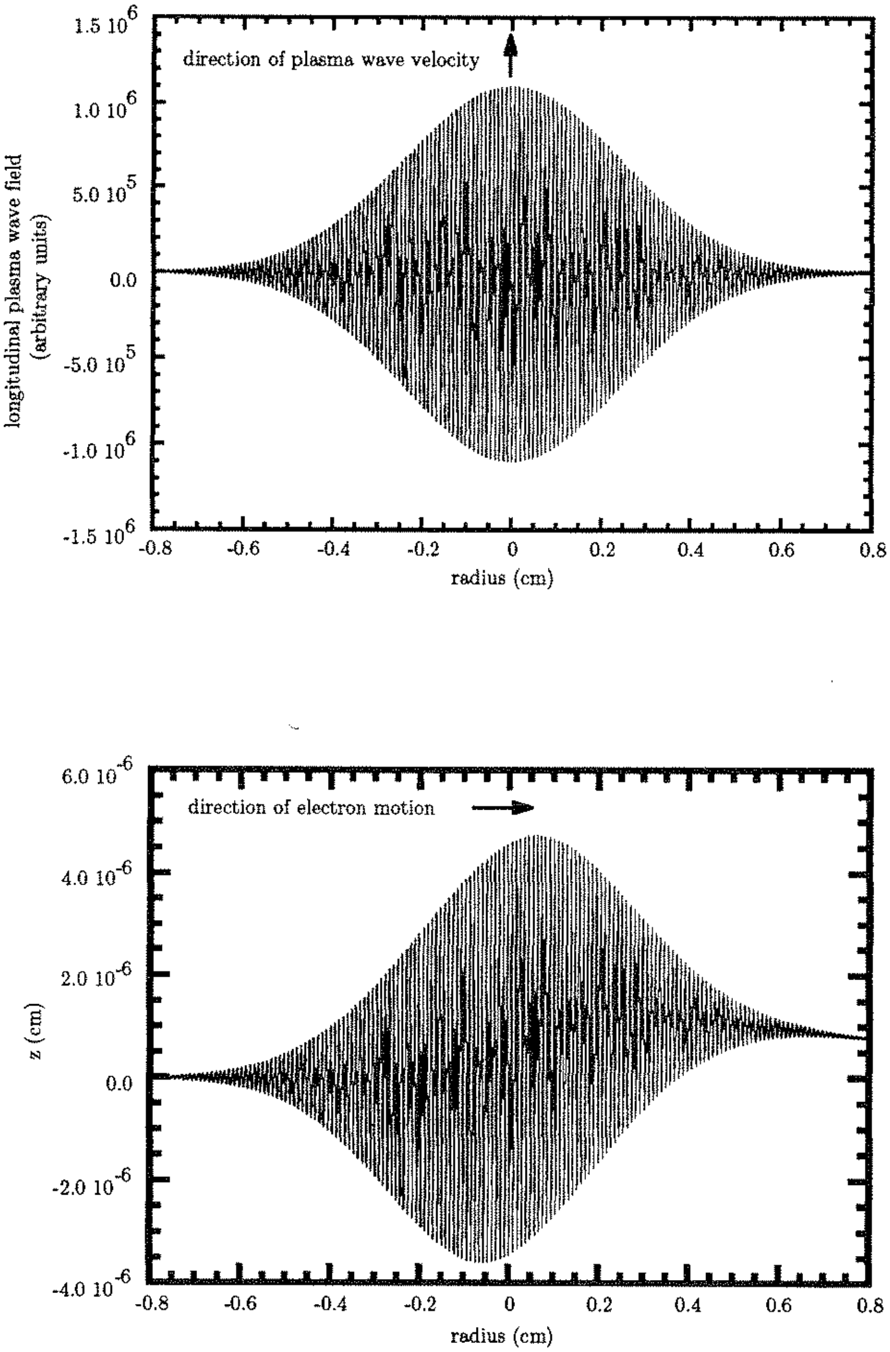

Figure 3.1: (a) The longitudinal electric field seen by the electron as it traverses the plasma wave and (b) the electron trajectory through the plasma wave. The plasma wave moves upward in (a) and the electron moves to the right in (b). Emittance $== 0$, $\gamma_o = 4$, $a_w = 1\%$ and $\gamma_p = 9.7$.

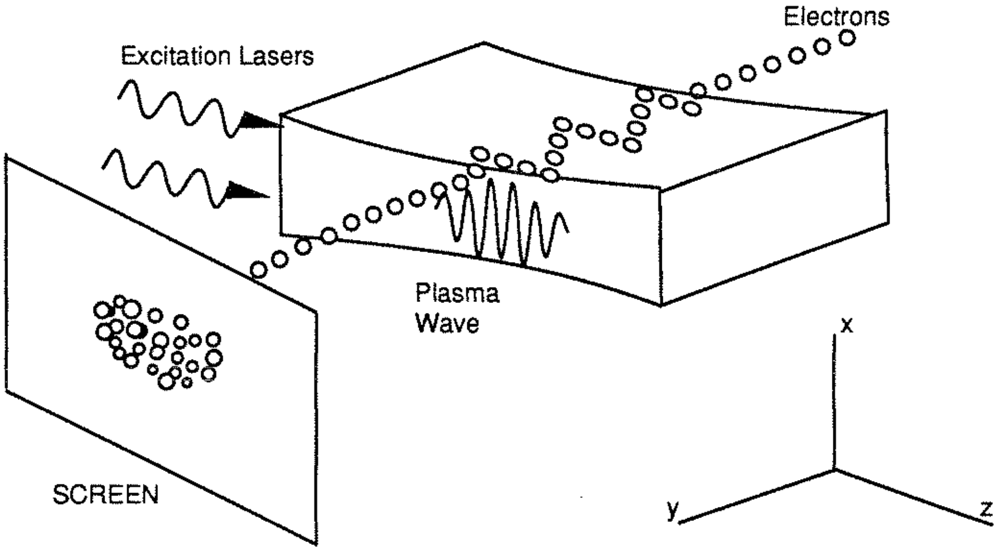

Figure 3.2: Geometry of plasma wave diagnostic scheme, showing propagation directions for the excitation lasers, plasma wave, and electron bunch.

long, which corresponds to an electron pulse period of 33 psec. At the start of the simulation, the front of the electron bunch is -0.75 cm from the centerline of the plasma wave, and at the end of the simulation the front of the bunch is approximately 10 cm past the centerline. Figure 3.2 shows the relationships between the directions of propagation of the excitation lasers, plasma wave and electron beam. Also shown is an idealization of the use of a "screen" to measure the electron bunch density distribution (spot size).

Figure 3.3 shows the effects of variations of plasma wave amplitude, or a_w, on the electron bunch density distribution when the emittance is zero. In this figure the pattern of scattered dots represents the electron distribution after the bunch has passed perpendicularly through the plasma wave and has drifted approximately 10 cm away from the wave's centerline. The electrons can be imagined to be collected on a "screen" as shown in figure 3.2. The plots show the end-on view of the bunch with the electrons moving up out of the plane of the figure while the plasma wave

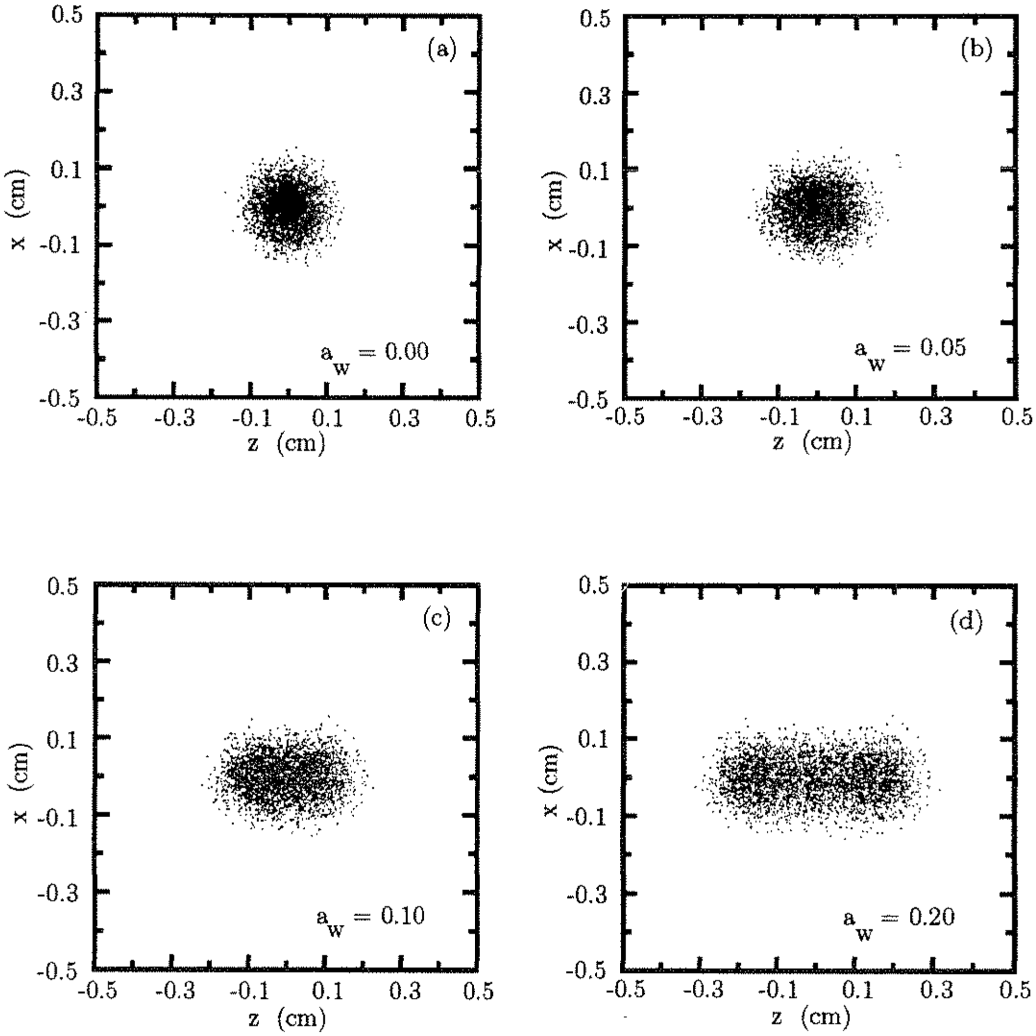

Figure 3.3: Variation of Electron Bunch Spot Size for $a_w = 0.0$, 0.05, 0.10 and 0.50. The plasma wave moves to the right in the figure and the electrons move out of the page.

moves from left to right. Figure 3.3(a) shows the electron distribution for fractional plasma wave amplitude equal to zero, which corresponds to no plasma wave present. This distribution is the original injected electron distribution, since the electrons travel in straight lines when the plasma wave amplitude and emittance are zero. Figures 3.3(b), (c), and (d) show the electron distributions when the plasma wave amplitude is increased to a_w = 5%, 10%, and 20%, respectively. We see that the bunch has been elongated (from about 2 mm to about 6 mm wide) in going from a_w = 0% to 20% fractional plasma wave amplitude. The elongation is in the z direction, parallel to the plasma wave motion, indicating that the spreading is due to the longitudinal plasma wave field. This elongation may have potential as a probe of the plasma wave amplitude. Figure 3.4 summarizes the change in transverse spot dimensions, x and z, of the electron bunch as a_w is increased. A statistical software package was used to measure the standard deviations in the x and z directions (i.e. "sigma x" and "sigma z") of the distribution of electron positions in the spot. Figure 3.4 shows that the spot width in the longitudinal field direction, z, increases approximately uniformly with a_w, while the spot width is almost constant in the transverse field direction, x.

Additional graphical studies (not shown) indicated that the radial plasma wave electric fields, E_x and E_y, had no effect on the longitudinal spreading of the electron bunch in the z direction, even for the very narrow plasma waves having 0.005 cm (0.5 λ_p) Gaussian half-width. For wide plasma waves the transverse E_x and E_y fields had very little effect on the electron bunch in the x and y directions, but for the very narrow wave in which E_x and E_y are large, changes in the transverse directions were observed. For very narrow plasma waves the electron bunch's distribution spreads in the x direction (vertical in the scatter diagrams) and in the y direction, but still remains very dense near the center. This is shown in figure 3.5, where the spreading

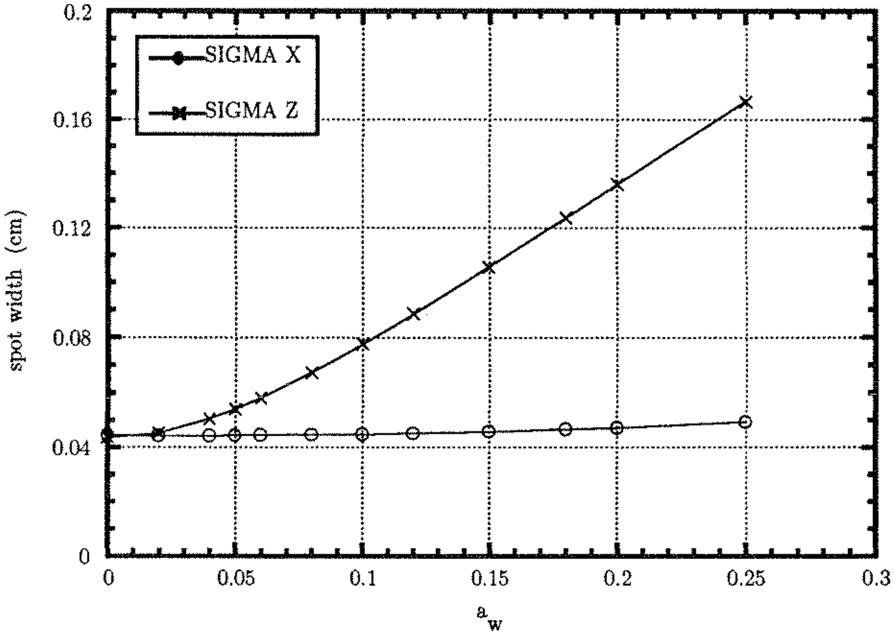

Figure 3.4: Summary of variation of electron bunch spot size with a_w. Emittance = 0, $\gamma_o = 4$, and $\gamma_p = 9.7$.

in the x direction is due to the radial field of a one λ_p wide plasma wave. Figure 3.6 summarizes the change in transverse spot dimensions, x and z, of the electron bunch as the width of the plasma wave is decreased. These results show that the RPW probably would not be suitable as a diagnostic of the longitudinal field or as a plasma wave undulator for plasma wave widths below about 5 λ_p. However the scattering of electrons from the beam might possibly be used as a diagnostic of the strong E_x radial field. The effect of the radial E_y field of a narrow wave would be to cause the shape of the electron bunch to have a conical leading edge (not shown), due electrons near the center of the bunch being accelerated ahead of the electrons near the edge. This shape change might possibly be used as a diagnostic of the strong E_y radial field of the plasma wave.

Also examined was the effect on the electron bunch distribution due to changes in the wavelength of the plasma wave, and it was found that longitudinal spreading

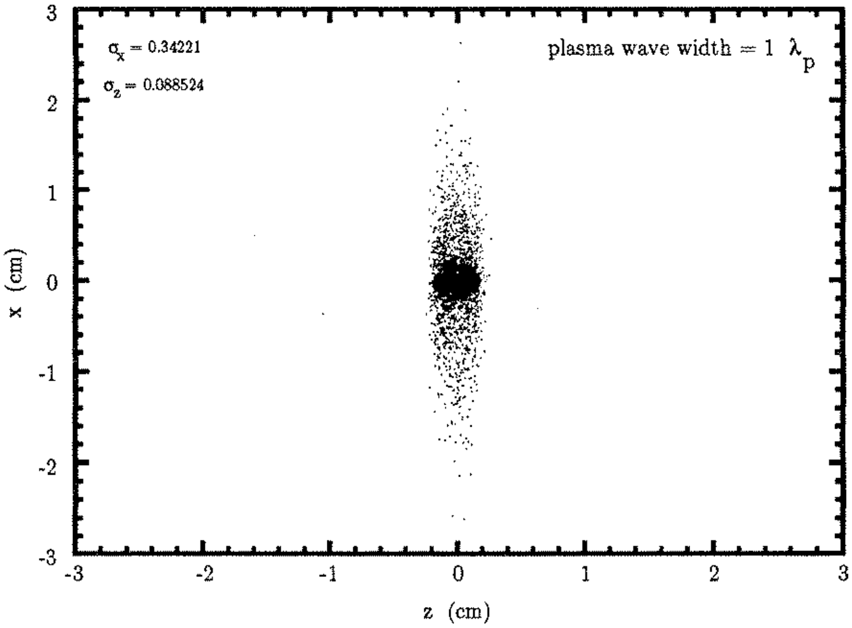

Figure 3.5: Effect of large radial field on electron bunch spot size. The plasma wave is one plasma wavelength wide. Emittance = 0, $\gamma_o = 4$, $\gamma_p = 9.7$ and $a_w = 10\%$.

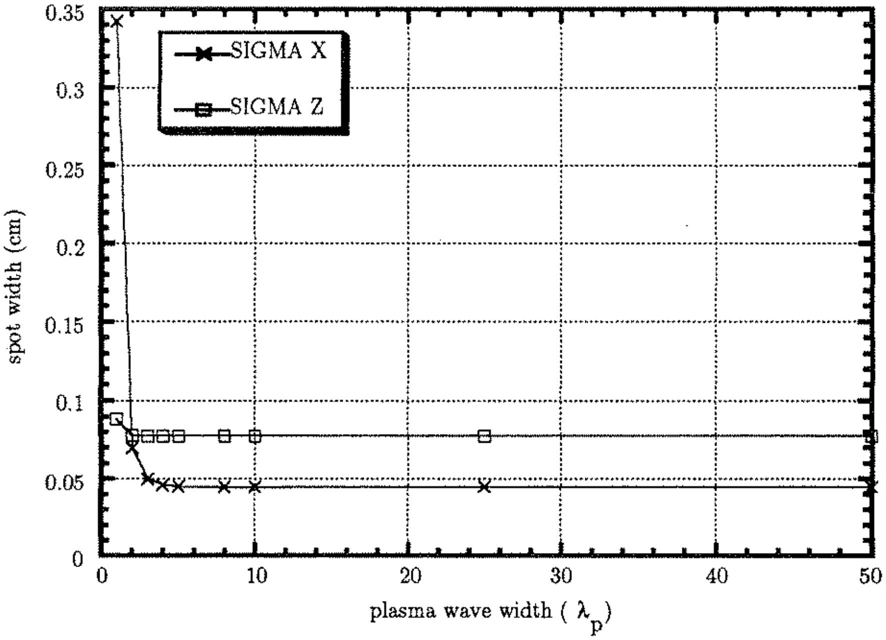

Figure 3.6: Summary of variation of electron bunch spot size with plasma wave width. Emittance = 0, $\gamma_o = 4$, $\gamma_p = 9.7$, and $a_w = 10\%$.

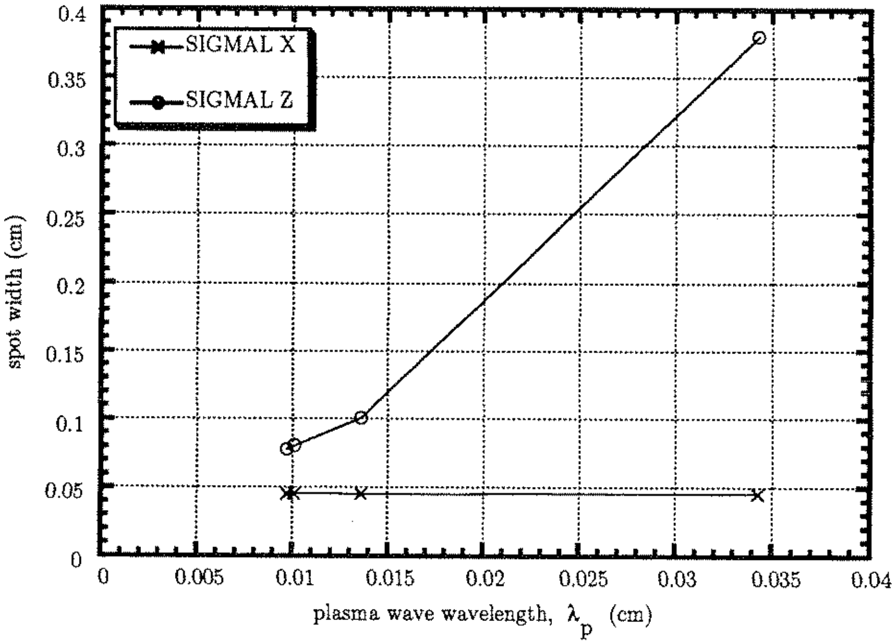

Figure 3.7: Summary of variation of electron bunch spot size with plasma wave wavelength. Emittance = 0, $\gamma_o = 4$, and $a_w = 10\%$.

increased approximately linearly with wavelength, for the case of no emittance, as shown in figure 3.7. The four wavelengths plotted in figure 3.7 correspond to the four laser beatwave combinations shown in Table A.2. This figure shows that this scheme possibly could be used as diagnostic of the plasma wave wavelength, provided that other variables, such as a_w and γ_o, were known.

Also examined was the effect on the electron bunch distribution due to changes in the electron energy, γ_o, as shown in figure 3.8. This figure shows that the difference in the x and z dimensions of the spot decreases as γ_o increases, indicating that the longitudinal plasma wave field has less effect on the spot size of more energetic beams. Therefore this diagnostic scheme is best suited for lower energy beams.

However, instead of spreading, at high energies ($\gamma_o \approx 100$) a bunching or grating pattern in the direction of the longitudinal field was observed in the spot distribution of the electron bunch, as shown in figure 3.9. The bunching or grating spacing is

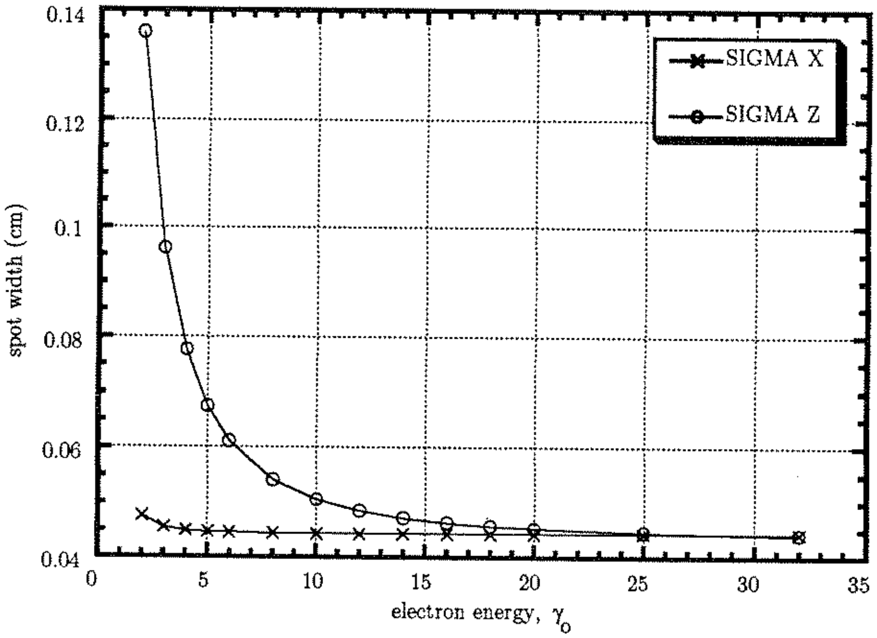

Figure 3.8: Summary of variation of electron bunch spot size with electron injection energy. Emittance = 0, $\gamma_p = 9.7$, $a_w = 10\%$.

the wavelength of the plasma wave. The change in the spot with γ_o can be seen by comparing figure 3.3(c) in which $\gamma_o = 4$, with figure 3.9(b) in which $\gamma_o = 100$, for the same plasma wave a_w, λ_p, and γ_p. The two figures are on the same scale and show that the longitudinal spreading is not present and that the grating appears at high electron energies. The spreading is due to the deflection of the electrons as they exit the wave in the region where the wave is smaller in magnitude. A higher energy electron would be less affected by the weaker fields at the plasma wave's edge and would spread less as shown in these figures. The bunching is probably due to the stronger plasma wave fields near the center of the wave, and is probably present even at lower electron energies, but is not visible because spreading causes electrons from neighboring bunches to cross each other as they exit the plasma wave. This grating phenomenon could possibly be used as a diagnostic of the plasma wave wavelength or could be used just to obtain a density modulated beam for some other application, such as a reflection grating or lithographic pattern making. Figure 3.9(a) is a view looking down on the electrons as they move upward in the figure and the plasma wave moves to the right. This figure shows that the grating runs the length of the pulse and appears straight and uniform.

The change in the energies of the electrons in the bunch after passing transversely through the plasma wave was also investigated using the model, for the case of no emittance. In one instance, all electrons were injected having $\gamma_o = 4.00$ and after drifting transversely through the plasma wave ($\gamma_p = 9.7$ and $\epsilon = 10\%$) the energy spread was found to be $3.96 < \gamma < 4.04$, or 2%. This energy spread is probably due to the E_y radial field and could possibly be used as a diagnostic of that field.

Also examined was the effect of changes in the electron bunch emittance on the bunch distribution. Figure 3.10 shows bunch distributions after having passed through a plasma wave of $a_w = 10\%$ and $\gamma_p = 9.7$, and four different values of beam emittance. Figure 3.10(a) is the bunch distribution when the initial emittance is zero, and is the same as figure 3.3(c) but on a different scale. In figures 3.10(b), (c) and (d) the emittance is increased to 10, 20, and 40 mm-mrad, respectively. Typical plasma wave experiments at UCLA utilize electron bunches having emittance on the order of 20 mm-mrad [8]. These figures show that the emittance of this magnitude randomizes away any coherent spatial structure in the bunch's distribution.

Figure 3.11 summarizes the change in the spot dimensions, x and z, of the electron bunch as the emittance is increased. Figure 3.11(a) shows that the increase in spot size in both dimensions is linear with emittance. However, figure 3.11(b) shows that there is a value of emittance, approximately one mm-mrad, below which the spot size is constant. This means that the preceding results of this chapter that required a zero emittance beam would probably be valid for a beam with emittance as high as one mm-mrad. In any case, improvements in electron beam sources, pos-

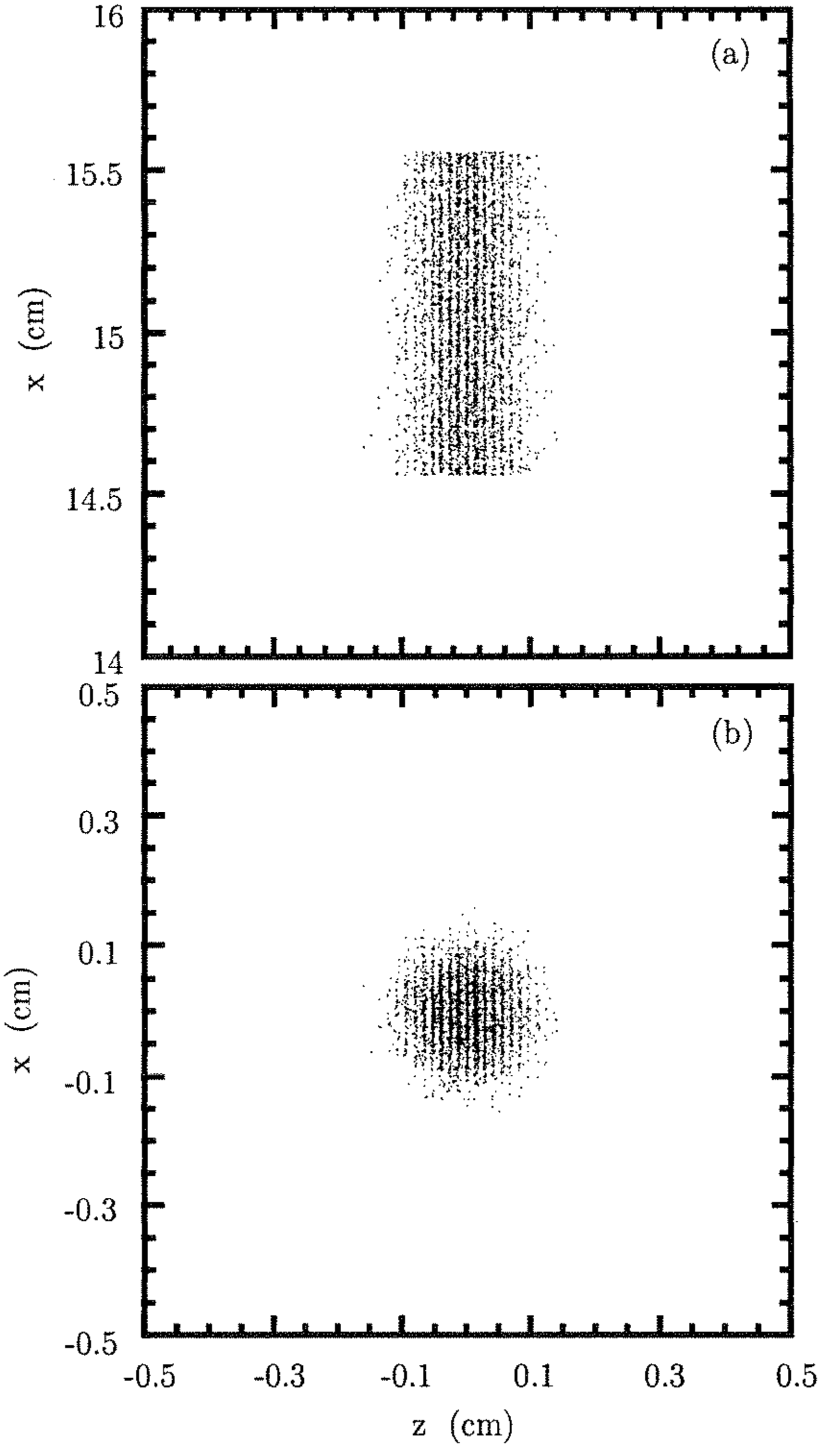

Figure 3.9: Electron bunch grating due to plasma wave at λ_p spacing (a) looking down on bunch as it moves up in the figure and (b) as bunch moves out of page. The plasma wave moves to the right in both figures. Emittance = 0, $\gamma_o = 100$, $a_w = 10\%$ and $\gamma_p = 9.7$

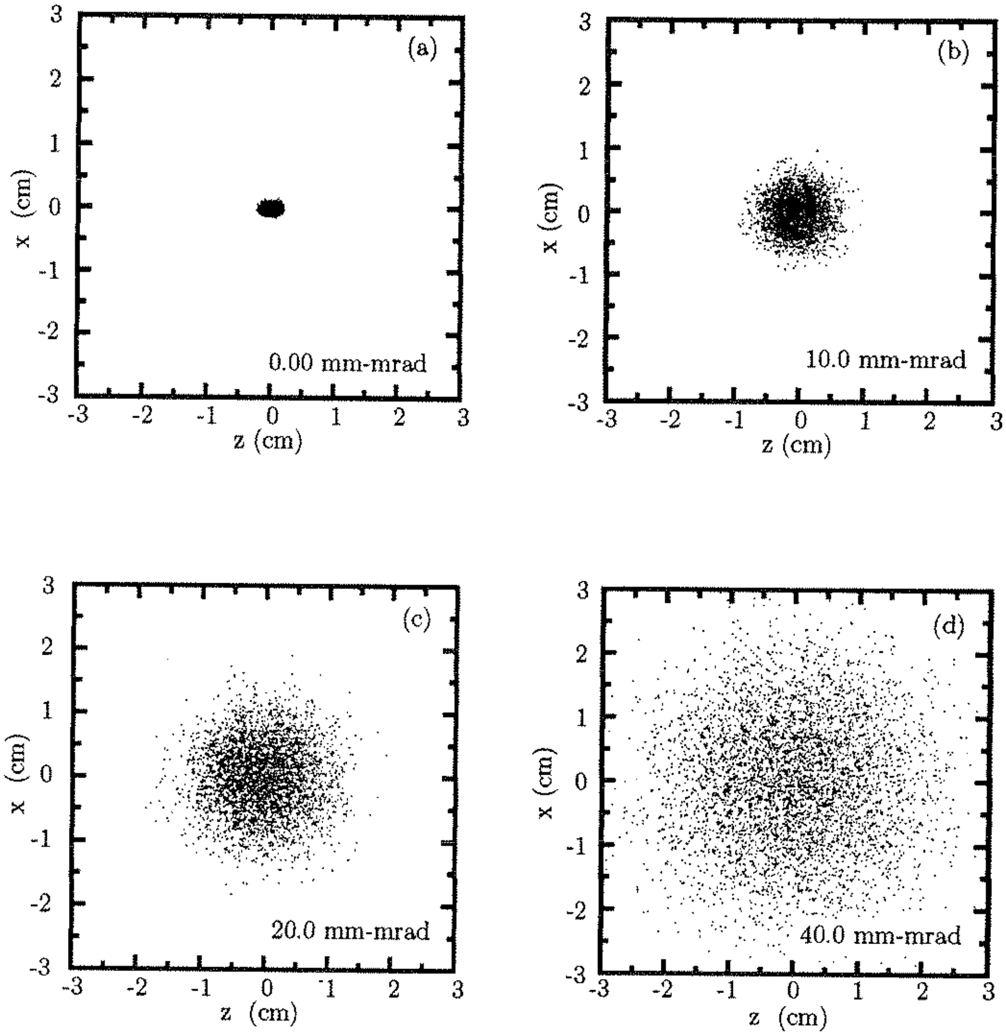

Figure 3.10: Variation of Electron Bunch Spot Size for emittance = 0, 10, 20 and 40 mm-mrad. The plasma wave moves to the right in the figure and the electrons move out of the page.

sibly utilizing laser driven photocathodes, would be required if transverse injection of a beam through a plasma wave is to be used as a diagnostic or as a plasma wave undulator.

3.5 Summary

The use of transversly injected electron bunches as a diagnostic of plasma wave properties has been shown by numerical simulation to be feasible in the limit of wide plasma waves and lower energy low emittance electron beams. The angular deflection in the z direction for a cold electron beam of energy γ_o injected across the plasma wave of amplitude a_w and wavelenth λ_p is summarized as

$$\Delta\theta \propto \frac{\kappa\lambda_p a_w}{\gamma_o} \tag{3.1}$$

where κ is a constant. The angluar deflection is greater than the angular spread of the incident beam of radius σ for normalized beam emittance of

$$\epsilon_n = \gamma\epsilon < \kappa\lambda_p a_w \sigma. \tag{3.2}$$

If larger beams are used, the allowable emittance before the structure is lost should increase in proportion to the beam size.

This study has revealed that this beam-wave interaction is rich in effects, including longitudinal and radial beam spot spreading, energy spreading, and beam grating formation. This study was an idealization in that it ignored such things as nonlinear plasma wave effects, plasma wave growth effects, electron beam collective effects and beam-plasma instabilities. In general, these effects would work to spoil the ideal results, however in some limits the ideal results may hold. The next step

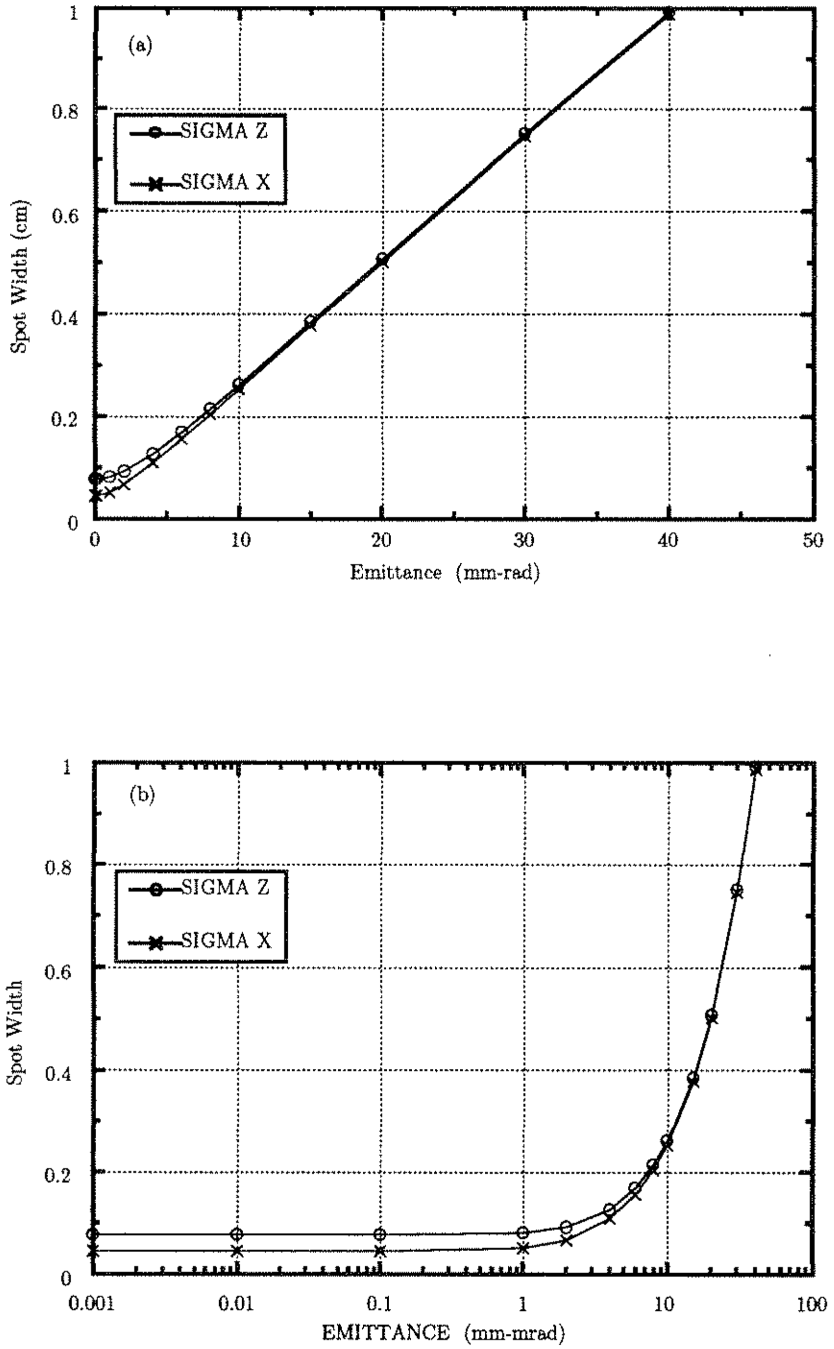

Figure 3.11: Variation of Electron Bunch Spot Size for emittance = 0, 10, 20 and 40 mm-mrad. The plasma wave moves to the right in the figure and the electrons move out of the page.

should be to refine the present results by including nonideal effects to determine the limits of applicablity. If the results are optimistic, perhaps experiments can be done to test this scheme as a diagnostic.

As far as the plasma wave undulator is concerned, the spatial spreading appears only after the electrons have drifted some distance beyond the plasma wave. The radiation is generated only during the short time the electron is inside the plasma wave. However, to minimize deflection of electrons from the bunch that might occur inside the wave, a wide plasma wave (having a small transverse electric field) and a relatively larger electron energy would be preferred.

Chapter 4

Studies of Classical Radiation Emission From Plasma Wave Undulators

4.1 Introduction

There is a significant ongoing research effort focused on producing short wavelength coherent radiation having wavelengths down to the x-ray regime using relativistic electron beams that oscillate in undulator fields. Many examples are found in the fields of free electron lasers and synchrotron radiation sources [30] [31]. It is well known that the radiated wavelength, λ_r, can be reduced by decreasing the undulator (wiggler) wavelength, λ_w, or by increasing the electron energy, γ, in accordance with the resonance relation:

$$\lambda_r \propto \frac{\lambda_w}{\gamma^2}. \tag{4.1}$$

The generation of coherent radiation in the x-ray regime using undulators was accomplished long ago by using large γ electron beams, but this was done at very large and expensive accelerator facilities [32]. It should be possible to reach the x-ray regime using less expensive and more compact low γ electron beam facilities by decreasing λ_w. In the original undulator and synchrotron radiation schemes, and in most configurations since then, magnetic field undulators were used [33][34][35]. In magnetic field undulators the minimum λ_w obtained currently is in the range of 0.1 to 1.0 cm, and is limited by the practical difficulty of placing very strong and very small permanent magnets or electromagnets close together in an alternating array. Among alternative approaches to decreasing λ_w are to replace the magnetic undulator with an electromagnetic wave undulator and with a crystal structure undulator, and much research is underway in these directions [36][37][38][39][40][41].

A different approach has been suggested for decreasing λ_w, which is to replace the magnetic undulator with an electrostatic plasma wave undulator. This potentially inexpensive and compact configuration is based on using a short wavelength large amplitude relativistic plasma wave as the undulator, through which is injected a modest energy but relativistic electron beam [28] [48]. In this scheme the electrons propagate parallel to the wavefronts of the plasma wave and emit radiation as they oscillate in the wave's alternating electrostatic field. Such large amplitude relativistic plasma waves can be excited readily by laser pulses or intense electron bunches and are being studied theoretically, computationally and experimentally by many researchers around the world [42]. In this chapter the characteristics of the classical radiation emitted by electrons in the plasma wave undulator are studied.

Figure 4.1 shows schematically the relationships among the propagation directions of the excitation lasers, plasma wave, electron beam, and radiation in this scheme. In this particular configuration the plasma wave is shown as if it were excited by laser beams as in the beatwave excitation scheme, however it also could have been excited by a short laser pulse (laser wakefield scheme) or by a short pulse of relativistic electrons (plasma wakefield scheme) propagating through a plasma.

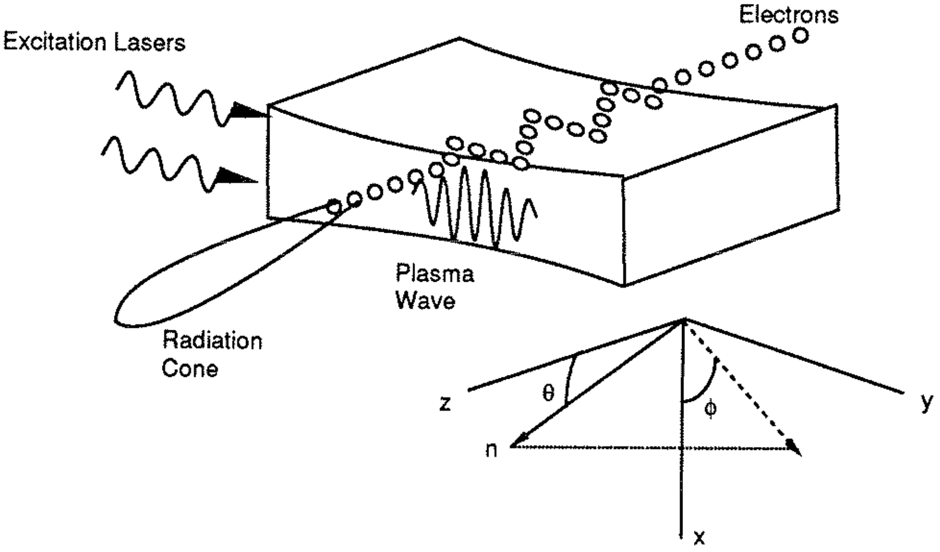

Figure 4.1: Undulator geometry, showing propagation directions of the excitation lasers, electron beam, plasma wave, and radiation.

The wiggling of an electron as it moves across a plasma wave undulator is described qualitatively by referring to figure 4.2, in which the potential contours of the plasma wave are shown to be very wide so that only the longitudinal electrostatic fields affect the electron motion. In the figure the plasma wave moves to the right at a phase velocity which is nearly equal to the speed of light while the electron moves downward also at nearly the speed of light. In figure 4.2(a) the longitudinal field deflects the electron to the left toward the potential minimum. In the time taken for the plasma wave to move to the right by one-half wavelength, the electron also moves across the wave vertically down a distance of one-half wavelength. This is because both wave and electron move at approximately the same speed. Therefore the undulator wavelength, λ_w, is effectively equal to the plasma wave's wavelength, λ_p. At its new location, figure 4.2(b), the electron is again deflected toward the potential minimum that is now to the right. This alternating or undulating motion continues as the electron passes across the plasma wave, figure 4.2(c).

Typical physical parameters for a plasma wave undulator are: undulator wavelength, $\lambda_w \approx 100$ μm; undulator strength, $a_w \geq 0.01$; number of undulations or wiggles, $N_w \approx 100$; and length of undulator, $L_w \approx 1.0$ cm. These are typical laboratory parameters for a wide beatwave excited relativistic plasma wave. An electron beam of 20 MeV ($\gamma = 41$) would emit 30 nanometer radiation in the above plasma undulator. The resonance relation, equation 4.1, is used to estimate the radiation wavelength. A single 30 picosecond micropulse of electrons (typical of a linac output) that passes across a 1.0 cm wide plasma undulator would emit a radiation pulse approximately 30 picoseconds in duration.

The maximum electrostatic fields in a relativistic plasma wave can be very large, equivalent in undulator strength to magnetic fields on the order of 1.0 megaGauss for 100 μm plasma waves. To show this we first note that a_w for the plasma undulator can be derived from Gauss' law and is

$$a_w = \frac{eE_o}{m_o c\,\omega_p} = \frac{E_o}{E_{max}} = \frac{n_1}{n_o} \tag{4.2}$$

where

E_o =amplitude of the plasma wave electrostatic field

E_{max} =maximum possible amplitude of an electrostatic field in a plasma for a given plasma density (or given plasma frequency)

ω_p =plasma frequency$= 4\pi n_o e^2/m_o$

e =electron charge

m_o =electron rest mass

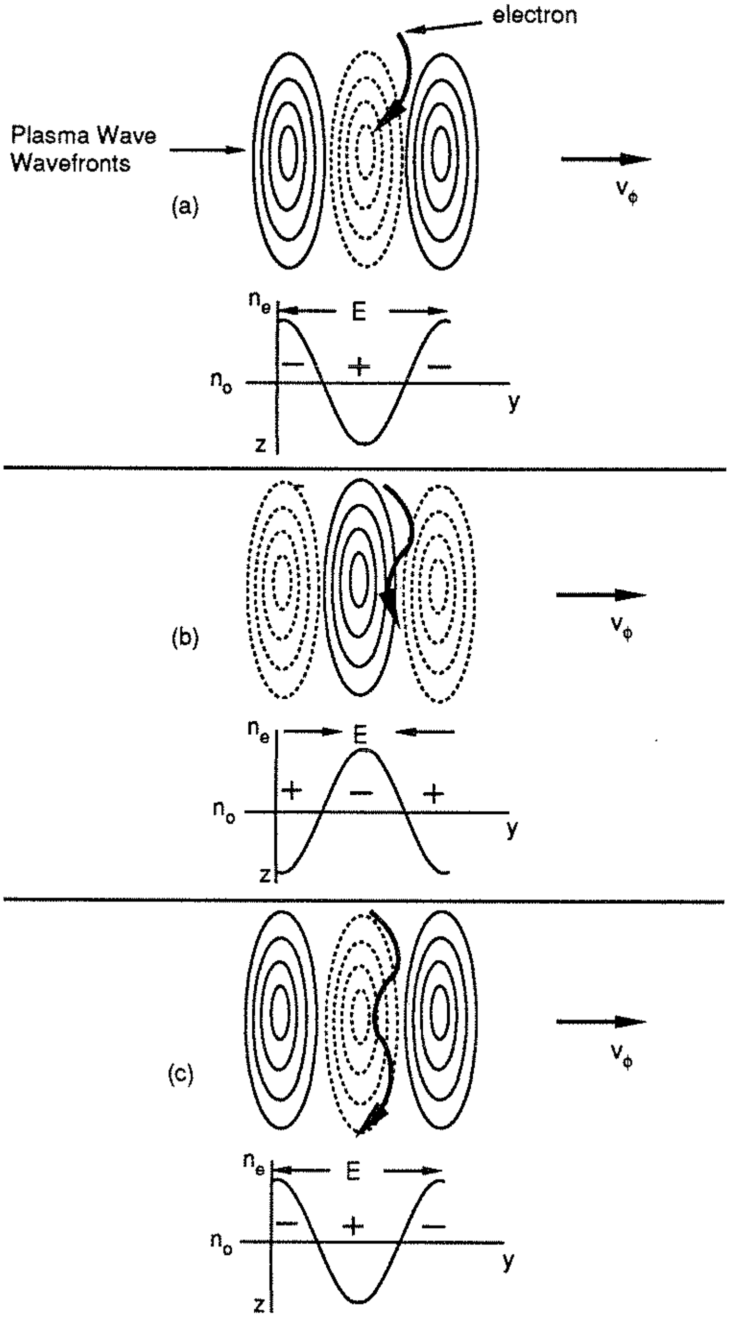

Figure 4.2: Electron's undulating trajectory in the potential countours of a plasma wave undulator.

c =speed of light

n_o =background plasma density

n_1 =perturbed plasma density

The maximum effective magnetic field of a plasma undulator can be estimated using

$$B_{ef} = \frac{2\pi m_o c^2}{e\lambda_p} a_w = \frac{10^4}{\lambda_w\ (cm)} = 3 \times 10^{-3}\sqrt{n_o(cm^{-3})} \tag{4.3}$$

or $B_{ef} \approx 9.5 \times 10^5$ Gauss for $a_w = 1.0$ and $\lambda_w = 100\ \mu$m. For comparison, in typical permanent magnet undulators the magnetic field is on the order of tens of kiloGauss and less. To get 30 nanometer radiation from a $\lambda_w = 1.0$ cm, $a_w = 1$ magnetic undulator would require an approximately 200 MeV electron beam. Equivalently, 20 MeV electron beam would radiate 3 μm radiation in this magnetic undulator.

The potential problems related to the facts that the electron beam can excite instabilities in the plasma and that the plasma wave's electrostatic fields can deflect the electron beam in undesirable ways must be considered in designing plasma wave undulators. In recent years some of these problems have been investigated theoretically and computationally and found not to be serious limitations provided that the electron beam is not too dense and that the plasma wave's transverse electrostatic fields are small. The limit on maximum electron beam density is imposed by the beam loading limit as discussed in Chapter 2 and reference [19]. Transverse electrostatic plasma wave fields should not be a problem as long as the plasma wave is much greater than five plasma wavelengths wide, as discussed in Chapter 3 and reference [29]. Our simulation results showed that electron beam quality is very important and that the beam emittance should be less than one mm-mrad for the example parameters discussed in this chapter. Methods for plasma wave excitation, calculations on the limitations of FEL action due to beam plasma interactions, and the parameters for radiation gain have been reported [28]. Some of the problems associated with building a uniform high density plasma source suitable for plasma wave undulators have been reported [43]. The problems of electron beam deflection due to the longitudinal and radial electrostatic fields in the plasma wave undulator, the effect of beam emittance, and the use of the deflected beam as a diagnostic of the plasma wave's electric field have also been studied through numerical calculations (Chapter 3 and reference [29]).

A plasma wave undulator in which an electron beam is injected antiparallel to the wave, and in which the transverse plasma wave fields wiggle the electrons, has been theoretically analyzed by Fedele et al.[44]. Fedele presented a fluid theory, discussed intrinsic efficiency, emittance, self pinching, and alternate configurations. A plasma wave undulator in which a relativistic electron beam excites the wave in a cylindrical plasma column has been investigated theoretically by Lalita et al.[45]. Lalita presented an instability analysis and discussed radiation guiding. A magnetostatic plasma undulator scheme that does not involve plasma waves, but makes use of stationary rows of laser produced plasma spots (effective $\lambda_w \approx 100\ \mu$m) that are formed on a flat solid target has been reported, along with reports of measurements of megaGauss fields [46],[47]. Another undulator scheme has been suggested by Yan and Dawson, called the "*ac* Free-Electron Laser", in which an electron beam propagates through a "temporally oscillating but spatially uniform transverse electric or magnetic structure"[48]. Yan and Dawson obtained the radiation dispersion relation, expressions for the growth rate and efficiency, and discussed design criteria for an experiment. One of their suggested configurations is to propagate an electron beam parallel to the wavefronts of a plasma wave, which is the plasma wave undulator discussed herein. We note that in order to have a significant electric field the plasma wave must have a phase velocity close to that of light. In such a plasma wave, the particle trajectories are going to be somewhat different than in the purely oscillating (*ac*) case. In this chapter a single electron analysis of the *ac* FEL undulator will be presented concurrently with the analysis of the plasma wave undulator. Finally, we note that a fluid theory analysis of the *ac* FEL has also been reported[49], and further work on enhancing the output power of an *ac* Raman FEL has been reported[50].

As stated earlier, the relativistic plasma waves may be produced by laser beatwave excitation, laser wakefield excitation or plasma wakefield excitation. Some typical plasma wave undulator wavelengths that can be obtained using laser plasma beatwave excitation are as follows (see Table 2.1). Using laser wavelengths of 9.6 and 10.6 μm gives $\lambda_w \approx 97$ μm; using 9.6 and 10.3 μm laser wavelengths gives $\lambda_w \approx 135$ μm; using 10.3 and 10.6 μm laser wavelengths gives $\lambda_w \approx 343$ μm; and using 1.05 and 1.06 μm laser wavelengths gives $\lambda_w \approx 101$ μm.

In section 4.2 are described the plasma wave equations, equation of motion and details of the 3-D simulation model. In section 4.3 are described the perturbation techniques used to obtain analytic equations for the electron trajectories. These trajectories are plotted and compared with the simulation results. In section 4.4 are described the derivations of the approximate equations for the spontaneous radiation from which are obtained the frequency spectra and angular distributions for different harmonic numbers. The analytic results are plotted and compared with computer simulations. In section 4.5 is described the derivation of the approximate analytic equations for the stimulated radiation gain which is due to a copropagating electromagnetic wave. The gain versus time and versus detuning are plotted and compared with the simulation results. Electron bunching due to the copropagating electromagnetic wave is also described. Section 4.6 is the conclusion. Many of the techniques followed herein for analyzing the plasma wave undulator, and much of the notation, are based on the free electron laser theory developed by Colson[51] [52].

4.2 The Plasma Wave Equations and the Simulation Model

The relativistic electrostatic plasma wave is assumed to be infinite in length, finite in width and moving in the $+y$ direction in this model. The relativistic electrons are injected in the $+z$ direction perpendicularly through the plasma wave as shown in figure 4.1. The electron's initial velocity is parallel to the plasma wave's wavefronts. The oscillating longitudinal field, E_y, of the plasma wave is responsible for the undulating motion of the electrons in the $\pm y$ direction. The oscillating transverse fields, E_x and E_z, of the plasma wave are perpendicular and parallel, respectively, to the electrons' initial velocities, and have negligible effect on their motion. This is because the plasma wave is wide (Gaussian half width $R = 50\lambda_p \approx 0.5$ cm) and therefore the transverse fields are small. The relativistic equation of motion for the electrons and the equations for the longitudinal and transverse electrostatic plasma wave field components are the same as used in Chapter 2 and 3. We use equations 2.22, 2.22, and 2.22, except that the equation subscripts are renamed to be compatible with coordinate definitions shown in figure 4.1. The electron beam model assumes point charges which interact with the electrostatic fields of the plasma wave but which do not interact with each other through space charge forces. Radiation damping is considered to be negligible.

In the 2-D simulation, a single electron is injected into the plasma wave from a position far from the centerline of the wave ($z \approx -3R$, where R is the Gaussian width of the plasma wave). The electron's position (x, y, z), velocity $(\beta_x, \beta_y, \beta_z)$, and acceleration $(\dot{\beta}_x, \dot{\beta}_y, \dot{\beta}_z)$ are calculated along the trajectory until the electron reaches the opposite side of the wave ($z \approx +3R$). The electron is injected at time equal zero with phase equal zero with respect to the plasma wave (i.e. $y(0) = 0$). The trajectory of the electron and the electrostatic field it sees are shown in figure 3.1.

In the 3-D simulation a micropulse of thousands of electrons is injected into the plasma wave so that the front of the micropulse starts at $z \approx -3R$. The spatial distribution of electrons in the micropulse is determined by a uniform random number generator for the direction of beam propagation, z, and is determined by a Gaussian random number generator for the perpendicular directions, x and y. The electron micropulse has a Gaussian halfwidth of $5\,\lambda_p$ in the x and y directions. Each electron's position, velocity and acceleration are calculated along the trajectory until the rear of the bunch reaches the opposite side of the wave ($z \approx +3R$). Electron beam emittance can be included and is used to determine an initial perpendicular deflection for each electron using a Gaussian random number generator as described previously in Chapter 2 (equation 2.26) and reference [25]

4.3 Electron Trajectories

Approximate equations for the electron trajectories in the plasma wave undulator are obtained by substituting a simplified expression for the plasma wave field into the relativistic equation of motion and solving it by perturbation. The lowest order approximation of the electron trajectory in the plasma wave undulator is also the approximate electron trajectory in an *ac* FEL undulator. The *ac* FEL undulator is spatially uniform, has $k_p = 0$ and oscillates at frequency ω_p.

The plasma wave fields (equations 2.22, 2.23, and 2.24) were simplified by assuming that the laser pump field or electron quiver velocity is small (α_{em} is small) and that the plasma wave is wide (R is large). Then the predominant plasma wave field component acting on the electron in the laboratory frame is

$$E_y = \frac{a_w m_o c \omega_p}{e} \cos(k_p y - \omega_p t) = E_o \cos(k_p y - \omega_p t). \tag{4.4}$$

The trajectory is found by solving the Lorentz force equation,

$$\frac{d\overline{v}(t)}{dt} = \frac{e}{\gamma m_o}\left[\overline{E} - \frac{\overline{v}\left(\overline{v}\cdot\overline{E}\right)}{c^2}\right], \tag{4.5}$$

where $E = E_y$ and the velocity is expanded in terms of the small parameter, ε,

$$\overline{v} = \overline{v}_o + \varepsilon\, \overline{v}_1 + \varepsilon^2\, \overline{v}_2 + \cdots. \tag{4.6}$$

First equation 2.22 (with subscript changed from z to y) is approximated by $E_y = E_o \cos(\omega_p t)$, and the equation of motion is solved to obtain the following electron trajectory:

$$\overline{r}(t) = v_o t\, \hat{z} + \frac{a_w c}{\gamma_o \omega_p}(1 - \cos\omega_p t)\, \hat{y} + \frac{a_w^2 v_o}{4\gamma_o^2 \omega_p} \sin 2\omega_p t\, \hat{z} + \cdots. \tag{4.7}$$

Note that the first term is the zeroth order drift, the second term is the first order transverse oscillation at frequency ω_p and the third term is a second order longitudinal oscillation at $2\omega_p$ (the second harmonic term). The velocity, $\overline{\beta}$, is found by differentiating $\overline{r}(t)$ and dividing by c. Equation 4.7 is rewritten in a convenient form for graphing using the dimensionless units

$$\tau = t\frac{\beta_o c}{N_w \lambda_p} \quad \text{and} \quad \Omega_p = \omega_p \frac{N_w \lambda_p}{\beta_o c}, \tag{4.8}$$

and becomes the trajectory in units of the length of the undulator, $N_w\lambda_p$,

$$\frac{\overline{r}(\tau)}{N_w\lambda_p} = \tau\hat{z} - \frac{a_w}{\gamma_o\beta_o\Omega_p}\left(\cos\Omega_p\tau - 1\right)\hat{y} + \frac{a_w^2}{4\gamma_o^2\Omega_p}\sin 2\Omega_p\tau\ \hat{z} + \cdots \tag{4.9}$$

where $\beta_o = \sqrt{1 - 1/\gamma_o^2}$. Equation 4.7, or 4.9, is the approximate equation for the electron trajectory in an *ac* FEL undulator.

Next, in order to obtain the approximate electron trajectory in a plasma wave undulator ($k_p \neq 0$), the y component of equation 4.7 is substituted into equation 4.4 to obtain

$$E_y = E_o \cos\left(\frac{k_p a_w c}{\gamma_o\omega_p}\left(1 - \cos\omega_p t\right) - \omega_p t\right). \tag{4.10}$$

The trig terms are expanded as a series in $J_n(\nu)$, keeping only the lowest order terms, where J_n is the n^{th} order Bessel function of the first kind. Equation 4.10 is then substituted into the equation of motion which is again solved by perturbation. The resulting approximate equation for the electron trajectory in a plasma wave undulator in dimensionless units is

$$\frac{\overline{r}(\tau)}{N_w\lambda_p} = \tau\hat{z} + \frac{a_w}{\gamma_o\beta_o\Omega_p}\left\{J_o(\nu)\left(-\cos(\nu - \Omega_p\tau) + \cos\nu + \Omega_p\tau\sin\nu\right)\right.$$
$$\left. + \frac{1}{4}J_1(\nu)\left[2\Omega_p^2\tau^2\sin\nu - \sin(\nu - 2\Omega_p\tau) + \sin(\nu) - 2\Omega_p\tau\cos(\nu)\right]\right\}\hat{y} + \cdots \tag{4.11}$$

where $\nu = k_p c a_w/\omega_p\gamma_o$. In this approximation the plasma wave field was assumed to be linear and thus was not expanded in terms of its harmonics. Using fields expanded in higher harmonics would produce additional terms in the above expressions at the respective harmonics (see Appendix F and [53]). The expressions for the trajectory and velocity obtained in this section will be used in the next section to calculate the radiation analytically.

The dimensionless electron trajectory in a plasma wave undulator, equation 4.11, is plotted in figure 4.3. Electrons enter the undulator at $\tau = 0$ and exit at $\tau = 1$. However in order to spatially resolve the electron undulations, only the first 30% of the undulator is plotted. In figure 4.3 the undulating electrons drift in the direction that the plasma wave moves and the amount of drift increases with a_w and decreases with γ. In the simulation, the original unsimplified expressions for the plasma wave fields (equations 2.22, 2.23, and 2.24) were numerically integrated to obtain the lab frame trajectory. The lab frame trajectory calculated by simulation is shown in figure 3.1(b) which also shows a drift in the direction of the plasma wave motion, in qualitative agreement with the analytic result, figure 4.3. The Gaussian profile of the plasma wave field used in the simulation causes the drift to be more gradual at the edges of the plasma wave. The simulation also shows that there is a deflection of the electron from its initial direction of motion that results as the electron exits the plasma wave, as was discussed in Chapter 3 and reference [25]. The analytic trajectory of an electron through the *ac* FEL looks similar to figure 4.3, except that there is no transverse drift.

4.4 Spontaneous Radiation

The approximate equations for the frequency spectrum and angular distribution of radiation emitted by an electron in a plasma wave undulator are found by substituting the equations for $\overline{r}$ and $\overline{\beta}$ into the well known expression for the intensity, I, of the radiation emitted per solid angle, $d\Omega$, and frequency interval, $d\omega$,[54]

$$\frac{d^2 I}{d\Omega d\omega_r} = \frac{e^2 \omega_r^2}{4\pi^2 c} \left| \int_{-\infty}^{+\infty} \hat{n} \times \left(\hat{n} \times \overline{\beta}(t) \right) e^{i\omega_r (t - \hat{n}\cdot\overline{r}(t)/c)} dt \right|^2 \tag{4.12}$$

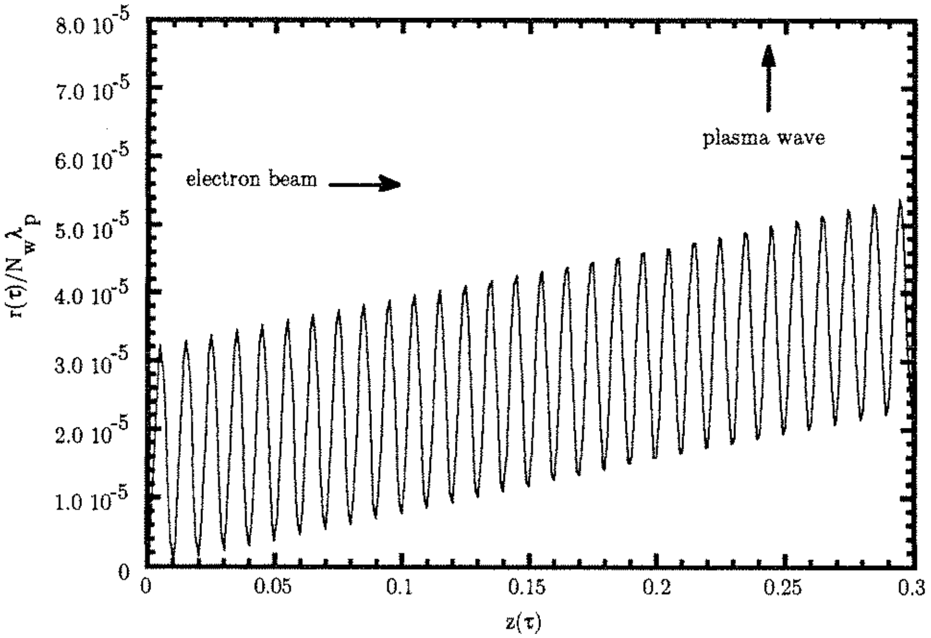

Figure 4.3: Analytic electron trajectory in a plasma wave undulator.

where $\hat{n} = \sin\theta\cos\phi\,\hat{x} + \sin\theta\sin\phi\,\hat{y} + \cos\theta\,\hat{z}$, and θ, ϕ, and $\hat{n}$ are defined in figure 4.1. We integrate analytically over the finite interval $|t| < N_w\pi/\beta_o\omega_p$ because the radiation emitted during the time the electron is outside the undulator is zero. The radiation of harmonic number f_i ($i = 1, 2, 3, \ldots$) from an electron in the plasma wave undulator is then

$$\left.\frac{d^2I}{d\Omega d\omega_r}\right|_{f_i} = \frac{e^2}{4\pi^2 c}\left[\frac{\sin\left(\frac{\omega_r}{\omega_p}\left(1-\beta_o\cos\theta\right)+\Delta-f\right)\frac{N\pi}{\beta_o}}{\left(\frac{\omega_r}{\omega_p}\left(1-\beta_o\cos\theta\right)+\Delta-f_i\right)\omega_p}\right]^2\left(\frac{f_i}{1-\beta_o\cos\theta}\right)$$

$$\times\left(\sin^2\theta\,PP^* + \frac{i}{2}\sin 2\theta\,\sin\phi\,\left(P^*Q - PQ^*\right) + \left(1-\sin^2\theta\right)\sin^2\phi\;QQ^*\right) \quad (4.13)$$

where

$$P = 2\beta_o\left(A_o + B_n^+\right) + \frac{\alpha^2 J_o^2(\alpha)\beta_o}{4}\cos 2\alpha\left(A_2^+ + B_{n+2}^+ + B_{n-2}^+\right) \quad (4.14)$$

$$Q = \alpha A_1^- + \alpha J_o^2(\alpha)\cos\alpha\left(B_{n+1}^- - B_{n-1}^-\right) \tag{4.15}$$

$$A_o = J_o(\alpha)\sum_{m=-\infty}^{m=+\infty} J_m(\kappa)\delta_{(2m,f)} \tag{4.16}$$

$$A_\eta^\pm = J_o(\alpha)\sum_{m=-\infty}^{m=+\infty} J_m(\kappa)\left(\delta_{(2m+\eta,f)} \pm \delta_{(2m-\eta,f)}\right) \tag{4.17}$$

$$B_\eta^\pm = \sum_{n=1}^{n=+\infty} i^n J_n(\lambda)\sum_{m=-\infty}^{m=+\infty} J_m(\kappa)\left(\delta_{(2m+\eta,f)} \pm \delta_{(2m-\eta,f)}\right) \tag{4.18}$$

$$\alpha = \frac{k_p\, c\, a_w}{\omega_p \gamma_o}, \tag{4.19}$$

$$\kappa = \frac{a_w^2 J_o^2(\alpha)\beta_o\omega_r}{\omega_p}\cos 2\alpha\ \sin\theta\ \sin\phi \tag{4.20}$$

$$\lambda = \frac{a_w J_o(\alpha)\beta_o\omega_r}{\omega_p}\cos\alpha\ \sin\theta\ \sin\phi \tag{4.21}$$

$$\Delta = \frac{\alpha J_o(\alpha)\beta_o\omega_r}{\omega_p}\sin\alpha\ \sin\theta\ \sin\phi \tag{4.22}$$

$i = \sqrt{-1}$, * signifies complex conjugate and δ is the Kronecker delta. Here we have neglected the harmonic content of the plasma wave undulator itself, however see Appendix F. The radiation of harmonic number f_i emitted by an electron in the *ac* FEL undulator can be obtained also and it is

$$\left.\frac{d^2I}{d\Omega d\omega_r}\right|_{f_i} = \frac{e^2}{4\pi^2 c}\left[\frac{\sin\left(\frac{\omega_r}{\omega_p}\left(1-\beta_o\cos\theta\right)\ - f\right)\frac{N\pi}{\beta_o}}{\left(\frac{\omega_r}{\omega_p}\left(1-\beta_o\cos\theta\right)\ - f_i\right)\omega_p}\right]^2\left(\frac{f_i}{1-\beta_o\cos\theta}\right)$$

$$\times\left(\sin^2\theta\, PP^* + \frac{i}{2}\sin 2\theta\ \sin\phi\ \left(P^*Q - PQ^*\right) + \left(1-\sin^2\theta\right)\sin^2\phi\ \ QQ^*\right) \tag{4.23}$$

where

$$P = 2\beta_o\left(A_o + B_n^+\right) + \frac{\alpha^2\beta_o}{2}\left(A_2^+ + B_{n+2}^+ + B_{n-2}^+\right) \tag{4.24}$$

$$Q = \alpha\left(A_1^- + B_{n+1}^- - B_{n-1}^-\right) \tag{4.25}$$

$$A_o = J_o(\alpha) \sum_{m=-\infty}^{m=+\infty} J_m(\kappa)\delta_{(-2m,f)} \tag{4.26}$$

$$A_\eta^{\pm} = J_o(\alpha) \sum_{m=-\infty}^{m=+\infty} J_m(\kappa) \left(\delta_{(-2m+\eta,f)} \pm \delta_{(-2m-\eta,f)}\right) \tag{4.27}$$

$$B_\eta^{\pm} = \sum_{n=1}^{n=+\infty} i^n J_n(\lambda) \sum_{m=-\infty}^{m=+\infty} J_m(\kappa) \left(\delta_{(-2m+\eta,f)} \pm \delta_{(-2m-\eta,f)}\right) \tag{4.28}$$

$$\lambda = \frac{a_w \beta_o \omega_r}{\omega_p} \sin\theta \, \sin\phi \tag{4.29}$$

$$\kappa = \frac{a_w^2 \beta_o \omega_r}{8\omega_p} \cos\theta \tag{4.30}$$

$$k_p = 0 \quad and \quad \Delta = 0. \tag{4.31}$$

The single electron radiation intensity as a function of observation angle, θ, and frequency ratio, ω_r/ω_p, up to the second harmonic component is shown in figure 4.4 for the plasma wave undulator and, for comparison, in figure 4.6 for the *ac* FEL undulator. The angle is plotted in the range $|\theta| < 1/\gamma$, the harmonics correspond to $f_1 = 2\gamma^2$, $f_2 = 4\gamma^2$ and $f_3 = 6\gamma^2$, and $\phi = \pi/2$. The radiation is plotted in units of $(e^2/4\pi^2 c)$. The figures show that the radiation is centered about $\theta = 0$ in the *ac* FEL undulator but it is skewed in the $-\theta$ direction in the plasma wave undulator. This is because of the drift of the electrons in the direction of the phase velocity of the plasma wave. There is also a reduction in the magnitude of the radiation as the harmonic number increases for both undulators. Expressions similar to equation 4.13 were obtained by Colson for the linearly polarized and circularly polarized magnetic undulators [51][55]. These different undulator configurations have very similar radiation characteristics due to the similarity of their line shape functions. They are all characterized by regularly spaced radiation peaks, which decrease in frequency and amplitude as the angle of observation varies away from the forward direction, $\theta = 0$. The skewing of the plasma undulator's radiation is due to the Δ term in the line shape function which depends on k_p through the α term. By rotating the $dI/d\Omega d\omega$ figures, one obtains the angular distribution, $dI/d\Omega$, or the frequency spectrum, $dI/d\omega$, which are shown in figures 4.5 and 4.7 for the fundamental harmonic of the plasma wave undulator and *ac* FEL, respectively. Figure 4.6 shows that the *ac* FEL radiates the first and third harmonics on axis ($\theta = 0$), but the second harmonic is radiated off axis. In general, the odd harmonics are radiated on axis and the even harmonics are radiated off axis for *ac* FEL as well as the linear magnetic undulator. The circularly polarized undulator radiates only the fundamental on axis and all higher harmonics are radiated off axis [51][56].

In the simulation the radiation intensity for the plasma wave undulator was obtained by substituting $\overline{r}$, $\overline{\beta}$ and $\dot{\overline{\beta}}$ for each electron trajectory point into the well known expression for the radiation emitted per solid angle and frequency interval given by [54]

$$\frac{d^2I}{d\Omega d\omega} = \frac{e^2}{4\pi^2 c}\left|\int_{-\infty}^{+\infty} \frac{\hat{n}\times\left[\left(\hat{n}-\overline{\beta}(t)\right)\times\dot{\overline{\beta}}(t)\right]}{\left(1-\overline{\beta}(t)\cdot\hat{n}\right)^2} e^{i\omega(t-\hat{n}\cdot\overline{r}(t)/c)}dt\right|^2 . \tag{4.32}$$

To obtain $dI/d\omega$ we numerically integrated equation 4.32 over the trajectory, squared it, and integrated over the solid angle (with $\phi = \pi/2$). The single electron $dI/d\omega$ is shown in figure 4.8 for the fundamental frequency and zero beam emittance case, which qualitatively compares well with the approximate theoretical result for $dI/d\omega$ shown in figure 4.5(a). It was found in the simulations that as the number of electrons increased by N, the radiation in the peak at $\theta = 0$ increased as N^2 and the width of the peaks decreased as $N - 1$. It was also found that as the emittance was increased to values above one mm-mrad, the radiation peak at $\theta = 0$ decreased in magnitude and the discrete spectral pattern became smeared out. This is in

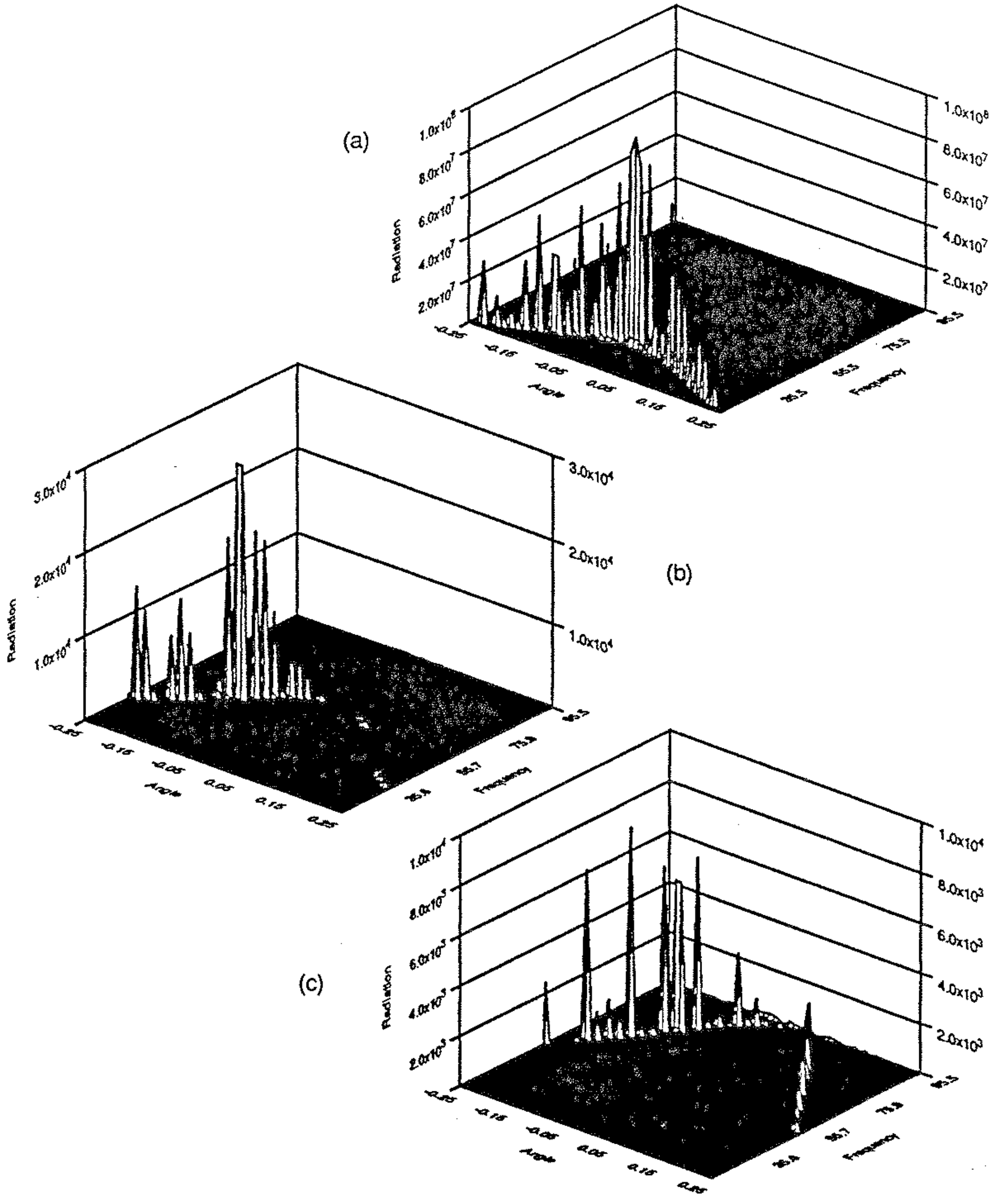

Figure 4.4: Radiation emitted by the plasma wave undulator versus frequency and angle for the (a) fundamental, (b) first harmonic, and (c) second harmonic. $\gamma_o = 4$, $a_w = 0.1$, $(-1/\gamma < \text{angle} < 1/\gamma)$, $(\gamma < \text{frequency} < 6\gamma)$, and $\phi = \pi/2$.

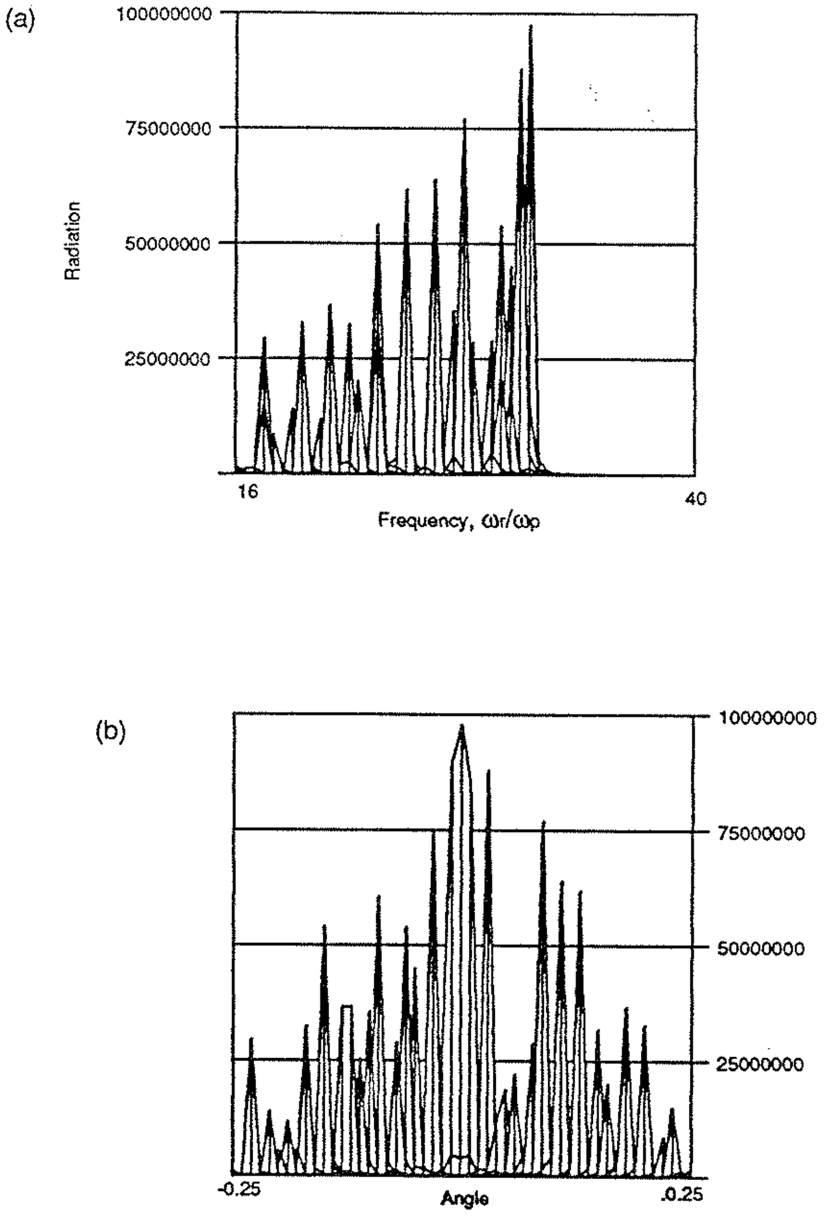

Figure 4.5: Radiation spectrum and angular distribution in the plasma wave undulator for the fundamental frequency (same conditions as in figure 4.4).

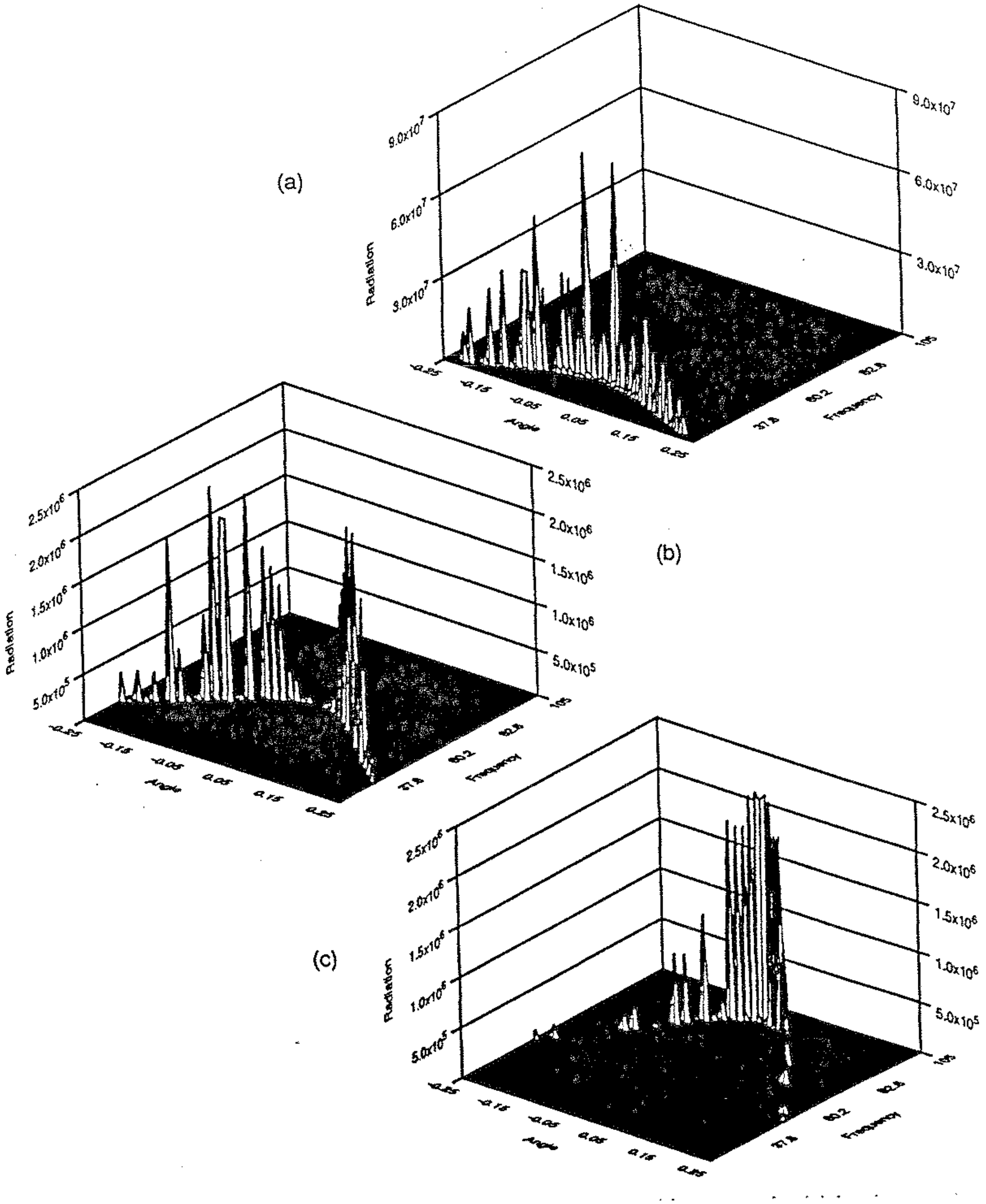

Figure 4.6: Radiation Emitted by the *ac* FEL versus frequency and angle for the (a) fundamental, (b) first harmonic, and (c) second harmonic. $\gamma_o = 4$, $a_w = 0.1$, ($-1/\gamma <$ angle $< 1/\gamma$), ($\gamma <$ frequency $< 6\gamma$), and $\phi = \pi/2$.

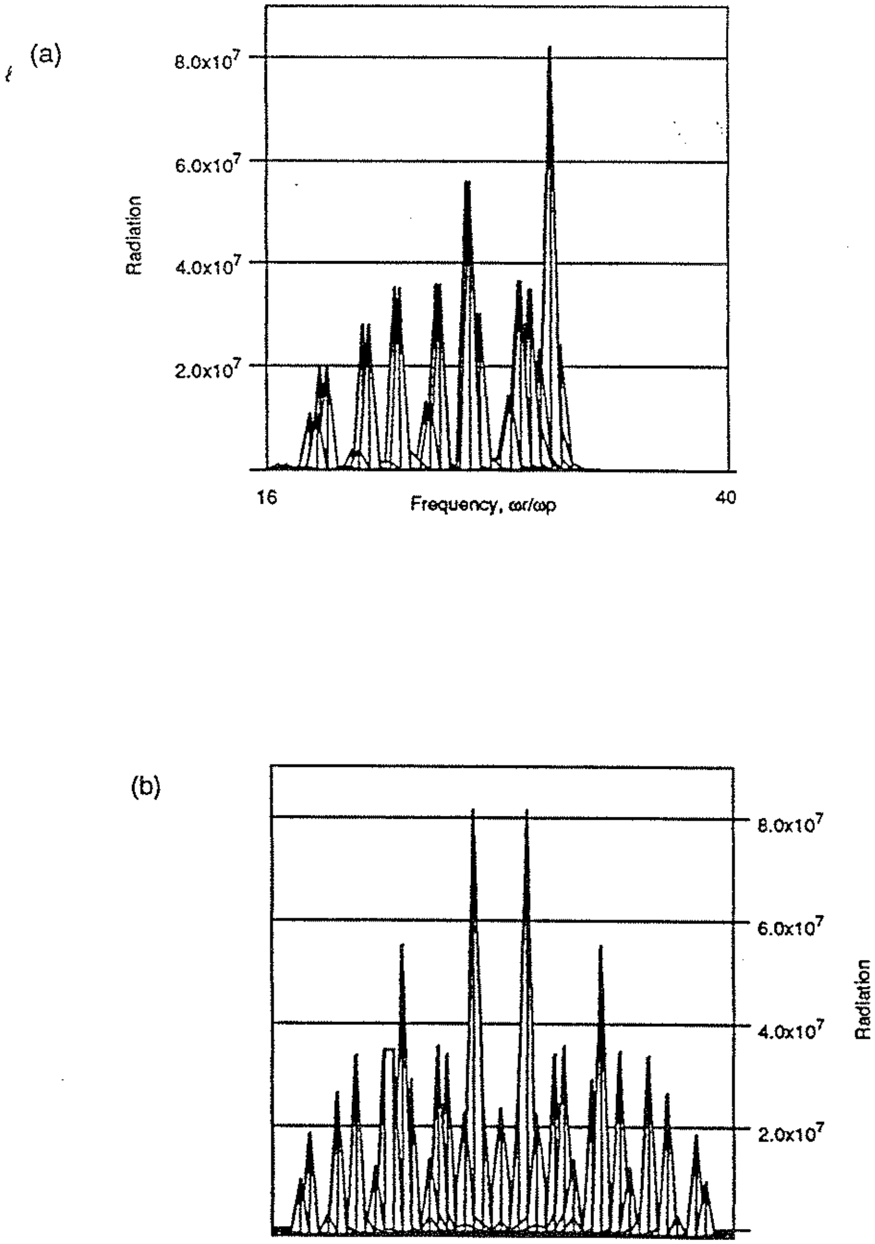

Figure 4.7: Radiation spectrum and angular distribution in the *ac* FEL for the fundamental frequency (same conditions as in figure 4.6).

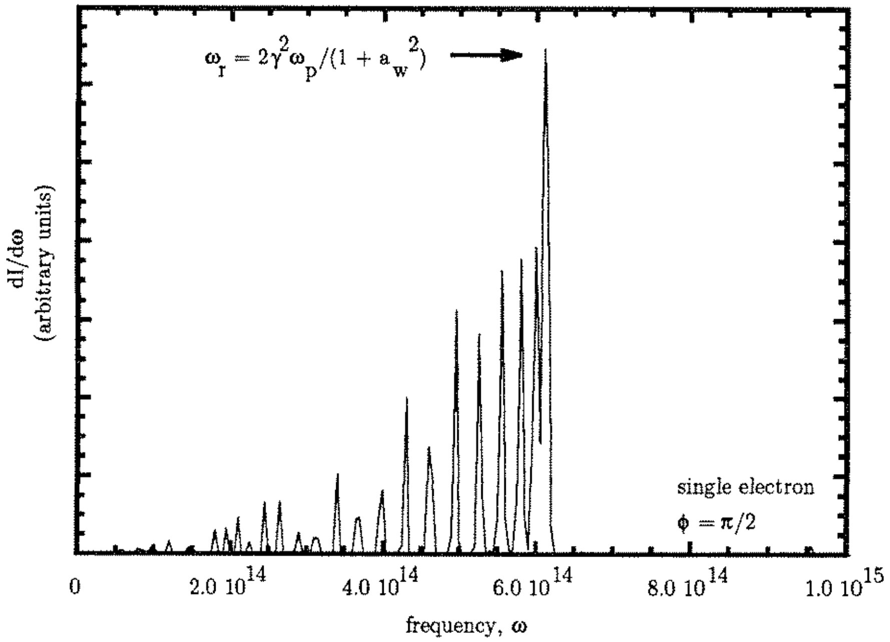

Figure 4.8: Spontaneous radiation spectrum obtained by simulation for the plasma wave undulator. $\gamma_o = 4$, $a_w = 1\%$, and $\phi = \pi/2$.

agreement with the beam spreading results discussed in Chapter 3.

The narrow spikes in the frequency spectrum found analytically and by simulation can be explained in analogy to a linear array of attennas phased so that the radiation peaks along the array axis, also called the end-fire array [57]. The electrons along the undulator radiate like antennas in line and their radiation adds in phase along the direction of propagation. Since the length of the undulator is long compared with the radiated wavelength, the summed radiation changes rapid as the angle of observation is changed from the forward direction. The angular width of the peaks can be estimated by setting equal to zero the argument of the sine term in the numerator of the line shape term in equation 4.13 for the radiation from the plasma undulator.

The peak of the frequency spectrum ($\theta = 0$ value of the fundamental) changes in accordance with the resonance relation,

$$\omega_r = 2\gamma^2\omega_p/(1 + a_w^2) \tag{4.33}$$

as γ and a_w are varied. The peaks of the frequency spectra obtained from several simulations are plotted along with the theoretical resonance relation in figures 4.9(a) and 4.9(b) versus γ and a_w, respectively. In these figures the solid line gives the theoretical values. The measured frequency values are given by X's when the absolute peak of the spectrum was used and by O's when the frequency was measured at half way up the high frequency slope of the spectral peak. The deviation of the X's in figure 4.9(a) is due to the widening of the spectral peaks as γ increases.

4.5 Stimulated Radiation, Radiation Gain and Electron Bunching

Approximate equations for the radiation gain are obtained by summing the fields of an injected plane electromagnetic (EM) wave with the plasma wave field, solving the equation of motion by perturbation to obtain the velocity, relating the average energy change of the electron to its average change in velocity along the undulator, and relating the change in radiation energy to the electron energy change.

The radiation and plasma wave electric fields are oriented along the same direction so that the total fields are

$$E = \left(E_o \cos\left(k_p y - \omega_p t\right) + E_r \cos\left(k_r z - \omega_r t + \phi_r\right)\right)\hat{y} \tag{4.34}$$

$$B = E_r \cos\left(k_r z - \omega_r t + \phi_r\right)\hat{x} \tag{4.35}$$

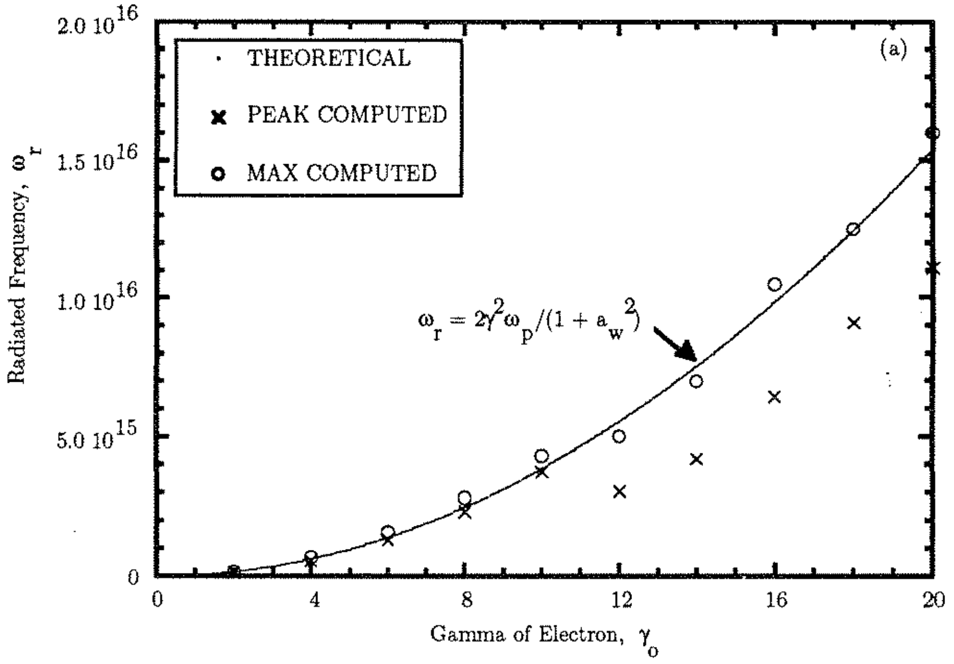

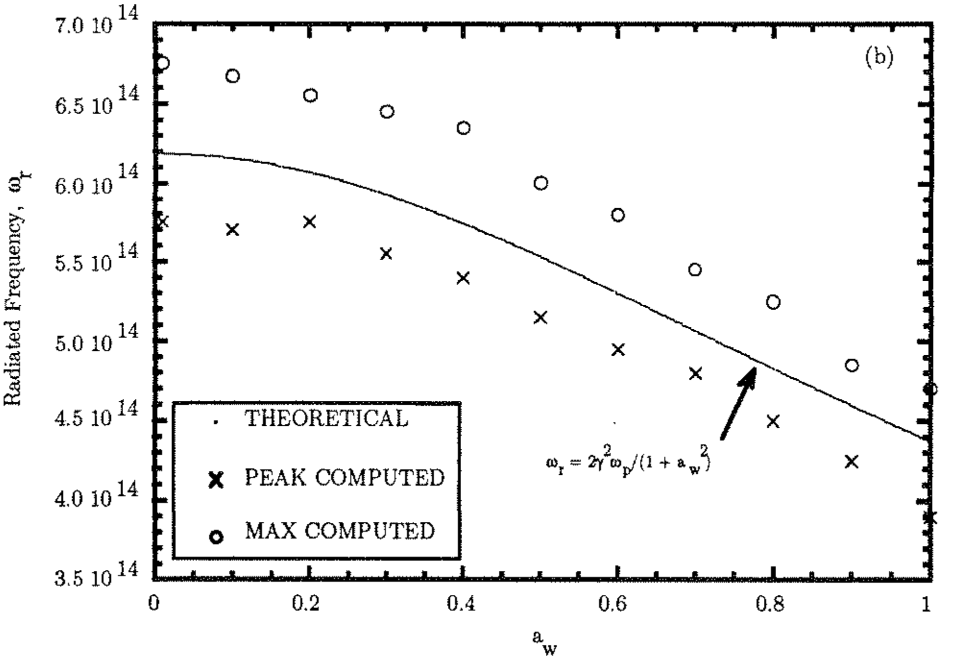

Figure 4.9: Comparison of theoretical resonance condition with simulation results for the plasma wave undulator for (a) variations in γ_o and (b) a_w.

where the EM radiation has field strength E_r, frequency ω_r, wave vector k_r and phase ϕ_r and B is the magnetic field of the EM radiation. In this low gain approximation E_r is approximately constant. The frequency of the injected EM radiation field is related to the frequency of the plasma wave undulator by the resonance condition, equation 4.33. An electron that is injected with energy γ is at resonance with the radiation and does not lose or gain energy. To get radiation gain, the electrons are injected with energy slightly greater than the resonance energy and the decrease of the average electron beam energy as it travels down the undulator results in a gain of radiation energy.

To solve the equation of motion it is separated into transverse and longitudinal components and solved for the perpendicular and parallel velocity components, $d\beta_\perp/dt$ and $d\beta_\parallel/dt$, which are function of the longitudinal position, z. The position, or phase, of the electron within a radiation wavelength is defined as

$$\zeta(t) = \zeta_o + \Delta\omega t + k_r dz(t), \tag{4.36}$$

where ζ_o is the initial phase, $\Delta\omega$ is the detuning factor and dz is the relative position of the electron in the wave. The detuning factor describes the amount that the electron's initial energy is different from the resonant energy and is

$$\Delta\omega = \beta_o\omega_p - \omega_r(1-\beta_o). \tag{4.37}$$

Using

$$\frac{d\beta_\parallel}{dt} = \frac{1}{\omega_r}\frac{d^2\zeta(t)}{dt^2} \tag{4.38}$$

a pendulum equation is obtained which describes the motion of the electron relative to the wave

$$\frac{d^2\zeta(t)}{dt^2} = \Omega_o^2 J_o(\alpha)\ \cos\alpha\ \cos\zeta(t) + a_w^2\omega_p^2 \sin(2\alpha - 2\omega_p t) \tag{4.39}$$

where

$$\alpha = \frac{k_p c\, a_w}{\omega_p \gamma_o} \tag{4.40}$$

and

$$\Omega_o^2 = \frac{2e^2 E_o E_r}{\gamma_o^2 m_o^2 c^2}. \tag{4.41}$$

This equation can be solved by perturbation to obtain the velocity, using

$$\varepsilon = \Omega_o^2/\Delta\omega^2 \tag{4.42}$$

as the small expansion parameter. From the change in velocity over the length of the undulator we obtain the change in electron energy. The average final electron energy, $\langle\gamma(t)\rangle$, is found by averaging over the initial phase, ζ_o. The negative of the average change in electron energy gives the change in radiation energy, which is

$$\frac{\gamma_o - \langle\gamma(t)\rangle}{\gamma_o} = \frac{\gamma_o^2\Omega_o^4}{\omega_r\Delta\omega^3} J_o^2(\alpha)\cos^2\alpha\left(1 - \cos\Delta\omega t - \frac{\Delta\omega t}{2}\sin\Delta\omega t\right) + \frac{a_w^2}{2} J_o(\alpha)\cos(2\alpha - 2\omega_p t). \tag{4.43}$$

The gain, $G(t)$, is obtained by multiplying the change in radiation energy by the number of electrons, $\rho_e V$, and dividing by the EM wave energy, $2E_r^2\rho_e V/8\pi$. Where ρ_e is the electron density and V is the volume that contains the electron beam and

EM radiation[51]. The resulting gain for the plasma wave undulator is

$$G(\tau) = \frac{8\pi e^4 E_o^2 \rho_e c}{\omega_p \gamma_o m_o c} \left(\frac{N_w \lambda_p}{\beta_o \gamma_o m_o c^2} \right)^3 \frac{1}{\Delta\varpi^3} \left[J_o^2(\alpha) \cos^2\alpha \left(1 - \cos \Delta\varpi\tau - \frac{\Delta\varpi\tau}{2} \sin \Delta\varpi\tau \right) \right]$$

$$\left. \frac{\Delta\varpi^3 \gamma^4 \left(\frac{E_o}{E_r} \right)^2}{4 a_w^2 \varpi_p^3} J_o(\alpha) \cos\left(2\alpha - 2\varpi_p \tau\right) \right] \tag{4.44}$$

where we have used the following dimensionless variables in the time varying terms

$$\tau = t\frac{\beta_o c}{N_w \lambda_p}, \quad \Delta\varpi = \Delta\omega \frac{N_w \lambda_p}{\beta_o c} \quad \text{and} \quad \varpi_p = \omega_p \frac{N_w \lambda_p}{\beta_o c}. \tag{4.45}$$

We note that $k_p c \approx \omega_p$ for the relativistic plasma wave and in general a_w is small and γ is large. Then the arguments of the cosine and Bessel function terms are small, thus these terms are approximately equal to one.

The pendulum and gain equations for the *ac* FEL undulator are obtained from equations 4.39, 4.43, and 4.44 by setting $k_p = 0$. The pendulum and gain equations for the linearly polarized magnetic undulator of strength B_o are obtained by setting $B_o = E_o$, and $a_w = k_p = 0$. The gain equations for the plasma wave and *ac* FEL undulator have terms which depend on $\varpi_p t$ and are due to the electrostatic field. The electrostatic field term also depends on the square of the ratio of the electrostatic to electromagnetic field magnitudes, and as the electromagnetic field becomes larger the electrostatic term becomes less significant.

In figure 4.10(a) we plot the gain, equation 4.44, in units of

$$\frac{8\pi e^4 E_o^2 \rho_e c / \omega_p}{\left(N_w \lambda_p / \beta_o \gamma_o m_o c^2\right)^3} \tag{4.46}$$

versus τ for several values of dimensionless detuning ($\Delta\varpi$ from 1 to 5) for the plasma wave undulator. At $\tau = 0$ the electron enters the undulator, and exits it at $\tau = 1$. For positive detuning values close to resonance ($\Delta\varpi$ small) there is positive gain which increases as the electron travels down the undulator, as shown in the figure. As the detuning increases, the gain reaches a maximum and begins to drop near the end of the undulator. For detuning values far from resonance (i.e. $\Delta\varpi > 10$) the gain will oscillate rapidly between positive and negative values as the electron travels along the undulator. The case shown in figure 4.10(a) is for an electron of $\gamma_o = 4$ in an undulator of $a_w = 0.1$, and undulator-to-wave field ratio E_o/E_r of 0.1. The gain plots for an *ac* FEL undulator and a linearly polarized magnetic undulator also resemble figure 4.10(a). However for smaller values of a_w or larger field ratios, the electrostatic term in the gain equation becomes significant and the gain curves become as shown in figure 4.10(b) for the plasma wave and *ac* FEL undulators. There is a rapid oscillation superimposed upon the gain curves which is due to the electrostatic field term in the gain equation. By adjusting the terms multiplying the electrostatic term of the gain equation, this oscillation can be eliminated or increased. The physical reason we give for this oscillation is as follows. As the electron oscillates, a component of its velocity is alternately parallel and antiparallel to the electric field. The electric field can change the energy of the electron by $\mathcal{E} = e\bar{v} \cdot \bar{E}$. In the magnetic undulator, the magnetic field cannot change the energy of the electrons and therefore the gain curves are smooth.

In figure 4.11 is plotted the gain and absorption versus detuning for four values of time, which represent plasma wave undulators that are shorter or longer than $\tau = 1$. Positive gain occurs for small positive values of detuning, and negative gain (or absorption) occurs for small negative values of detuning. For larger values of detuning (either positive or negative) the gain is small and oscillates about zero. The case shown in figure 4.11(a) is for an electron of $\gamma_o = 4$ in an undulator of $a_w = 0.1$, and undulator-to-wave field ratio of 0.1. The gain plots for an *ac* FEL

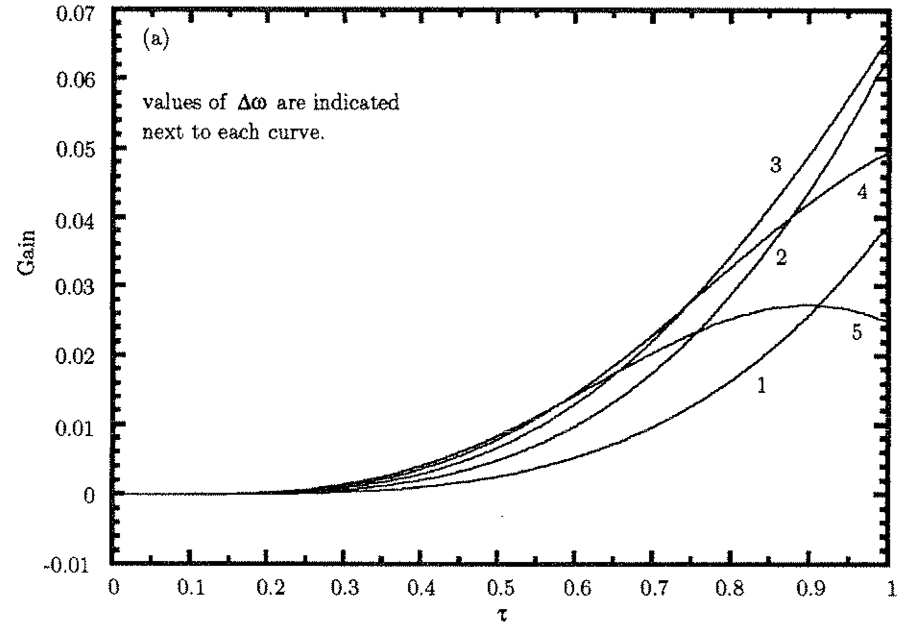

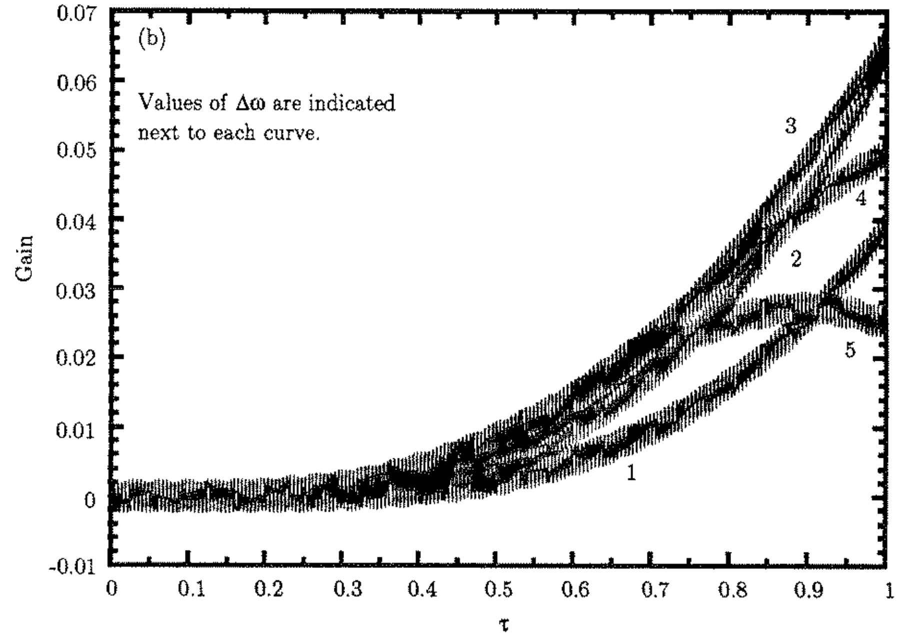

Figure 4.10: Normalized stimulated radiation gain versus normalized time in the plasma wave undulator for four values of detuning, $\Delta\omega$, for (a) E_o/E_r small and a_w large and (b) E_o/E_r large, a_w small and showing rapid gain oscillations.

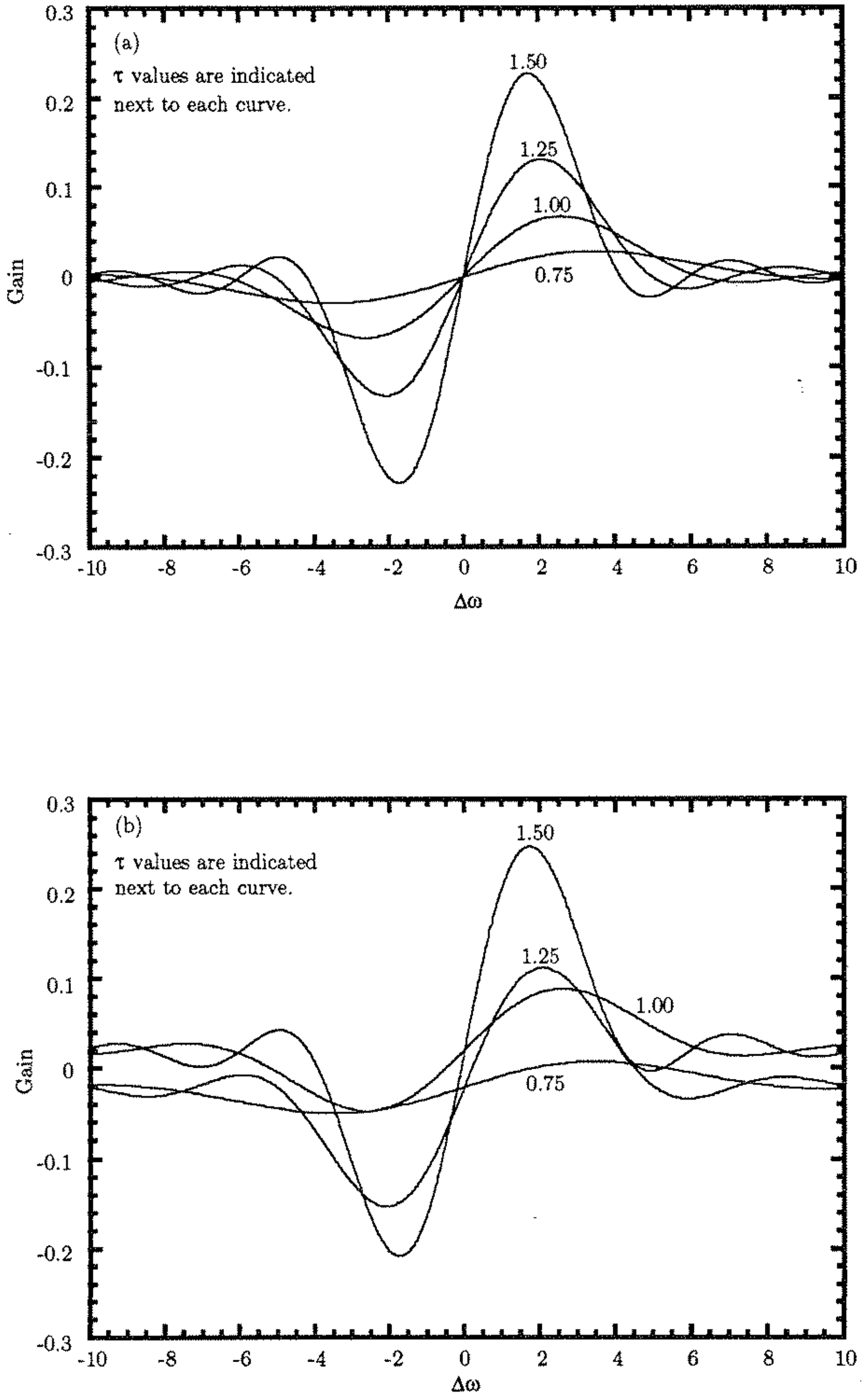

Figure 4.11: Radiation gain versus detuning in the plasma wave undulator for four values of normalized time, τ, for (a) E_o/E_r small and a_w large and (b) E_o/E_r large and a_w small, showing gain curves offset above and below the zero gain level.

undulator and linearly polarized magnetic undulator also resemble figure 4.11(a). The parameters of the plasma wave undulator can be chosen so that the electrostatic term becomes significant, and this is shown in figure 4.11(b) for $a_w = 0.01$, field ratio $= 3.0$ and $\gamma_o = 4$. Figure 4.11(b) shows that two of the curves oscillate about a mean value greater than zero and two oscillate about a value less than zero. If the field ratio were increased more, the separation between the two sets of curves would also increase. The parameters for figure 4.11(b) approximately correspond to those for figure 4.10(b) which has high frequency oscillations on the gain curves.

In the simulations a resonant EM wave was injected into the plasma wave co-parallel with a finite micropulse containing several thousand electrons having the same energy. Figure 4.12(a) shows the spatial distribution of the electrons after emerging from the plasma wave undulator, for the case when no EM wave is present. The electron bunch is moving upward and the plasma wave is moving to the left in the figure. In figure 4.12(b) the EM wave was has been added resulting in electron bunching. The separation between the large bunches in figure 4.12(b) is equal to the radiation wavelength, λ_r. There are closer spaced bunches within the larger electron bunches with separation approximately equal to the higher harmonic wavelengths.

In the simulation, a smaller monoenergetic group of fifty test electrons was injected along with an EM wave into the plasma wave undulator and allowed to drift to the end of the undulator. The final energy of the electrons was recorded and then averaged over the group of 50. In order to simulate injection at different detuning values each simulation run started with a different electron energy. In successive simulation runs, the initial electron energy was swept in small increments over the range from $\gamma_o = 3.9$ to 4.1. The EM wave frequency was resonant with the $\gamma_o = 4$ electron in each simulation run. The negative of the average energy change of the emerging electrons was plotted versus the initial energies in figure 4.13. This is the

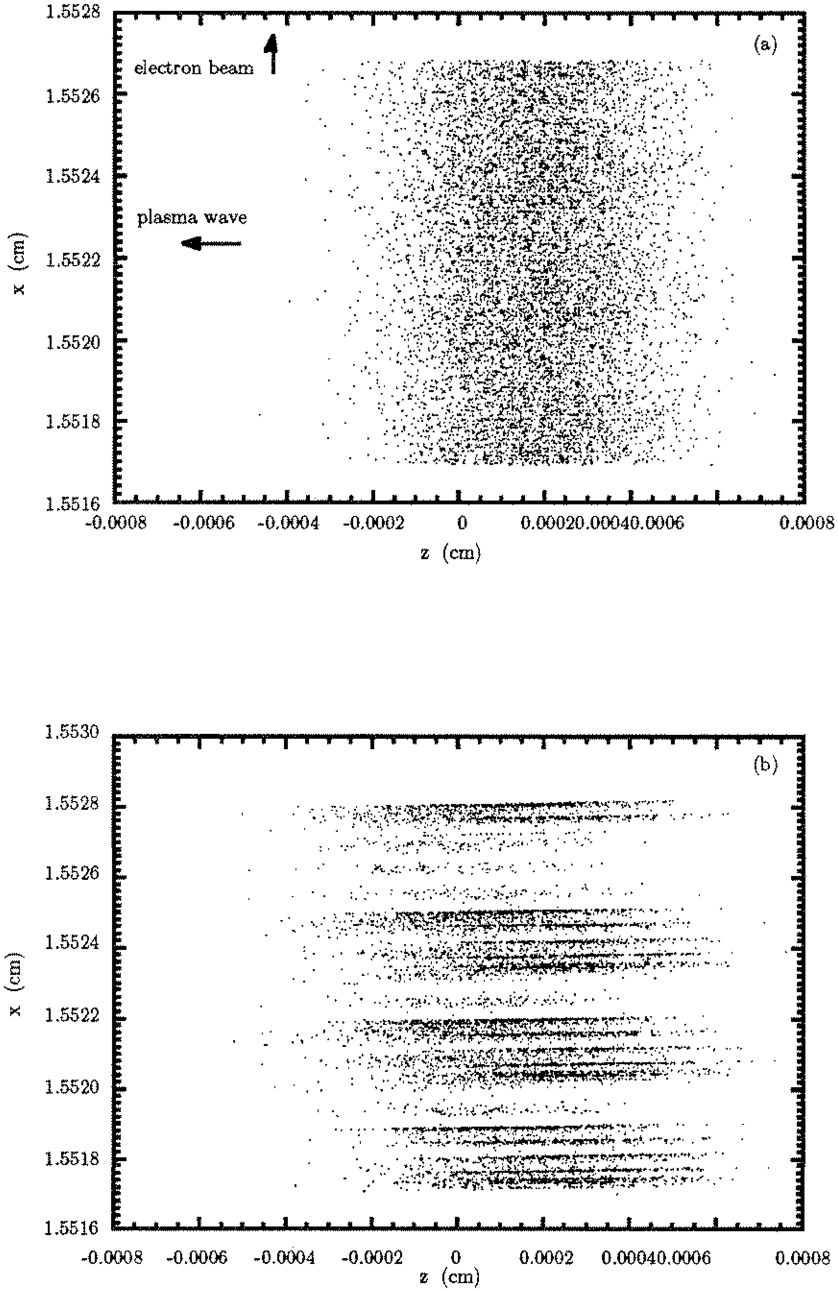

Figure 4.12: Distribution of electrons emerging from the plasma wave undulator for the cases of copropagating electromagnetic wave (a) not present and (b) present, showing bunching at the fundamental and harmonic wavelengths.

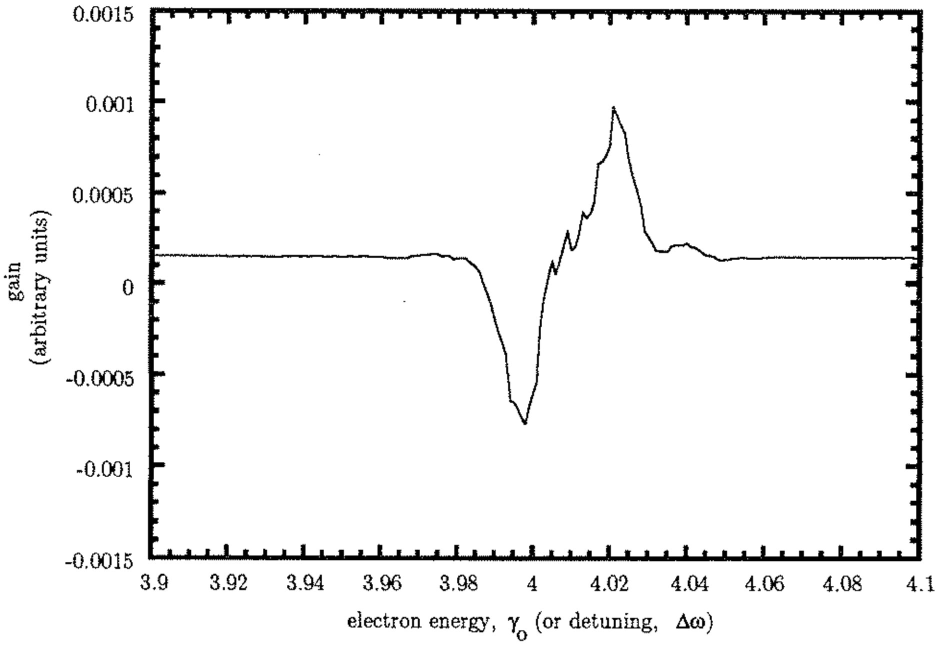

Figure 4.13: Radiation gain and absorption obtained by simulation versus electron injection energy (γ_o), or detuning ($\Delta\omega$). This radiation curve results from combining the radiation of 50 individual electrons.

gain/absorption curve obtained by simulation that was approximated by equation 4.44 and figure 4.11. Note that the baseline of the curve is shifted above the zero gain level, and that the curve is not symmetric about the resonant energy, $\gamma_o = 4$. If several thousand electrons had been used in the simulation (very expensive), the curve would probably have been much smoother. However, again we see that the simulation is in qualitative agreement with the results of the approximate analytic theory.

4.6 Summary

The relativistic plasma wave undulator has the potential to be a compact and less expensive source of short wavelength radiation down to the x-ray regime because it can be used with modest energy relativistic electron beams. Approximate expressions for the electron trajectories, spontaneous radiation and stimulated radiation gain have been obtained for the plasma wave undulator as well as the *ac* FEL. The electron trajectory has a very small transverse drift in the plasma wave undulator which causes the angular distribution of the spontaneous radiation to be directed at a small angle away from the undulator centerline. The *ac* FEL does not have this drift. The 3-D simulation results confirm the approximate analytical trajectory, spontaneous radiation and stimulated radiation gain calculations. The simulations also show that radiation gain occurs when an EM wave copropagates with the electron beam, however a rapid modulation of the gain can also occur. Electron bunching occurs at the radiation wavelength and at harmonics when the EM wave is copropagating with the beam. The stimulated radiation gain/absorption curves resemble those of magnetic undulators, except that a shift in the gain curves above or below zero gain can occur.

Now that a correlation has been established between the numerical code and the analytical calculation, we can venture to apply the code to more complex or arbitrary field configurations. For example, laser scattering from plasma waves or grating could be studied in detail. Another challenge would be to do the quantum radiation calculation and simulation.

Chapter 5

Studies of Electron Beam Matching and Spot Size Compression in a Ramped-Density Plasma Lens

5.1 Introduction

Plasma lenses have been proposed [58] and studied recently as a way to reduce e^+e^- beam spot sizes in future TeV linear colliders (TLC). Small spot sizes increase the luminocity, $\mathcal{L}$, at the collision point, and spot dimensions on the order of 1 nm × 190 nm and smaller will be desired in the future [59] [60] [61]. The luminocity is given by [61]

$$\mathcal{L} = \frac{N^2 b f H_D}{4\pi\sigma_x\sigma_y} \approx \mathcal{O}\left(10^{32}\ \mathrm{cm}^{-2}\ \mathrm{sec}^{-1}\right) \tag{5.1}$$

where

$N =$ number of particle per bunch

$b =$ number of bunches per linac pulse

$f =$ linac pulse repetition rate

$H_D =$ luminocity enhancement factor due to disruption

σ_x = bunch width in x direction

σ_y = bunch width in y direction .

Disruption is the additional pinching of one beam by the space charge of the other beam with which it collides. In this study we examine in detail one way that has been proposed for decreasing σ_x and σ_y.

Strong focusing fields will be required to obtain small spot sizes. Using thin lenses of any kind, there is a fundamental limit (the Oide limit [62]) on the final spot size due to the energy spread resulting from the synchrotron radiation emitted during strong focusing. The adiabatic plasma lens has been proposed [63] as an alternative to the thin lens since it would not be as severely restricted by the Oide limit. In the adiabatic plasma lens beam electrons create an ion channel [64][65] in the plasma which has a slowly increasing density. The ion space-charge field provides an increasing focusing force that continuously, and adiabatically, squeezes the beam to smaller spot sizes. Because there is a continuous focus rather than a single focal point, chromatic aberrations are reduced. In studying the adiabatic plasma lens, we have found that the increasing density ramp need not be adiabatic in order to reduce chromatic aberrations, provided that the beam and lens are matched.

Plasma lenses, sometimes called "space charge lenses", have been used to focus ion beams at least as early as 1947 (Garbor Lenses [66]) and had been suggested at least as early as 1932 [67]. One kind of plasma lens uses the magnetic field of an externally generated current in a z-pinch plasma to focus the particles, as is already in use in the CERN Antiproton Collector (ACOL) [68] [69] [70] [71] [72]. Another kind of plasma lens focuses by using the large transverse fields of relativistic plasma waves as found in plasma wakefield and beatwave schemes [71] [73] [74] [75] [76] [77] [78] [79]. Focusing of low energy electron beam ($<$ 20 MeV) has been experimentally demonstrated in the wakefield plasma lens [80] [83]. Two regimes of plasma lens operation have been studied: the overdense region in which the plasma density is greater than the beam density and the underdense region in which the plasma density is less than the beam density [77] [82]. The underdense plasma lens is favored over the overdense plasma lens because the latter has problems associated with nonlinear electron focusing resulting in aberrations and also large background collision event rates in the high density plasma. Unfortunately, positron beams experience nonlinear focusing in the underdense plasma lens, while the electrons have linear focusing, which makes collisions asymmetric. Recent investigations have shifted from wakefield type plasma lens schemes to schemes based on using a quiescent plasma column through which the beams are passed and focused [77] [85]. Low energy electron beam focusing has also been experimentally demonstrated in quiescent plasma lenses [86]. Recent refinements of the quiescent plasma lens scheme are the adiabatic focuser [63] [87] [88] and the tapered plasma funnel [89] which both rely on ramping the density of the quiescent plasma. The probem of experimentally producing these ramped-density plasmas has yet to be solved, however research is underway [88].

In this chapter we examine underdense ramped-density quiescent plasma lenses by using a 2-D numerical model that calculates the trajectories of electrons injected into a region of space that has an increasing focusing force. For the focusing force we use the ion space-charge created in the beam channel by the beam as it propagates into the plasma. However, the results of this study would pertain to any device that gives an increasing focusing force, not necessarily a plasma.

In the next section we describe the physical model of the underdense plasma lens, summarize the basic theory in terms of the Courant-Snyder (Twiss) parameters [90], and describe the 2-D numerical method. In the following sections the simulation results are presented on matching the beam to the lens and on the variation of beam spot size due to variations in the beam and lens Courant-Snyder parameters, and variation in beam energy.

5.2 Physical Model, Theory, and Numerical Method

5.2.1 Physical Model

In the adiabatic plasma lens concept a dense electron bunch passes through an underdense plasma such that

$$n_o < n_b, \tag{5.2}$$

where n_o is the lens plasma electron density and n_b is the electron beam density. The leading electrons in the bunch repel all of the background plasma electrons. This leaves a region containing relatively immobile and unshielded positively charged ions with density

$$n_{io} = n_o, \tag{5.3}$$

where n_{io} is the background ion density. The repulsive electrostatic forces of the electrons in the beam are canceled by the attractive $\bar{v} \times \bar{B}$ forces, where $\bar{v}$ is the electron velocity and $\bar{B}$ is the magnetic field due to the beam current. The unshielded ions of the background plasma produce a space-charge force, F_y. From Gauss' law this force is

$$\frac{F_y}{y} = -2\pi n_{io} e^2 = 300 \, \frac{MegaGauss}{cm} \times \frac{n_{io}(cm^{-3})}{10^{17}} \tag{5.4}$$

where y is the transverse displacement of the electron and e is the electron charge. This is the force that focuses the electrons. We note that in magnetic lenses, the focusing force is on the order of 10 kiloGauss/cm.

5.2.2 The Lens

The equation of motion of a particle in the lens is

$$\frac{d^2y(s)}{ds^2} + K(s)y(s) = 0 \tag{5.5}$$

where $K(s)$ is the focusing strength of the lens,

$$K(s) = \frac{F_y}{y}\frac{1}{\gamma m_o c^2} = \frac{2\pi n_{oi} e^2}{\gamma m_o c^2} = \frac{\omega_p^2}{2\gamma c} \tag{5.6}$$

and $n_{oi} = n_o$. This has a solution

$$y(s) = A\beta_l(s)^{1/2}\cos\left(\Psi(s) + \phi\right) \tag{5.7}$$

where A and ϕ are integration constants, $\Psi(s)$ is the phase advance, and $\beta_l(s)$ is the amplitude function, also called the Courant-Snyder beta-function.

Equation 5.7 is an exact solution provided that

$$K(s) = \frac{\frac{1}{4}\left(\frac{d\beta_l(s)}{ds}\right)^2 - \frac{1}{2}\beta_l(s)\frac{d^2\beta_l(s)}{ds^2} + \beta_l(s)^2\left(\frac{d\Psi(s)}{ds}\right)^2}{\beta_l(s)^2} \tag{5.8}$$

and

$$\Psi(s) = \int \frac{\text{constant}}{\beta_l(s)} ds \tag{5.9}$$

and we will let the constant equal one. In the originally proposed adiabatic lens scheme [58] $\beta_l(s)$ varies linearly with s as follows

$$\beta_l(s) = \beta_{lo} - 2\alpha_l(s)s \tag{5.10}$$

with

$$\beta_l(0) = \beta_{lo}, \tag{5.11}$$

where we define $\alpha_l(s)$, another Courant-Snyder parameter, as the amount of lens "adiabaticity" in the uniformly ramped plasma lens:

$$\alpha_l(s) = \alpha_l(0) = \alpha_{lo} = \text{constant}, \tag{5.12}$$

and

$$\alpha_l(s) = -\frac{1}{2}\frac{d\beta_l(s)}{ds} = -\frac{1}{2}\beta_l'(s). \tag{5.13}$$

By uniformly ramped, we mean that the beta-function varies (decreases) at a constant rate in the lens, or that $\alpha_l(s)$ is a constant throughout the lens. (The nonuniformly ramped adiabatic lens will be discussed later.) For the uniformly ramped adiabatic lens equation 5.8 becomes

$$K(s) = \frac{1+\alpha_{lo}^2}{\beta_l(s)^2} = \frac{1+\alpha_{lo}^2}{(\beta_{lo} - 2\alpha_{lo}s)^2}. \tag{5.14}$$

We can find the value of $\beta_l(s)$ at the entrance to the lens ($s = 0$) by combining equations 5.14, 5.5, and 5.4 to get

$$\beta_l(0) = \beta_{lo} = \sqrt{2\gamma\left(1+\alpha_{lo}^2\right)}\,\frac{c}{\omega_{po}} \tag{5.15}$$

where we have used the initial background plasma electron density at the entrance to the plasma lens given by

$$\omega_p(0)^2 = \omega_{po}^2 = \frac{4\pi n_{eo}e^2}{m_o}. \tag{5.16}$$

Using the above expressions we have the important relationships:

$$K(s) \propto \frac{1}{\beta_l^2(s)} \propto n(s) \propto \frac{1}{y^4(s)} \tag{5.17}$$

for the unimformly ramped plasma lens.

We note that equation 5.7 is the approximate WKB solution to the equation of motion, equation 5.5, for the condition

$$\frac{d\beta_l(s)}{ds} \ll \frac{1}{2}. \tag{5.18}$$

In that approximation we also get

$$\beta_l(s) = \frac{1}{\sqrt{K(s)}} \quad \text{and} \quad \Psi(s) = \int \frac{1}{\beta_l(s)} ds. \tag{5.19}$$

The inequality in equation 5.18 is the condition that the plasma density ramp be adiabatic.

5.2.3 The Beam

The coordinates of the beam as it propagates through the lens are related by the beam ellipse equation (an exact constant of the motion)

$$\frac{\left[y(s)^2 + (\alpha_b(s)y(s) + \beta_b(s)y'(s))^2\right]}{\beta_b(s)\epsilon} = 1 \tag{5.20}$$

where

$$y'(s) = \frac{dy(s)}{ds}, \tag{5.21}$$

the beam ellipse skewness factor is

$$\alpha_b(s) = -\frac{1}{2}\frac{d\beta_b(s)}{ds} = -\frac{1}{2}\beta_b'(s), \tag{5.22}$$

$\beta_b(s)$ is the beam betatron wavelength, and ϵ is the beam emittance. The beam betatron wavelength is related to the oscillation wavelength, λ_b, by

$$\beta_b(s) = \frac{\lambda_b}{2\pi} \tag{5.23}$$

Equation 5.20 also describes the boundary of the beam in phase space where ϵ is the area of the beam in phase space divided by π, and the normalized emittance is

$$\epsilon_n = \gamma\epsilon. \tag{5.24}$$

5.2.4 The Meaning of Matched and Unmatched Beam and Lens

In the original adiabatic plasma lens scheme [58] the beam and lens were unmatched, meaning that the waist of the beam coincided with the entrance to the lens, as illustrated in figure 5.1(b). In our analysis of the plasma lens, we fix the values of α_l and β_l for the lens and will compare the two cases in which the beam is matched and unmatched to the lens. The values of the electron beam's α_b and β_b at the entrance to the lens are varied conceptually by shifting the position of the beam along s axis. Figure 5.1(a) shows that for the matched beam and lens case there is a continuous transition of the slope of the beam envelope as it enters the

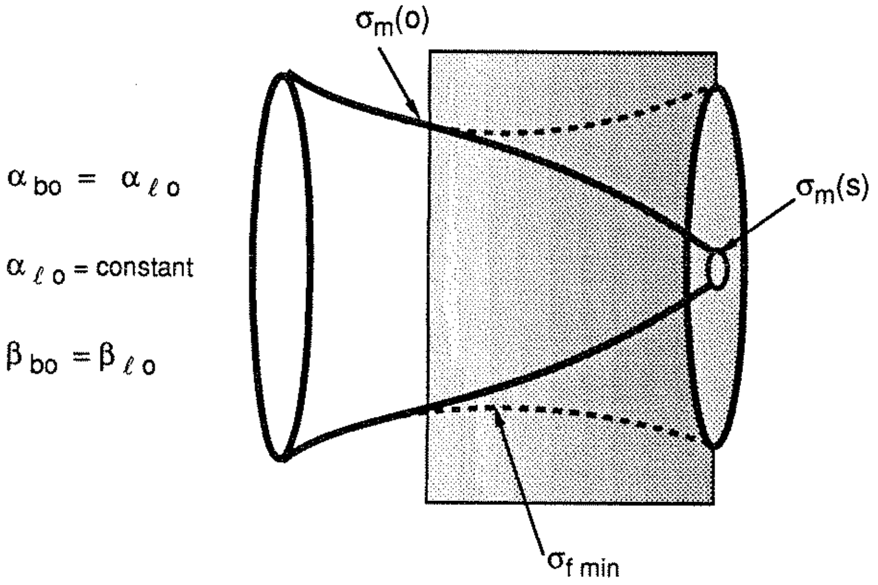

(a) Beam and Lens are Matched:

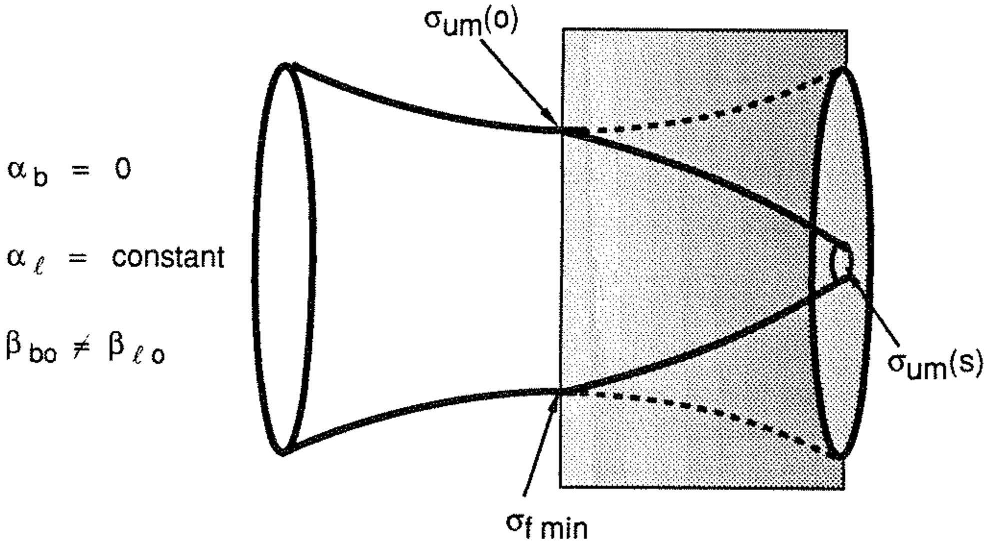

(b) Beam and Lens are Unmatched:

Figure 5.1: Geometry of beam and ramped density plasma lens showing the (a) matched and (b) unmatched schemes.

lens from free space. For the matched beam and lens case we have

$$\alpha_b(0) = \alpha_l(0), \tag{5.25}$$

$$\beta_b(0) = \beta_l(0), \tag{5.26}$$

and

$$\beta_b'(0) = -2\alpha_l(0). \tag{5.27}$$

For the unmatched beam and lens case we have

$$\alpha_b(0) \neq \alpha_l(0), \tag{5.28}$$

$$\beta_b(0) = \beta_l(0), \tag{5.29}$$

and

$$\beta_b'(0) = 0. \tag{5.30}$$

These definitions for the matched and unmatched cases will be extended in a later section to include the lens nonuniformity factor.

5.2.5 Electron Trajectories and Spot Size Compression

The amplitude of the electron transverse displacement, betatron wavelength and ion density at a position s in the lens are related to their initial quantities by

$$\frac{y(s)}{y(0)} = \left[\frac{\beta_l(s)}{\beta_{lo}}\right]^{1/2} \frac{\cos\Psi(s)}{\cos\Psi(0)} \leq \left[\frac{n_{io}}{n_i(s)}\right]^{1/4} \frac{1}{\cos\Psi(0)} \tag{5.31}$$

where we have used

$$\cos\Psi(s) \leq 1. \tag{5.32}$$

We refer to the ratio $y(s)/y(0)$ as the spot size compression or reduction, where $y(0)$ is the beam radius at the lens entrance and $y(s)$ is the beam radius at the minimum waist at the exit of the lens. To find $\cos\Psi(0)$ we differentiate equation 5.7, then for $y'(0) = 0$ we get,

$$\cos\Psi(0) = \frac{1}{\sqrt{1+\alpha_{lo}^2}} \,. \tag{5.33}$$

Thus for particles initially parallel and on the boundary of the beam envelope (unmatched case), equation 5.31 becomes

$$\frac{y(s)}{y(0)} \leq \left[\frac{n_{io}}{n_i(s)}\right]^{1/4} \sqrt{1+\alpha_{lo}^2} = \left[\frac{\beta_l(s)}{\beta_{lo}}\right]^{1/2} \sqrt{1+\alpha_{lo}^2} \,. \tag{5.34}$$

For $\cos\Psi(0) = 1$, we find that

$$y'(0) = -\frac{\alpha_{lo}}{\sqrt{\beta_{lo}}} \tag{5.35}$$

which gives the slope of the beam envelope at the entrance to the lens for the matched case (see figure 5.1(a)). Thus for particles initially on the boundary of the matched beam envelope at $s = 0$, equation 5.31 becomes

$$\frac{y(s)}{y(0)} \leq \left[\frac{n_{io}}{n_i(s)}\right]^{1/4} \,. \tag{5.36}$$

Note that equation 5.31 is exact, independent of whether the density is ramped adiabatically ($\beta' \ll 1/2$) or not. This suggests that the lens need not be adiabatic if the beam enters the plasma converging at the matching angle, θ_m. The matching angle is

$$\theta_m = \frac{d\sigma_y}{ds} = \frac{\sigma_y}{4n_{io}} \frac{dn_{io}}{ds} \tag{5.37}$$

which was obtained using equation 5.14, equation 5.13, the expression for the r.m.s.

beam radius

$$\sigma_y^2 = \epsilon\beta_{lo}, \tag{5.38}$$

and the definition of the plasma density scale length, L_s, at the lens entrance:

$$L_s^{-1} = \frac{1}{K}\frac{dK}{ds} = \frac{1}{n_{io}}\frac{dn_{io}}{ds}\,. \tag{5.39}$$

We note that equation 5.14 is a convenient choice for the form of the plasma density profile, where $K(s)$ is proportional to $n(s)$. In general, if the density profile $n(s)$ is specified, then equation 5.8 can be solved numerically for $\beta(s)$ and $\beta'(s)$. Then the initial to final spot size ratio for the particles on the boundary of the beam envelope for a matched beam and lens is, from equation 5.31,

$$\frac{y(s)}{y(0)} = \left[\frac{\beta_l(s)}{\beta_{lo}}\right]^{1/2}. \tag{5.40}$$

Generally $\beta(s)$ is not simply proportional to $n^{1/2}(s)$ and must be solved for numerically.

In figure 5.2 we show a theoretical envelope of the electron beam along with a representative single electron trajectory in an adiabatic lens. The theory curve is a plot of equation 5.34, and the trajectory is a plot of the numerical solution to the equation of motion, equation 5.5, for $K(s)$ given by equation 5.14. In figure 5.2 the focusing strength $K(s)$ is increased by a factor of 10^4; i.e. until the following condition is met

$$\frac{1}{(\beta_{lo} - 2\alpha_{lo}s)^2} \geq \frac{10000}{\beta_{lo}^2}\,. \tag{5.41}$$

Then the focusing strength is held constant so that we can display and measure the trajectories which then have constant betatron wavelengths. The left side of equation 5.41 will diverge at a particular value of s resulting in an infinitely small

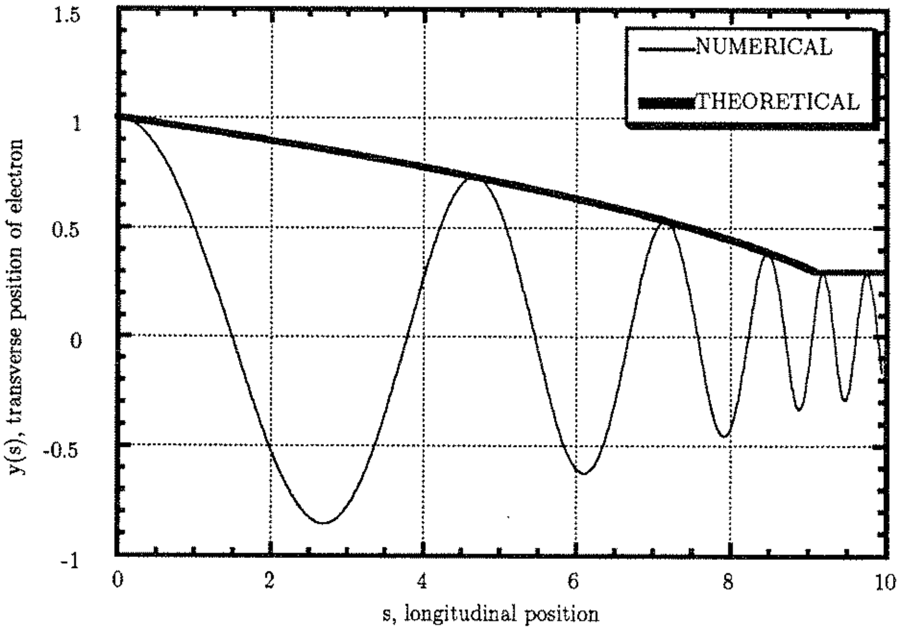

Figure 5.2: Electron trajectory and beam envelope in ramped density plasma lens.

minimum spot width. The condition 5.41 is used to limit the divergence, and by adjusting this limit we could adjust the absolute minimum width of the trajectory in figure 5.2. But in this study we are interested in understanding the variation of the spot size compression as a function of beam and lens parameters and not necessarily the absolute minimum spot width, and thus we tolerate the arbitrariness of the absolute spot size shown in these trajectory graphs. In an actual plasma lens the absolute minimum spot width would be determined by the ratio of the minimum and maximum densities in the lens, the width of the beam at the entrance to the lens and the Courant-Snyder parameters.

5.2.6 Numerical Method

In the simulations, the trajectories of several hundred electrons were calculated by numerically solving the equation of motion, equation 5.5, using a Runge-Kutte scheme. The initial transverse positions and velocities of the particles were described by the distribution

$$f(y, y') = exp\left[\frac{y^2 + (\alpha_b y + \beta_b y')^2}{\beta_b \epsilon}\right]. \qquad (5.42)$$

and were obtained using a bivariate normal random number generating subroutine.

The spot size compression was calculated in the simulations by taking the ratio of the r.m.s. widths of the beam's input trajectories to the final focused trajectories. The input trajectories were all calculated at $s = 0$ since all electrons were injected there. The final focused widths were calculated by first obaining the r.m.s. widths of each trajectory and then averaging over all of the trajectories.

5.3 Spot Size Compression vs Uniform Ramping

In this section we examine the beam spot size compression in the plasma lens as a function of the lens adiabaticity, α_l, for the cases of matched and unmatched beams. By varying α_l we change the rate at which the density and focusing force increase in the lens.

A beam of particles converging in free space is shown in figure 5.3, where we have plotted just a few particle trajectories. The figure shows that the beam has an initial r.m.s. free space width equal to $\sigma_f(s)$ at $s = 0$, converges to a minimum free space waist equal to $\sigma_{f_{min}}$ at $s \approx 6$, and then diverges. We assume that the beam has been focused by some magnet system upstream and the problem is to further reduce the width of this beam using a plasma lens. In this example the beam has $\alpha_b(0) = \sqrt{3}$, $E_o = 15$ GeV and $\epsilon_n = 1 \times 10^{-4}$ m-rad. These parameters were taken from Table I of reference [63] which gives design examples for an adiabaic lens placed at the SLAC End Station, SLC and TLC.

Figure 5.4 shows several trajectories from the same beam which are injected into a plasma lens having $\alpha_l(0) = \alpha_b(0) = \sqrt{3}$, which is the matched case. Again

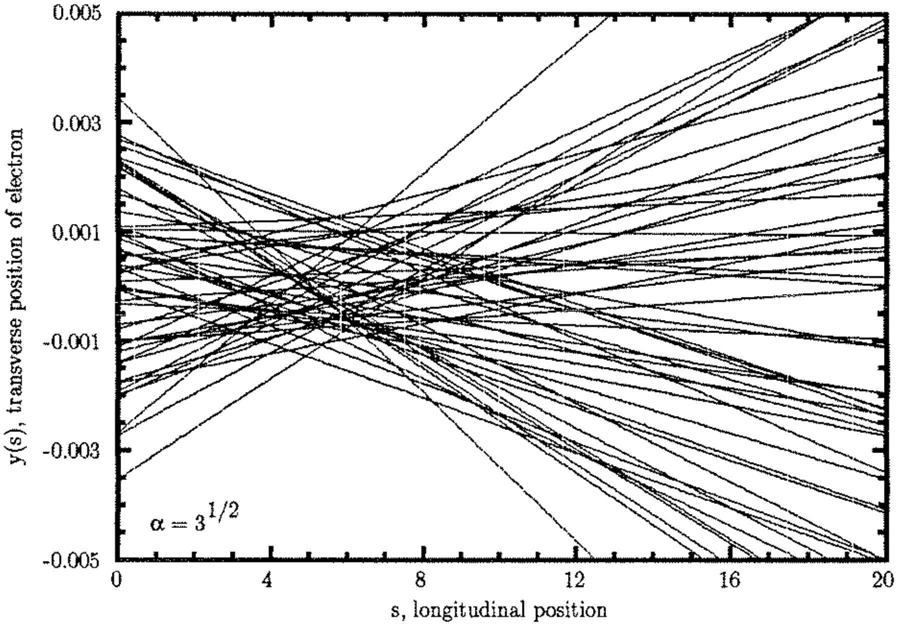

Figure 5.3: Electron trajectories in free space.

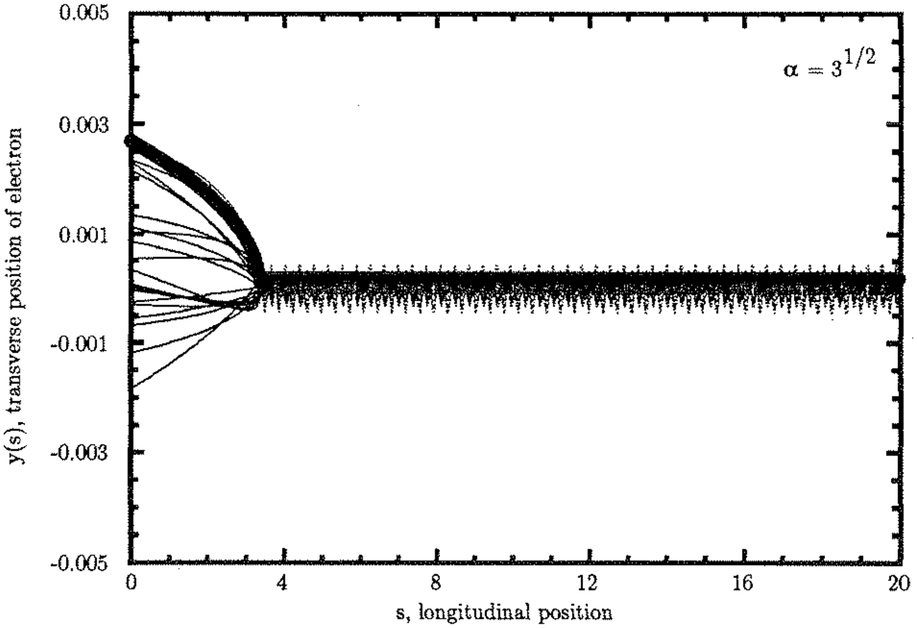

Figure 5.4: Electron trajectories in a matched ramped density plasma lens.

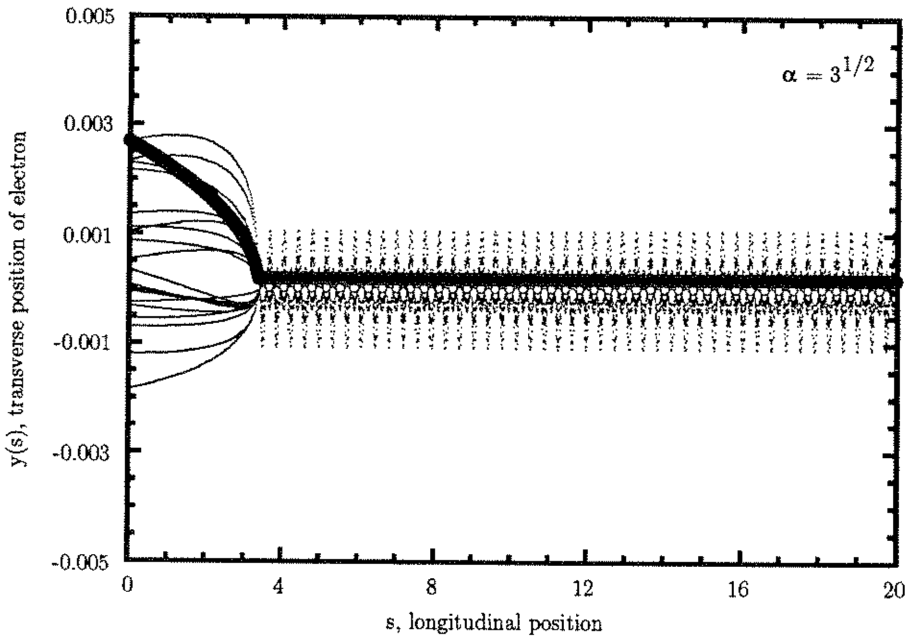

Figure 5.5: Electron trajectories in an unmatched ramped density plasma lens.

we assume that the beam has been prefocused and is converging when it enters the plasma lens at $s = 0$. The focused width of the beam at $s \approx 3$ is given by equation 5.36. The plasma lens clearly focuses the beam to a spot size smaller than the free space waist. The theoretical curve for the envelope is also plotted (thick line). As in figure 5.2, the focusing force is increased and then held constant in accordance with equation 5.41.

Figure 5.5 shows the beam injected into the plasma lens which has $\alpha_l(0) = \sqrt{3}$, but now the beam has $\alpha_b(0) = 0$, which is the unmatched case. We assume that the beam has been prefocused but not as strongly as in the matched case, so that here the beam is at a different free space waist, now located at $s = 0$, that is the same width as the converging beam in the matched beam case at $s = 0$. The theoretical curve is also shown. Clearly the beam's focused spot size is not as small as in the matched plasma lens case.

The variation of beam spot size compression, $\sigma_{max}/\sigma_{min}$ as a function of $\alpha_l(0)$

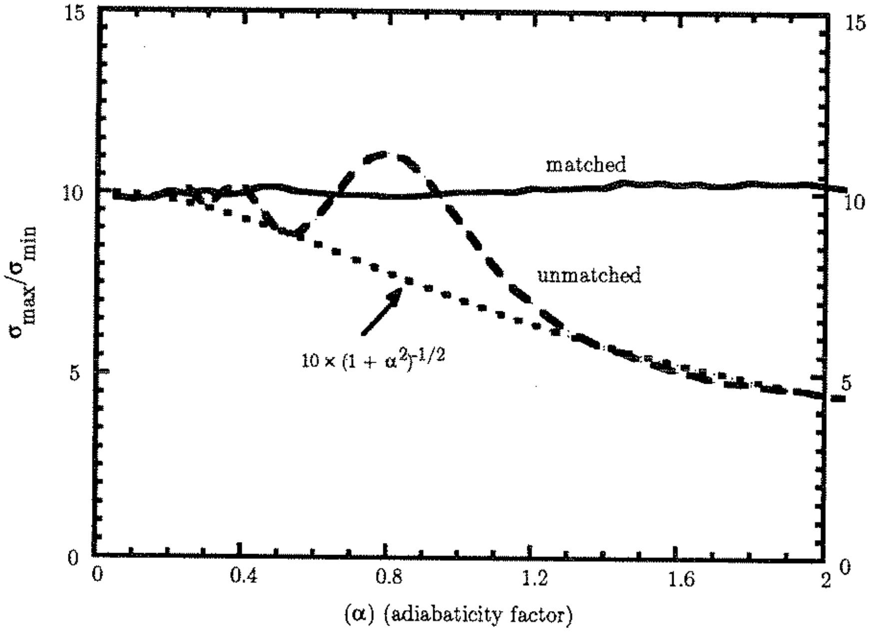

Figure 5.6: Spot size compression vs adiabiticity factor for matched and unmatched beam and lens.

and of matching is shown in figure 5.6. For small values of α_l, less than approximately 0.5, the reduction due to unmatching is negligible. But for larger values of α_l up to at least 2.0, the matched beam compression remains constant and the unmatched beam compression decreases. Note that for $\alpha_l > 1$ the adiabatic condition, equation 5.18, fails. Therefore we conclude that for matched beam and lens, it is not necessary to limit the plasma lens by the adiabatic condition.

In figure 5.6 we have also plotted the theoretical reduction factor for the unmatched case, which follows the numerical data for the unmatched case. There is an oscillation in the ummatched curve which we attribute to the phase advance term, $\cos\Psi(s)$, which appears in the solution to the equation of motion and in equation 5.31.

We now compare the minimum spot size for the matched and unmatched cases with the minimum free space waist. From beam optics theory [91] [92] the r.m.s.

free space beam spot size, $\sigma_f(s)$, at position s, is related to the minimum free space waist, $\sigma_{f_{min}}$ located at $s_{f_{min}}$ by

$$\sigma_f^2(s) = \sigma_{f_{min}}^2 \left(1 + \frac{(s - s_{f_{min}})^2}{\beta_{f_{min}}^2}\right) = \epsilon\beta_f(s) \tag{5.43}$$

where $s_{f_{min}}$ is the position of the minimum free space waist. The subscript "*f*" refers to "free space" and the subsubscript "*min*" always refers to the "minimum" width of the beam. The betatron wavelength is

$$\beta_f(s) = \beta_{f_{min}} \left(1 + \frac{(s - s_{f_{min}})^2}{\beta_{f_{min}}}\right). \tag{5.44}$$

Differentiating equation 5.44,

$$\beta'(s) = -2\alpha_b(s) = 2\frac{(s - s_{f_{min}})}{\beta_{f_{min}}}\,, \tag{5.45}$$

and substituting into equation 5.43 gives

$$\sigma_f^2(s) = \sigma_{f_{min}}^2 \left(1 + \alpha_b^2(s)\right). \tag{5.46}$$

For the matched beam and lens we rewrite equation 5.36 in the r.m.s. notation as

$$\sigma_{m_{min}}^2(s) = \sigma_m^2 \left[\frac{n_{io}}{n_i(s)}\right]^{1/2} \tag{5.47}$$

where $\sigma_{m_{min}}(s)$ is the minimum spot width at s in the matched plasma lens and σ_m is the spot width at the entrance to the lens at $s = 0$. The subscript "m" refers to "matched". Comparing our examples for the free space beam and matched beam and lens we see that

$$\sigma_m^2(s) = \sigma_f^2(s) \tag{5.48}$$

at $s = 0$. We then find that the relationship between the free space waist and the minimum spot width in the matched beam and plasma lens example is

$$\sigma^2_{m_{min}}(s) = \sigma^2_{f_{min}} \left(1 + \alpha^2_{bo}\right) \left[\frac{n_{io}}{n_i(s)}\right]^{1/2} . \tag{5.49}$$

where the minimum width of the matched beam occurs at s.

For the unmatched beam and lens we rewrite equation 5.34 as

$$\sigma^2_{um_{min}}(s) = \sigma^2_{um} \left[\frac{n_{io}}{n_i(s)}\right]^{1/2} \left(1 + \alpha^2_{lo}\right) . \tag{5.50}$$

The subscript "*um*" refers to "unmatched". Following the procedure above we find that the relationship between the free space waist and the minimum spot width in the unmatched beam and lens example is

$$\sigma^2_{um_{min}}(s) = \sigma^2_{f_{min}} \left(1 + \alpha^2_{bo}\right) \left[\frac{n_{io}}{n_i(s)}\right]^{1/2} \left(1 + \alpha^2_{lo}\right) . \tag{5.51}$$

If we place the entrance to the plasma lens at the free space waist shown in figure 5.3 then this would be an unmatched cases, and the minimum waist obtained in the lens in terms of the free space waist would be

$$\sigma^2_{umafw_{min}}(s) = \sigma^2_{f_{min}} \left[\frac{n_{io}}{n_i(s)}\right]^{1/2} \left(1 + \alpha^2_{lo}\right) \tag{5.52}$$

where the subscript "umafw" refers to "unmatched at free space waist".

According to our previous analysis the adiabatic condition should be applied to the plasma lens in this special case.

In comparing the three configurations, equations 5.49, 5.51, and 5.52, we find that the minimum spot size depends on the values of α_{lo} and α_b.

5.4 Spot Size Compression vs Nonuniform Ramping

Thus far we have assumed that the plasma density ramps everywhere with the same degree of adiabaticity (i.e, $\alpha_l(s)$ = constant, equation 5.12). Next we consider deviations from this assumption. We include the effect of nonuniform ramping in $\alpha_l(s)$ by setting

$$\alpha_l(s) = \alpha_{lo}\,(1 - \delta_l s) \tag{5.53}$$

so that

$$\beta_l(s) = \beta_{lo} - 2\alpha_l(s)s = \beta_{lo} - 2\alpha_{lo}\left(s - \delta_l s^2\right) \tag{5.54}$$

where δ_l is the nonuniformity factor for the lens. Thus $\delta_l > 0$ ($\delta_l < 0$) corresponds to a lens that is becoming more (less) adiabatic with distance into the lens. For this case we find, using the same steps which lead to equation 5.8 for the uniform case, that

$$K(s) = \frac{1 + \alpha_{lo}^2 - 2\alpha_{lo}\beta_{lo}\delta_l}{(\beta_{lo} - 2\alpha_{lo}s + 2\alpha_{lo}\delta_l s^2)^2} = \frac{\text{constant}}{\beta_l(s)}\ , \tag{5.55}$$

and also following the steps which lead to equation 5.15 we get that

$$\beta_{lo} = \left[-\frac{\alpha_{lo}\gamma c}{\omega_{po}}\delta_l + \sqrt{\left(\frac{\alpha_{lo}\gamma c}{\omega_{po}}\right)^2 \delta_l^2 + 2\gamma\left(1 + \alpha_{lo}^2\ \right)}\,\right]\frac{c}{\omega_{po}}\ . \tag{5.56}$$

Notice that because the numerator in equation 5.55 is independent of s, we can use equation 5.17 to show that for this nonuniform case the unmatched compression is

$$\frac{y(s)}{y(0)} = \left[\frac{\beta_l(s)}{\beta_{lo}}\right]^{1/2}\frac{\cos\Psi(s)}{\cos\Psi(0)} \le \left[\frac{n_{io}}{n_i(s)}\right]^{1/4}\frac{1}{\cos\Psi(0)} \tag{5.57}$$

just as in equation 5.31 for the uniform case. For the matched nonuniform case we

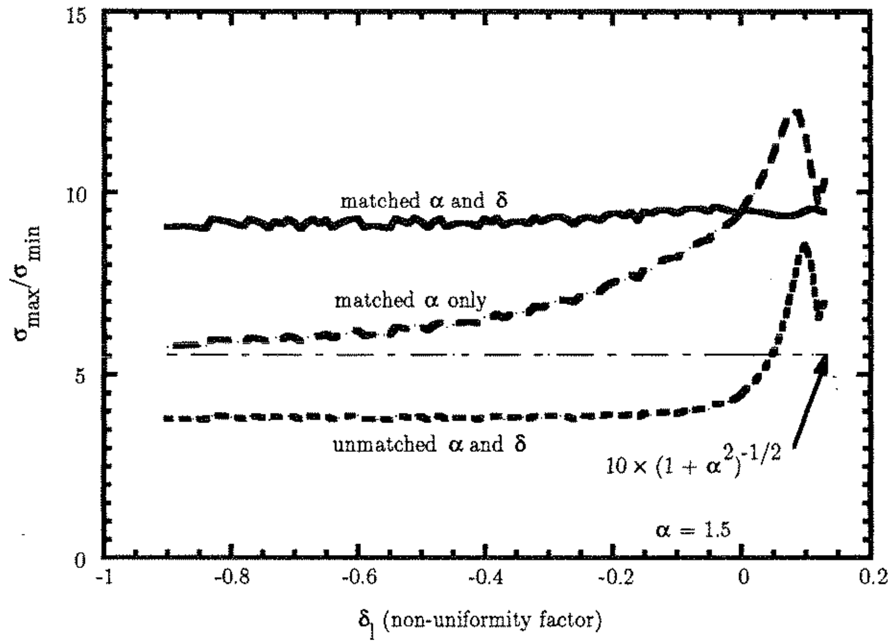

Figure 5.7: Spot size compression vs nonuniformity for three matching conditions.

get the compression

$$\frac{y(s)}{y(0)} \leq \left[\frac{n_{io}}{n_i(s)}\right]^{1/4} \sqrt{1+\alpha_{lo}^2} = \left[\frac{\beta_l(s)}{\beta_{lo}}\right]^{1/2} \sqrt{1+\alpha_{lo}^2}. \tag{5.58}$$

and also

$$y'(0) = -\frac{\alpha_{lo}}{\sqrt{\beta_{lo}}} \tag{5.59}$$

just as in equation 5.34 for the uniform case. The difference here is that we have new expressions for $K(s)$ and $\beta_l(s)$ and the matching conditions. The expressions relating the minimum r.m.s. free space waist to the minimum spot widths in the matched and unmatched uniform lens, equations 5.49, 5.51, and 5.52, are exactly the same for this nonuniform lens case.

Spot size compression versus the nonuniformity factor, δ_l, is plotted in figure 5.7 for $\alpha_{lo} = 1.5$ and for the matched and unmatched cases. The upper curve in figure 5.7 shows that spot size compression is constant for matched α and δ_l. By matched α and δ_l we mean that

$$\alpha_{bo} = \alpha_{lo} \tag{5.60}$$

and

$$\beta_{bo} = \beta_{lo} = \left[-\frac{\alpha_{lo}\gamma c}{\omega_{po}}\delta_l + \sqrt{\left(\frac{\alpha_{lo}\gamma c}{\omega_p}\right)^2 \delta_l^2 + 2\gamma\left(1+\alpha_{lo}^2\ \right)} \right] \frac{c}{\omega_{po}}. \tag{5.61}$$

This means that we can change the focusing rapidly ($\delta_l < 0$) and the spot size will be unaffected as along as we can adjust the α_{bo} and β_{bo} of the beam to match.

The next lower curve in figure 5.7 shows the case when α is matched but δ_l is not, which means that α_{bo} is given by equation 5.60, β_{lo} is given by equation 5.56 and δ_l is zero, or

$$\beta_{bo} = \sqrt{2\gamma\left(1+\alpha_{lo}^2\right)}\,\frac{c}{\omega_{po}}. \tag{5.62}$$

This curve shows that the compression eventually becomes reduced by almost the factor $1/\ sqrt 1 + \alpha_{lo}^2$ as δ_l gets more negative. This curve also shows that for some small positive values of δ_{lo}, the compression for this case can become greater than the completely matched case and even appears to oscillate. Again we attribute this to the phase advance term that appears in the solution for the equation of motion.

The lowest curve is completely unmatched case, in which case $\alpha_{bo} = 0$ β_{lo} is given by equation 5.56 and

$$\beta_{bo} = \sqrt{2\gamma}\,\frac{c}{\omega_{po}}. \tag{5.63}$$

This is the lowest compression case, but the curve shows that after δ_l gets less than approximately -2, the compression is independent of δ_l. As δ_l becomes positive, the change in the focusing in the lenses becomes very gradual and the unmatched compression is improved. The decrease in the lower curve at large positive δ_l occurs when the plasma density n_o longer reaches its maximum final value of $10^4 n_o$ (i.e.,

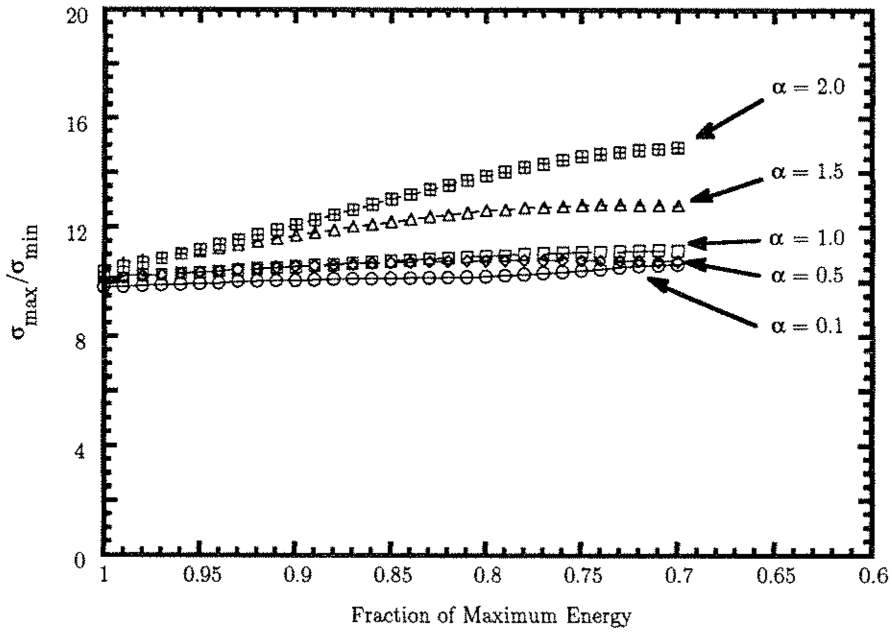

Figure 5.8: Spot size compression vs electron energy and adiabaticity factor.

$\delta_l > \alpha_{lo}/2\beta_{lo}$). The results are qualitatively the same for different values of α_{lo} between 0.0 and 2.0. The studies also show that positive δ_l must be less than or equal to α_{lo}.

5.5 Spot Size Compression vs Beam Energy Spread

The effect of beam energy spread is shown in figure 5.8, in which spot size compression is plotted versus the fractional reduction in beam energy and α_{lo}. In this simulation, all of the electrons in the beam were reduced in energy by the same amount before injection into the plasma lens. The beam energy was varied from 100% to 70%. The figure shows that the compression remains constant for small α_{lo} and increases only slightly for large α_{lo} as the energy is reduced. These curves imply that electrons that lose energy will be focused to a spot size at least as small as that of the highest energy particles. The aberrations due to energy spread should be very small in this scheme.

5.6 Summary

We have examined in detail the beam spot size compression in a ramped density plasma lens using a 2-D code. We investigated cases in which the Courant-Snyder β-function varied linearly with distance in the lens (uniform α_s), and also when the variation deviated from linearity (nonuniform α_s). The compression was found to remain constant even when the density was not ramped adiabatically and when the ramp deviated from linearity, provided that the beam and lens had matching Courant-Snyder parameters. The expected compression ratios for several beam-lens matching conditions were calculated, compared with free space focusing, and found to differ primarily according to the beam and lens α factors. The beam energy spread was found not to be a cause of chromatic aberrations in this lens, as expected. The results apply not only to a ramped density plasma lens, but to any ramped linear focusing force.

Future investigations should address nonlinearities in the focusing force. The radiation emitted by the strongly focusing particles, in both the classical regime (as done for the plasma wiggler in Chapter 4) and the quantum regime, could be calculated. The numerical code can easily be extended to 3-D, as done in the previous chapters. The code can be modified to model arbitrary focusing fields, as well as model colliding beams of various shapes.

Chapter 6

Conclusion

We began this study by examining two topics related to applications of large amplitude relativistic plasma waves; the plasma wave accelerator and plasma wave undulator. While in the process of studying the beam quality needed for coherent emission of radiation in the plasma wave undulator, we found that the beam could be used as a diagnostic of the plasma wave fields. Thus the topic of an electron beam diagnostic developed into a major part of this work. The plasma lens, which does not necessarily utilize a plasma wave, is an application of the large amplitude fields found in plasmas, and thus was easily modeled by the theoretical and computational tools developed for the previous studies.

For several years much theoretical and computational work has been done on the plasma accelerator, plasma lens and plasma undulator. Experiments are underway to test the plasma accelerator and plasma lens. Our motivation here was to support experimental efforts by concentrating on developing more detailed and physically illuminating descriptions of the beam-wave interactions than had been done by previous theoretical and computational researchers. We also endeavored to use actual experiments in progress as examples.

We have been able to describe the detailed evolution of the energy, spatial distribution, and phase evolution of electrons accelerated in the plasma wave accelerator. Comparisons were made of several ongoing or planned experiments. Estimates of the number of electron accelerated into energy ranges were given for current beat wave acceleration experiments.

We described how the scattering of a relativistic electron beam could be used as a diagnostic of a relativistic plasma wave, and gave numerical limits on its use. Details on the variation of the beam spot size as a function of several controllable parameters were given. For higher energy beams, a grating phenomenon was found in the electron distribution that could be used as a diagnostic too, but could also have some other very interesting applications in the future.

The radiation emitted by electrons drifting in the plasma undulator was described in detail. The plasma undulator was found to operate much like a traditional magnetic undulator, and thus could be described using slightly modified versions of well developed theories created for the magnetic undulator. A major experiment to test the plasma undulator is not presently underway, however, if and when that day comes, it is hoped that the results of this study will be of benefit.

Our studies of the ramped density plasma lens confirmed that small spot sizes could be obtained in high energy colliders, however we found that when the beam and lens are matched, the density ramp need not be adiabatic. We also found expressions relating the minimum spot size in the lens to the minimum spot size in free space for several beam injection configurations. Our work did not include self consistently the emission of radiation which will occur with strong focusing, and would limit the spot size due to aberrations. A natural extension of this work would be to include the radiation, both classical and quantum, self consistently.

A common idea connecting these topics is that plasmas can sustain much higher electric and magnetic fields than can be sustained in vacuum. This permits miniaturization of devices and extends the limits of their performance to higher energies, shorter wavelengths, smaller spots, and etc. The elusive plasma, however, is not without its challenges. It will be interesting to see what other new plasma-filled, rather that vacuum-filled, devices will break new ground in the future. Surely they will benefit from detailed experiment oriented investigations such as the ones performed herein.

Bibliography

[1] J. M. Dawson. Plasma Particle Accelerators. *Sci. Am.* **260**, 54 (1989).

[2] T. Tajima and J. M. Dawson. Laser Electron Accelerator. *Phys. Rev. Lett.* **43**, 267 (1979).

[3] C. Joshi, W. B. Mori, T. Katsouleas, J. M. Dawson, J. M. Kindel and D. W. Forslund. Ultrahigh gradient particle acceleration by intense laser-driven plasma density waves. *Nature* **311**, 525 (1984).

[4] P. Chen, J. M. Dawson, R. W. Huff, T. Katsouleas. Acceleration of Electrons by the Interaction of a Bunched Electron Beam with a Plasma. *Phys. Rev. Lett.* **54**, 693 (1985).

[5] P. Sprangle, E. Esarey, A. Ting, and G. Joyce. Laser wakefield acceleration and relativistic optical guiding. *Appl. Phys. Lett.* **53**, 2146 (1989).

[6] E. Esarey, A. Ting, P. Sprangle and G. Joyce. The Laser Wakefield Accelerator. *Comments Plasma Phys. and Controlled Fusion* **12**, 191 (1989).

[7] C. Clayton, C. Joshi, C. Darrow and D. Umstadter. Relativistic Plasma-Wave Excitation by Collinear Optical Mixing. *Phys. Rev. Lett.* **54**, 2343 (1985).

[8] C. Clayton, C. Joshi, W. Leemans, K. Marsh and R. Williams. Beat Wave Development Work. *Advanced Accelerator Concepts*, AIP Conf. Proc. **No. 193**, edited by C. Joshi, (AIP, New York,1989), p. 37.

[9] A. E. Dangor, A. Dymoke Bradshaw, R. Bingham, R. G. Evans, C. B. Edwards and W. T. Toner. The Rutherford Laboratory Beat Wave Experiment. *Laser Acceleration of Particles* AIP Conf. Proc. **No. 130**, edited by C. Joshi. and T. Katsouleas (AIP, New York, 1985), p. 130.

[10] Y. Kitagawa, K. Mima, S. Nakayama, T. Matsumoto, T. Minamihara, K. Sawai, H. Takabe, T. A. Tanaka, H. Azechi, K. Nishihara, Sadao S. Nakai. Relativistic Electron Beam-CO2 Interaction S Program. *Conference on Lasers and Electro-Optics (CLEO)*, Anaheim, Ca., Technical Digest Series, 7, Optical Society of America, Washington, D.C. 1988.

[11] G. Matthieussent. G. 1989 private communication.

[12] F. Martin, P. Brodeur, J. P. Matte, H. Pepin and N. Ebrahim. High Intensity Laser Processes. *Proc. of SPIE*, (A.J. Alcock, ed) **664**, 20 (1986).

[13] N. A. Ebrahim. Experiments on the Plasma Beat-Wave Accelerator. *IEEE Tran. Nucl. Sci.*, **NS-35** 3539 (1985).

[14] J. B. Rosenzweig, D. B. Cline, B. cole, H. Figueroa, W. Gai, R. Konecny, J. Norem, P. Schoessow and J. Simpson. Experimental Observation of Plasma Wake-Field Acceleration. *Phys. Rev. Lett.* **61**, 98 (1988).

[15] A. Ogata, S. Enomoto, K. Nakajima and F. Nakanishi. Experiment of the Plasma Wake-Field Accelerator at the KEK Linac. *Bull. Am. Phys. Soc.* **34**, 211 (1989).

[16] C. Darrow, M. D. Perry, F. Patterson, E. M. Campbell, T. Katsouleas and W. B. Mori. High Brightness Laser Development at LLNL and Possible Applications to the Laser Wakefield Problem. *Advanced Accelerator Concepts*, AIP Conf. Proc. **No. 193**, edited by C. Joshi, (AIP, New York,1989), p. 50.

[17] A. Gizzo, P. Bertand, M. M. Shoucri, T. W. Johnston, E. Fijalkow and M. R. Feix. A Vlasov Code for the Numerical Simulation of Stimulated Raman Scattering. *J. Comput. Phys.* **90**, 431 (1990).

[18] D. W. Forslund, J. M. Kindel, W. B. Mori, C. Joshi and J. M. Dawson. Two-Dimensional Simulations of Single-Frequency and Beat-Wave Laser-Plasma Heating. *Phys. Rev. Lett.* **54**, 558 (1985).

[19] T. Katsouleas, S. Wilks, P. Chen, J. M. Dawson and J. J. Su. Beam Loading in Plasma Accelerators. *Part. Accel.* **22**, 81 (1987).

[20] T. Katsouleas, C. Joshi, J. M. Dawson, F. F. Chen, C. Clayton, W. B. Mori, C. Darrow and D. Umstadter. *Plasma Accelerators*, in Laser Acceleration of Particles, AIP Conf. Proc. **No. 130**, edited by C. Joshi. and T. Katsouleas (AIP, New York, 1985), p. 63.

[21] J. L. Bobin. Lasers and Plasmas in Particle Acceleration, Proc. of the Workshop on New Developments in Particle Acceleration Techniques. *CERN 87-11, ECFA 87/110*, Orsay edited by S. Turner (CERN, Geneva, 1987) p. 58.

[22] T. Katsouleas. Physical Mechanisms in the Plasma Wake-Field Accelerator. *Phys. Rev.* **A 33**, 2056 (1986).

[23] J. D. Lawson. Beat-Wave Accelerator Studies at the Rutherford Appleton Laboratory. *Laser Acceleration of Particles*, AIP Conf. Proc. **No. 130**, edited by C. Joshi and T. Katsouleas (AIP, New York 1985), p. 120.

[24] R. Fedele, U. de Angelis and T. Katsouleas. Generation of Radial Fields in the Beat-Wave Accelerator for Gaussian Pump Profiles. *Phys. Rev.* **A 33**, 4412 (1986).

[25] R. L. Williams, C. E. Clayton, C. Joshi, T. Katsouleas, and W. B. Mori. Studies of Relativistic Wave-Particle Interactions in Plasma-Based Collective Accelerators. *Laser and Particle Beams* **8**, 427 (1990).

[26] A. Dyson and A. E. Dangor. Laser Beat Wave Acceleration of Particles. *Laser and Particle Beams* **9**, 619 (1991).

[27] C. E. Clayton, C. Darrow, and C. Joshi. Novel Small-Angle Collective Thomson Scattering System. *Appl. Opt.* **24**, No. 17, 2823 (1985).

[28] C. Joshi, T. Katsouleas, J. M. Dawson, Y. T. Yan, J. M. Slater. Plasma Wave Wigglers for Free-Electron Lasers. *IEEE J. Quantum Elec.* **QE-23**, No. 9, 1571 (1987).

[29] R. L. Williams, C. E. Clayton, C. Joshi, and T. Katsouleas. Motion of Relativistic Electrons Through Transverse Relativistic Plasma Waves. *Rev. Sci. Instrum.* **61** (10) 3037 (1990).

[30] A. M. Sesslser and D. Vaughn. Free-Electron Lasers. *American Scientist* **75**, 34 (1987).

[31] H. Winick, G. Brown, K. Halbach and J. Harris. Wigglers and Undulator Magnets. *Physics Today* **34**, 50 (1981); H. Winick, Synchrotron Radiation, *Sci. Am.* **257 No.5**, 88 (1987).

[32] J. E. La Sala, D. A. Deacon and J. M. M. Madey. Performance of an XUV Oscillator on the Stanford Storage Ring. *Nucl. Instr. and Meth.* **A250**, 262 (1986).

[33] J. M. J. Madey. Stimulated Emission of Bremsstrahlung in a Periodic Magnetic Field. *J. Appl. Phys.* **42**, 1906 (1971).

[34] H. Motz. Applications of the Radiation from Fast Electron Beams. *J. Appl. Phys.* **22**, 527 (1951).

[35] C. W. Roberson and P. Sprangle. A Review of Free-Electron Lasers. *Phys. Fluids* **B 1**, 3 (1989).

[36] S. A. Bogacz, J. B. Ketterson and G. K. Wong. Coherent Short Wave Radiation from a Solid State Free Electron Laser. *Nucl. Instr. and Meth.* **A250**, 328 (1986).

[37] M. Cohen, A. Gover and S. Ruschin. A Scheme for XUV Generation Based on a Laser-Pumped EEL with an Axial Electric Field. *Nucl. Instr. and Meth.* **A304**, 673 (1991).

[38] A. V. Zege. Advantages of the 'kinetic' amplification regime in a free electron laser with optical undulator. *Nucl. Instr. and Meth.* **A304**, 520 (1991).

[39] P. Dobiasch,P. Meystre and M. O. Scully. Optical Wiggler Free- Electron X-ray Laser in the 5 A Region. *IEEE J. Quantum Electronics* **QE-19**, 1812 (1983).

[40] V. A. Bazylev. Free Electron Laser in the Ultraviolet and X-ray Regions. *Nucl. Instr. and Meth.* **A304**, 671 (1991).

[41] V. G. Baryshevsky, I. Ya. Dubovskaya, and A. V. Zege. X-ray free electron laser in a crystal as distributed feedback oscillator. *Nucl. Instr. and Meth.* **A304**, 421 (1991).

[42] R. Bingham, U. de Angelis, P. K. Shukla and L. Stenflo. Large Amplitude Waves and Fields in Plasmas. Proceedings of the 2nd Week of the Spring College on Plasma Physics, *PHYSICA SCRIPTA* **T30**, see numerous articles (1990).

[43] R. L. Williams, C. E. Clayton, C. E. Joshi, T. Katsouleas, W. B. Mori and Jack Slater. Theory and Experiments on the Generation of Spontaneous Emission Using a Plasma Wave Undulator: A Progress Report. *SPIE Proc. on Free-Electron Lasers and Applications*, Series P, Edited by D. Prosnitz, **Vol. 1227**, 48 (1990).

[44] R. Fedele, G. Miano and V. G. Vaccaro, The Plasma Undulator. *Physica Scripta* **T30**, 192 (1990).

[45] Lalita, V. K. Tripathi and P. C. Agarwal. Radiation Guiding in a Plasma Wave Wiggler Free-Electron Laser. *IEEE Trans. Plasma Sci.* **19**, 9 (1991).

[46] A. Loeb and S. Eliezer. Free-Electron Laser and Laser Electron Acceleration Based on the Megagauss Magnetic Fields in Laser- Produced Plasmas. *Phys. Rev. Lett.* **56**, 2252 (1986).

[47] J. A. Stamper, E. A. McLean and B. H. Ripin. Studies of Spontaneous Magnetic Fields in Laser-Produced Plasmas by Faraday Rotation. *Phys. Rev. Lett.* **40**, 1177 (1978).

[48] Y. T. Yan and J. M. Dawson. ac Free-Electron Laser. *Phys. Rev. Lett.* **57**, 1599 (1986).

[49] T. H. Chung and J. H. Lee. Analysis of the ac Free Electron Laser. *IEEE Trans. Plasma Sci.* **18**, 651 (1990).

[50] Y. T. Yan. Output power enhancement of ac Raman Free Electron Laser. *Nucl. Instr. and Meth.* **A272**, 120 (1988).

[51] W. B. Colson. Free Electron Laser Theory. Ph.D. Thesis, Stanford Univ (1977).

[52] W. B. Colson. One-Body Analysis of Free Electron Lasers. *Physics of Quantum Electronics,* **Vol. 5**, ed. S. Jacobs, M. Sargent and M. Scully (Addison-Wesley) Ch. 4 (1978).

[53] W. B. Mori. Theory and Simulations on Beat Wave Excitation of Relativistic Plasma Waves. Ph.D. Thesis, UCLA (1987).

[54] J. D. Jackson. *Classical Electrodynamics* Second Ed. (John Wiley, New York) Chapter 14 (1975).

[55] W. B. Colson. The Nonlinear Wave Equation for Higher Harmonics in Free-Electron Lasers. *IEEE J. Quantum Electron.* **QE-17**, 1417 (1981).

[56] W. B. Colson, G. Dattoli and F. Ciocci. Angular-Gain Spectrum for Free-Electron Lasers. *Phys. Rev.* **A 31**, 828 (1985).

[57] S. Ramo, J. R. Whinnery, and T. Van Duzer. *Fields and Waves in Communications Electronics.* (John Wiley, New York) Chapter 12.23, (1965).

[58] P. Chen. A Possible Final Focusing Mechanism for Linear Colliders. *Part. Accel.* **20**, 171 (1987).

[59] B. Richter. Very High Energy Colliders. *IEEE Tran. Nucl. Sci.* NS- **32**, 3828 (1985).

[60] R. B. Palmer. The Interdependence of Parameters for TeV Linear Colliders. SLAC Pub. 4295, 1987.

[61] P. B. Wilson. Linear Accelerators for TeV Colliders. SLAC Pub. 3674 (Rev.), 1985.

[62] K. Oide. Synchrotron-Radiation Limit on the Focusing of Electron Beams. *Phys. Rev. Lett.* **61**, 1713 (1988).

[63] P. Chen, K. Oide, A. M. Sessler and S. S. Yu. An Adiabatic Focuser. *Part. Accel.* **31**, 7 (1990).

[64] D. H. Whittum. Theory of the Ion-Channel Laser. Ph.D. Thesis. UC Berkeley, 1990 and LBL Report LBL-29720.

[65] D. H. Whittum. A Continuous Plasma Final Focus. Proceedings of the Topical Conference on Research Trends in Nonlinear and Relativistic Effect in Plasmas, edited by V. Stefan, (LaJolla, 1990) and LBL report LBL-28644 (LBL-27965 Rev.).

[66] A. Gabor. A Space-Charge Lens for Focusing of Ion Beams. *Nature* **160**, 89 (1947).

[67] B. V. Borries and E. Ruska. Das kurze Raumladungsfeld einer Hilfsentladung als Sammellinse für Kathodenstralen. *Z. Phys.* **76**, 649 (1932).

[68] B. Autin, H. Riege, E. Boggasch, K. Frank, L. De Menna, and G. Miano. A Z-Pinch Plasma Lens for Focusing High-Energy Particles in an Accelerator. *IEEE Trans. Plasma Sci.* **PS-15**, 226 (1987).

[69] T. G. Roberts and W. H. Bennett. The Pinch Effect in Pulsed Streams at Relativistic Energies. *Plasma Physics* **10**, 381 (1968).

[70] European Organization for Nuclear Research. *Workshop on Plasma Focusing.* CERN PS/87-99 (AA), (Geneva, 1988). Many articles on plasma lenses are contained therein.

[71] S. Turner, editor. New Developments in Particle Acceleration Techniques. *CERN 87-11, ECFA 87-110*, (Orsay, 1987). Some articles on plasma lenses are contained therein.

[72] Y. Qingchang and Q. Hong. Self-Sustaining Space-Charge Lens. *Nucl. Instr. and Meth.* **A 311**, 14 (1992).

[73] P. Chen, J. J. Su, T. Katsouleas, S. Wilks, and J. M. Dawson. Plasma Focusing for High Energy Beams. *IEEE Trans. Plasma Sci.* **PS-15**, 218 (1987).

[74] T. Katsouleas, J. J. Su, and J. M. Dawson. Plasma Lens Work at UCLA. European Particle Accelerator Conference, Rome, Italy, June 7-11, 1988.

[75] T. Katsouleas, J. J. Su and J. M. Dawson. Underdense Plasma Lenses for Focusing Particle Beams. Proceedings of Linear Accelerator Conference, Newport News, Virginia, Oct. 3-7, 1988.

[76] J. J. Su, T. Katsouleas, J. M. Dawson, and R. Fedele. Plasma Lens for Focusing Particle Beams. *Phys. Rev.* **A 41**, 3321 (1990).

[77] T. Katsouleas, J. J. Su, W. B. Mori, and J. M. Dawson. Plasma Physics at the final focus of high-energy colliders.*Phys. Fluids* **B 2**, 1384 (1990).

[78] J. B. Rosenzweig, B. Cole, D. Larson, and D. B. Cline. Luminosity Enhancement in Linear Colliders Using a Short-Focal-Length Plasma Lens. *Part. Accel.* **24**,11 (1988).

[79] J. B. Rosenzweig, P. Chen. Beam Optics of a Self-Focusing Plasma Lens. *Phys. Rev.* **D 39**, 2039 (1989).

[80] J. B. Rosenzweig, P. Schoessow, B. Cole, W. Gai, R. Konecny, J. Norem, and J. Simpson. Experimental Measurement of Nonlinear Plasma Wake Fields. *Phys. Rev.* **A 39**,1586 (1989).

[81] P. Chen, S. Rajagopalan, and J. B. Rosenzweig. Final Focusing and Enhanced Disruption from an Underdense Plasma Lens in a Linear Collider. *Phys. Rev.* **D 40**, 923 (1989).

[82] J. J. Su. Plasma Wake Field Excitation by Charge Particle Beams. Ph.D. Thesis, UCLA, 1990.

[83] J. B. Rosenzweig, P. Schoessow, B. Cole, C. Ho, W. Gai, R. Konecny, S. Mtingwa, J. Norem, M. Rosing, and J. Simpson. Demonstration of Electron Beam Self-Focusing in Plasma Wake Fields. *Phys. Fluids* **B 2**, 1376 (1990).

[84] J. B. Rosenzweig, B. Breizman, T. Katsouleas, and J. J. Su. Acceleration and Focusing of Electrons in Two-Dimensional Nonlinear Plasma Wake Fields. *Phys. Rev.* **A 44**, 6189 (1991).

[85] R. J. Briggs. Collective Acceleration for Electrons *Phys. Rev. Lett.* **54**, 2588 (1985).

[86] H. Nakanishi, Y. Yoshida, T. Ueda, T. Kozawa, H. Shibata, K. Nakajima, T. Kurihara, N. Yugami, Y. Nishida, T. Kobayashi, A. Enomoto, T. Oogoe, H. Kobayashi, B. S. Newberger, S. Tagawa, K. Miya, and A. Ogata. Direct Observation of Plasma-Lens Effect. *Phys. Rev. Lett.* **66**, 1870 (1991).

[87] T. Katsouleas and R. Williams. Some Curious Aspects of Plasma Wakefields and Lenses. Proc. U.S./Japan Workshop on Non-linear Beam Dynamics and Accelerator Mechanisms, Tsukuba, Japan, Oct. 21-24, 1990.

[88] D. Betz, P. Chen, D. Cline, M. Gundersen, C. Joshi, T. Katsouleas, J. Norem, S. Rajagopalan, J. Rosenzweig, J. J. Su, and R. Williams. Plasma Lenses for SLAC Final Focus Test Facility. Proc. IEEE PAC Conf., San Francisco, May 6-9, 1991.

[89] T. Katsouleas. A Tapered Plasma Funnel for Focusing Electron Beams. Univ. Southern California, Pulsed Power Applied Physics Report, 1991, unpublished.

[90] E. D. Courant and H. S. Snyder. Theory of the Alternating-Gradient Synchrotron. *Ann. Phys.* **3**, 1 (1958).

[91] J. D. Lawson. *The Physics of Charged-Particle Beams.* Clarendon Press, Oxford, 1988.

[92] Stanley Humphries, Jr. *Charged Particle Beams.* John Wiley & Sons, Inc., New York, 1990.

[93] F. F. Chen. Excitation of Large Amplitide Plasma Waves. Proceedings of the 2nd Week of the Spring College on Plasma Physics, *PHYSICA SCRIPTA* **T30**, 14 (1990).

[94] W. P. Leemans. Interferometric Study of a Preionized Theta- Pinch Plasma. M.S. Thesis, UCLA (1987).

[95] C. Joshi, C. Clayton, K. Marsh, R. Williams and W. Leemans. Experimental Work at UCLA on the Plasma Beat Wave Accelerator. *New Developments in Particle Acceleration Techniques* (Edited by S. Turner), CERN Publication 87-11, **II**, 351 (1987).

[96] W. P. Leemans, C. E. Clayton and C. Joshi. Detection of Trapped Magnetic Fields in a Theta Pinch using a Relativistic Electron Beam. *Rev. Sci. Instrum.* **59 (8)**, 1641 (1988)

[97] Y. Kitagawa, T. Matsumoto, T. Minamihata, K. Sawai, K. Mina, K. Nishihara, H. Azechi, K. A. Tanaka, H. Takabe and S. Nakai. Demonstration of Electron Acceleration by a Beatwave excited Plasma Wave. ILE Report, Osaka University, Japan, unpublished.

[98] Y. Kitagawa, T. Matsumoto, T. Minamihata, K. Sawai, K.Matsuo, K. Mima, K. Nishihara, H. Azechi, K. A. Tanaka, H. Takabe and S. Nakai. Beat-Wave Excitation of Plasma Wave and Observation of Accelerated Electrons. *Phys. Rev. Lett.* **68**, 48 (1992).

[99] K. Estabrook and W. L. Kruer. Theory and simulation of one- dimensional Raman backward and forward scattering. *Phys. Fluids* **26(7)**, 1892 (1983).

[100] A. E. Dangor, A. K. L. Dymoke-Bradshaw, A. Dyson, T. Garvey, I. Mitchell, A. J. Cole, C. N. Danson, C. B. Edwards, and R. G. Evans. Generation of uniform plasma for beat wave experiments. *IEEE Trans. Plasma Sci.* **PS-15**, 161 (1987).

[101] W. P. Leemans, C. E. Clayton, K. A. Marsh, A. Dyson, and C. Joshi. Suitability of Tunneling Ionization Produced Plamas for the Plasma Beat Wave Accelerator.

Appendices

Appendix A

Tables for Plasma Wave Acceleration Experiments

In this appendix are collected some tables that are relevant to laser plasma beatwave acceleration experiments.

Table A.1 is a list of lasers currently used in beatwave acceleration experiments. Table A.2 is a comparison of beatwave accelerator properties.

	9.6 μm	10.3 μm	10.6 μm	1.05 μm	1.06 μm
λ (cm)	0.0009552	0.0010274	0.0010590	0.0001053	0.0001064
k (cm^{-1})	6577.53	6115.44	5932.63	59669.38	59052.49
ω (rad/s)	1.97×10^{14}	1.83×10^{14}	1.78×10^{14}	1.79×10^{15}	1.77×10^{15}
n_c (cm^{-3})	1.22×10^{19}	1.06×10^{19}	9.94×10^{18}	1.01×10^{21}	9.85×10^{20}

Table A.1: Lasers used in plasma beatwave acceleration experiments.

	9.6, 10.6 μm	9.6, 10.3 μm	10.3, 10.6 μm	1.05, 1.06 μm
λ_p (cm)	0.0097428	0.0135972	0.0343695	0.0101853
k_p (cm^{-1})	644.9	462.09	182.81	616.88
ω_p (rad/s)	1.93×10^{13}	1.39×10^{13}	5.48×10^{12}	1.85×10^{13}
n_o (cm^{-3})	1.17×10^{17}	6.03×10^{16}	9.44×10^{15}	1.07×10^{17}
v_{phase}	2.981×10^{10}	2.990×10^{10}	2.996×10^{10}	2.997×10^{10}
β_{phase}	0.99467	0.99735	0.99954	0.99995
γ_{phase}	9.70	13.73	32.95	96.23
$L_{acceleration}$ (cm)	0.58	1.63	23.75	60.04
γ_{max} $(\epsilon = 1)$	376.3	754.4	4343.3	37038.7
Labs	UCLA ILE INRS	UCLA	UCLA	RAL EP

Table A.2: Properties of laser excited beatwaves used in PBWA experiments.

Appendix B

Comments on the UCLA Beatwave Acceleration Experiments

In this appendix we discuss three plasma sources used in the UCLA beatwave experiments: the theta pinch, the multi-cathode arc, and the gas jet. Simulation results of electron acceleration for each source are given. In the UCLA laser plasma beatwave experiments two beams from a CO_2 laser are generated, shortened, amplified, and focused colinearly into a dense plasma. The plasma density is adjusted so that the plasma frequency matches the difference frequency (beat frequency) of the two lasers. The beating lasers resonantly excite a relativistic plasma wave. Electrons are injected into the plasma concurrently with the lasers and are accelerated by the plasma wave as described in Chapter 2. Figure B.1 shows the arrangement of components in the beatwave experiments at UCLA. The three plasma sources are sketched in figure B.2 and their properties are given in table B.1. A discussion on these and several other plasma sources for producing large amplitude plasma waves is given by Chen[93]. The original plasma source used was the theta pinch (figure B.2(a) and table B.1 which is described in detail by Leemans[94]. Simulation results of the number of electrons accelerated in the theta pinch that also would be

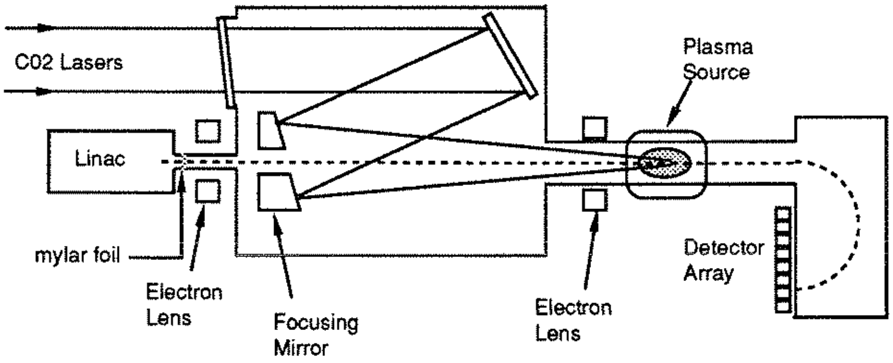

Figure B.1: Sketch of beatwave acceleration experiment at UCLA.

Source	Theta Pinch	Multi-Cathode Arc	Plasma Jet
wavelengths (μm)	9.6, 10.6	10.3, 10.6	9.6, 10.6
$n_{resonant}$ (cm^{-3})	5.8×10^{16}	8.0×10^{15}	1.0×10^{17}
$n_{measured}$ (cm^{-3})	$10^{15} - 10^{17}$	$10^{15} - 10^{17}$	10^{19} at 1500 psi
			10^{17} at 30 psi
plasma size	2.5 cm dia.	5 - 7 mm dia	1.5 mm dia.
	20 cm long	1 cm long	1.5 mm long
plasma wave length	0.75 - 3 mm	2 - 4 mm	1.5 mm
$\epsilon = n_1/n_0$	2 - 17%	5 - 7%	10%
fill gas	H_2 or He	H_2	H_2
gas pressures	0.1 - 1.7 T	0.5 - 3 T	1.7 T
pulsed B field	20 kG	400 G	none
trapped B field	1 - 2 kG	none	none
Power Source:			
current	350 kA	2 kA or 25 kA	n/a
charging voltage	28 kV	5 kV or 3 kV	n/a
capacitance	11.1 μF	1.8 μF	n/a
inductance	72 nH	0.4 μH	n/a
stored energy	4.3 kJ	23 J or 8 J	n/a
pulse period	6 μs	10 μs	n/a

Table B.1: Properties of plasma sources used in UCLA beatwave acceleration experiments.

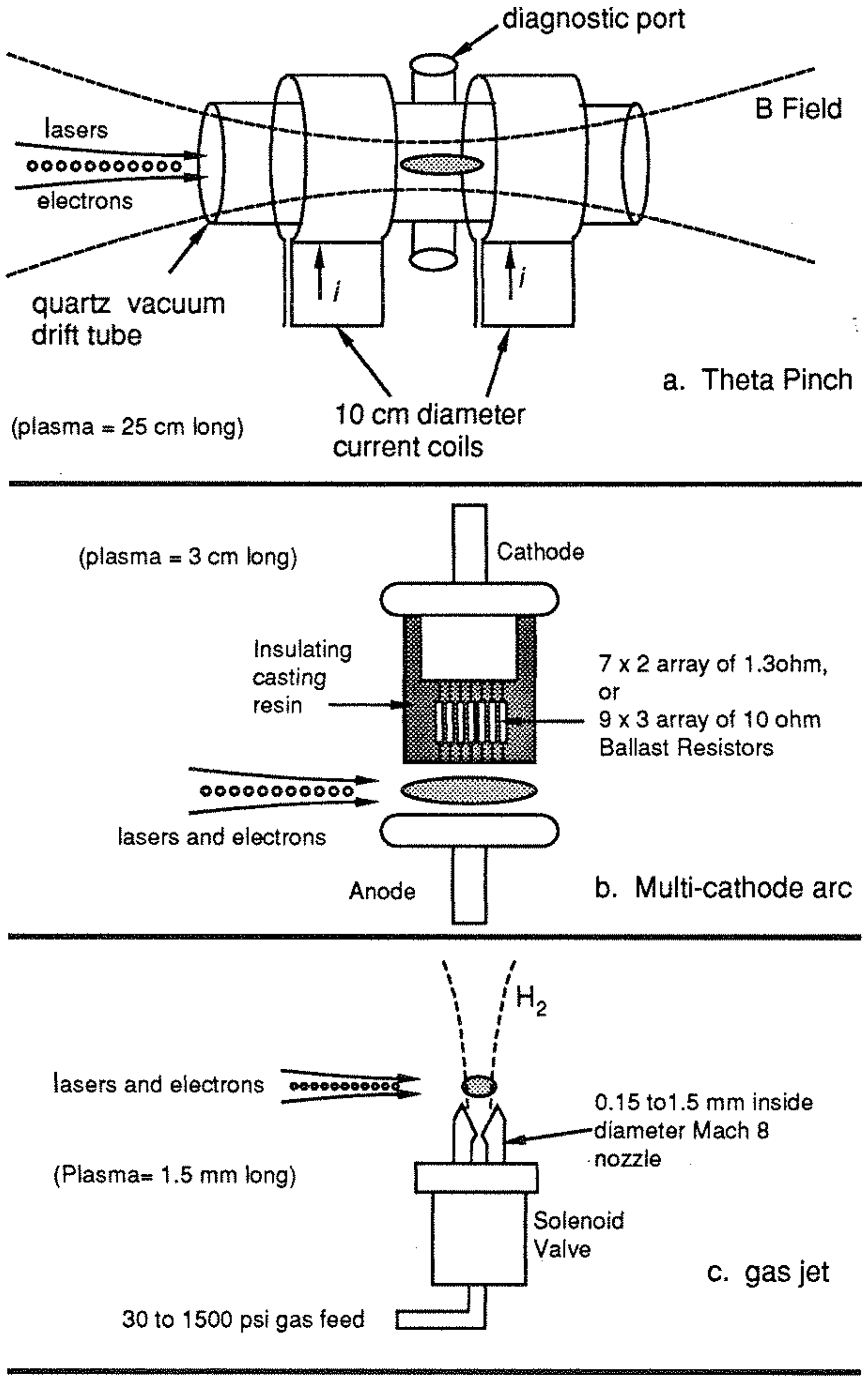

Figure B.2: Plasma sources for the UCLA beatwave experiment. (a) Theta pinch, (b) multi-cathode arc, and (c) gas jet.

detected by the original spectrometer are shown in figure 2.16 of Chapter 2. For figure 2.16, 250,000 electrons having $\gamma_o = 4$ were injected into a beatwave having $\gamma_p = 14$ and $\epsilon = 2\%$ to 17%, accelerated for 3.0 mm to 0.75 mm, and collected in a half angle of 8 deg. The Chapter 2 results show that only 1's to 10's of electrons are expected to be detected due to the large radial electric fields in the plasma wave, marginal electron injection energy, and large beam emittance. A detailed experimental study[96] showed that large amplitude plasma waves could be excited but that the theta pinch plasma contained trapped magnetic fields (about 4 kGauss) which could deflect electrons from the beam. These magnetic fields would further reduce the electrons detected to below the numbers of figure 2.16, as shown in figure 2.20. Full beatwave acceleration experiments were performed but no electrons were detected[8] Subsequently, improvements were made to the electron injector and the theta pinch plasma was replaced with an arc plasma source.

A multi-cathode arc plasma source (figure B.2(b) and table B.1 was installed and tested by injecting the electron beam through it. Beam trajectory calculations showed that the large azimuthal magnetic field (about 400 Gauss) near the arc current deflected the electrons as they approached the plasma. The electrons passed through the plasma wave at an angle (about 12 deg) instead of parallel to it. This reduced the interaction time between the electrons and wave. Additional simulations were performed to obtain the energy spectrum of the accelerated electrons and was based on using the original unimproved electron injector. The simulation results are summarized in figure B.3 and show that the number of electrons accelerated and their energies decreased as the angle of injection was increased from 0 to 12 deg. For figure B.3, 250,000 electrons having $\gamma_o = 4$ were injected into a beatwave having $\gamma_p = 34$ and $\epsilon = 5\%$, accelerated for 2.0 mm, and collected in a half angle of 8 deg. Experiments were performed but it was difficult to control the

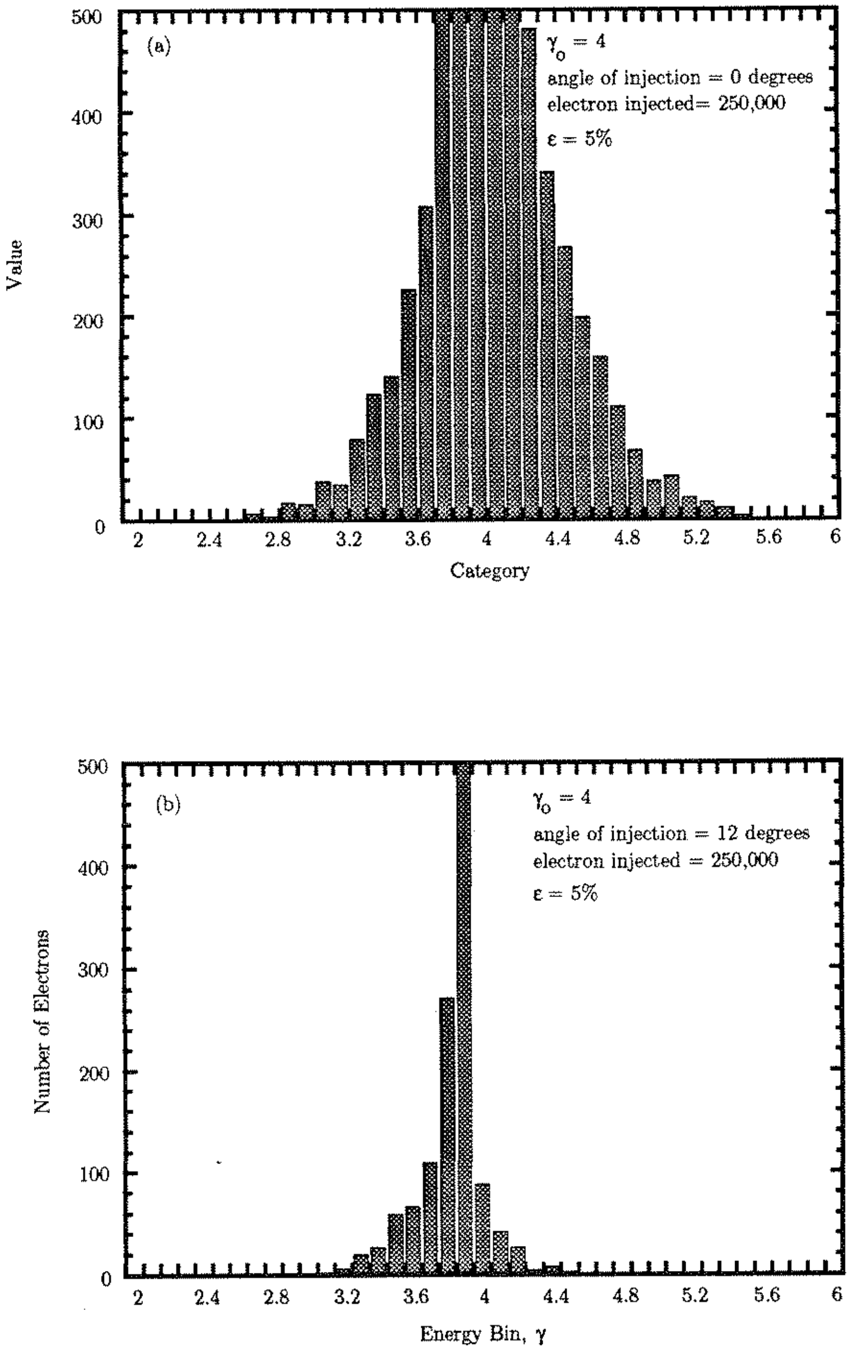

Figure B.3: Histogram of electrons accelerated in the multi-cathode arc source for (a) zero degree injection angle and (b) 12 degree injection angle.

injection of electrons into the plasma at an angle. To overcome these difficulties a gas jet plasma source was introduced.

The gas jet plasma source (figure B.2(c) and table B.1 does not contain a magnetic field to perturb the electrons. Simulations were performed for electron injection into three gas jet plasma waves of different ϵ, and the results are shown in figurec B.4(a), (b), and (c). For these figures 250,000 electrons having $\gamma_o = 5$ were injected into a beatwave having $\gamma_p = 14$ and $\epsilon = 10\%$, 3%, and 1%, accelerated for 1.5 mm, and collected in a half angle of 6 deg. The histogram of accelerated electron energies, the energy versus longitudinal and transverse positions, and the phase space trajectory are shown in each figure. These summaries are based on using the improved electron injector which was increased in energy from $\gamma = 4\%$ to 5. The injector's emittance was decreased from 20 mm-mrad to 3 mm-mrad so that a smaller beam focus could be obtained at the laser focus resulting in better overlap between the electron beam and plasma wave. The magnetic spectrometer was redesigned to detect smaller increases in electron energy. A cloud chamber immersed in a magnetic field was introduced as an alternate electron energy diagnostic. The simulations show that the number of detectable electrons accelerated in the gas jet plasma source will be on the order of thousands. Full electron acceleration experiments utilizing the gas jet plasma source remain to be performed.

We note that the tunneling ionization method was also investigated as a way to obtain uniform high density plasma, as discussed in detail in reference [101]. The plasma source in this case is just the gas filled vacuum chamber, and is not shown or listed in figure B.2 or table B.1. The density obtained by tunneling ionization was limited to below 1 to 2 $\times 10^{16}$ cm^{-3}. This limit was due to laser refraction in a long plasma which prevented the laser from completely focusing and having the required intensity for producing the desired ionization and density. The gas jet

?

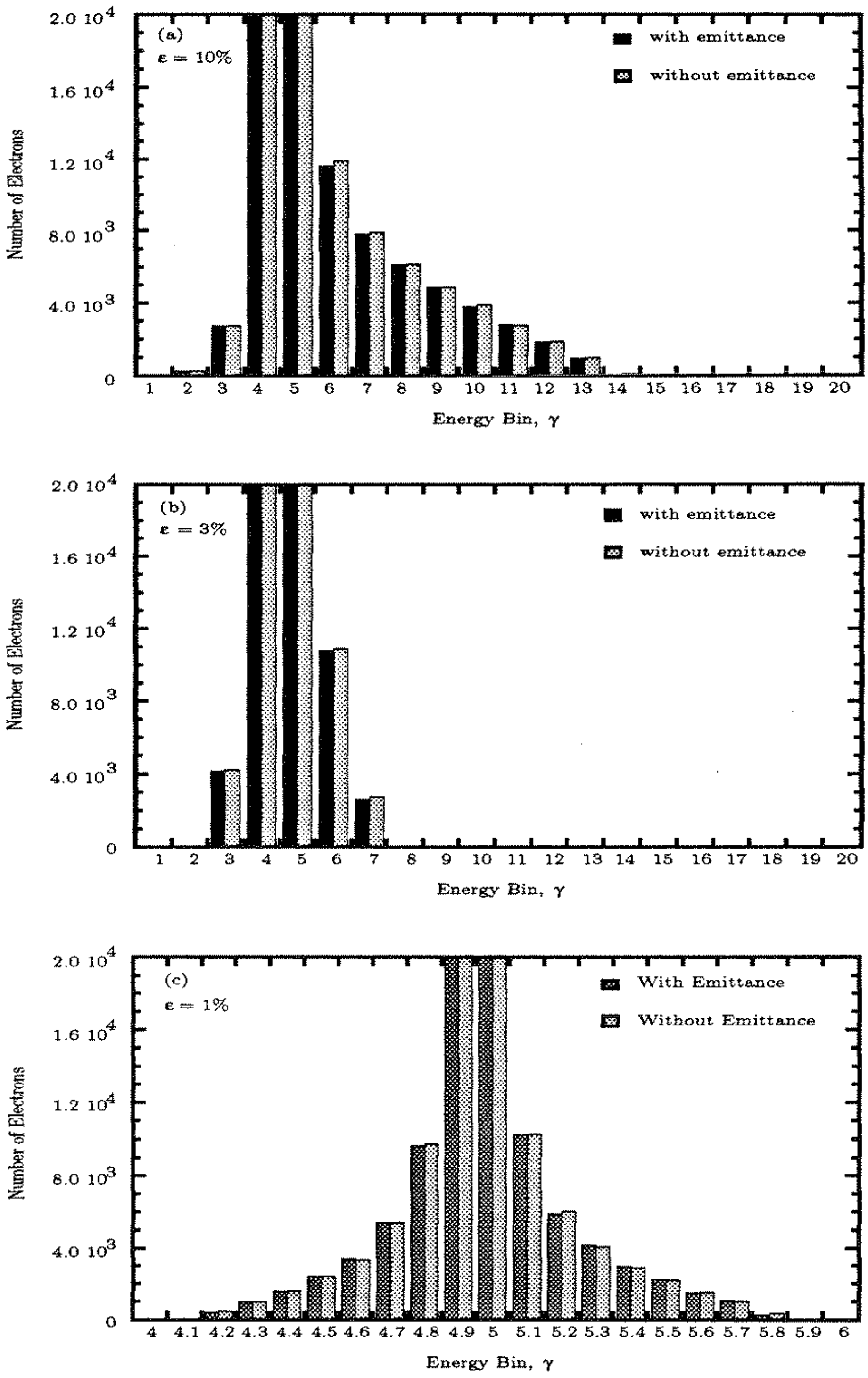

Figure B.4: Histogram of electrons accelerated in the plasma jet sourcee for (a) $\epsilon = 10\%$, (b) $\epsilon = 3\%$, and (c) $\epsilon = 1\%$.

plasma source is short and thus laser refraction should not be a problem.

Appendix C

Electron Energy Data Acquisition System

In this Appendix we discuss the electronic data acquisition system for measuring and recording the accelerated electron energies. Magnetic spectrometers were located at the output of the UCLA beatwave acceleration experiments to momentum analyze the accelerated electrons. The spectrometers deflected electrons onto a linear array of silicon surface barrier detectors. The array consisted of up to eight detectors. Several spectrometers were available and their geometries and field strengths could be readily varied to suit different experimental configurations. The detectors could be substituted at the output of any of these spectrometers. A schematic of the data acquisition system is shown in figure C.1. The system consists of a spectrometer, detectors, preamps, differentiators, inverters, power splitter, attenuators, eight- channel amplifier, sixteen channel analog-to-digital converter, computer, and various power supplies.

A small number of accelerated electrons was predicted in the numerical simulations discussed in Chapter 2, therefore the detectors needed to be very sensitive. The system was designed to permit detection of single electrons incident on the

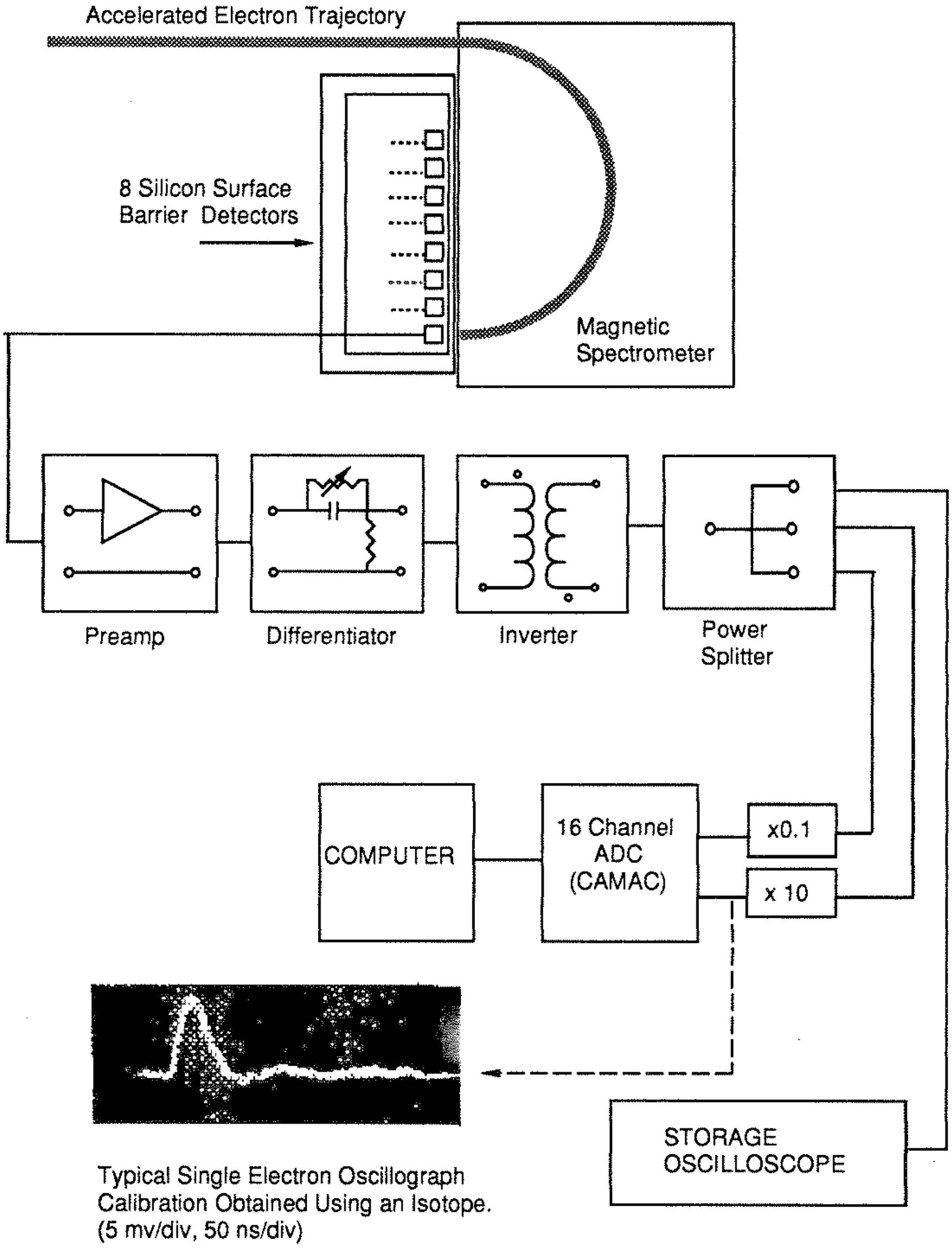

Figure C.1: Electron detection system and oscillograph of single electron calibration pulse.

detectors. The silicon surface barrier detector consists of a 1000 μm thick p-type silicon wafer in contact with a 0.18 mm aluminum window. The wafer diameter is about 10 mm which restricted the energy resolution to several hundred electron volts for most of the spectrometer configurations used. An electron passing through the silicon wafer loses a small amount of enegry energy which goes into creating electron-hole pairs. Biased electrodes collect the charges, which causes a voltage pulse to appear at the output of the detectors. The rate of energy loss in silicon, dE/dx, is approximately constant for electrons in the range of 0.7 to 7.0 MeV ($\gamma = 2.4$ to 14) which includes the range of energies most of the spectrometers are configured to detect. Therefore the expected magnitude of the output pulse would be approximately constant for any electron in the energy range of interest. Also, this feature would permit counting the number of electrons in an energy bin because the magnitude of the detector output would be directly proportional to the number of electrons incident at one time.

The voltage signal from one electron was determined by placing beta emitting isotopes, Co^{60} or Sr^{90}, over the entrance to the detectors. The isotope emits a spectrum of beta energies, however the highest energy electrons, which had range greater than the thickness of the detectors, were used to obtain a calibration of the system in units of volts/electron. The output of the detector was nominally a 3 mV positive step pulse with 500 msec decay. The preamps were located at the detectors and transmitted the pulse by coax cables to a screen room located about 10 m away. A differentiating filter shaped the pulse and a transformer converted its polarity to suit the input requirements of the amplifier and ADC. The amplitude and width of the pulse could be modified by changing the components in the filter, but nominally it was a 10 mV pulse with 50 nsec width, an example of which is shown in figure C.1. A power splitter was used to obtain three pulses, one of which was recorded on a storage oscilloscope in order to provide an analog record. Another pulse was attenuated (÷10) and another was amplified (×10) to provide a dynamic range of 100. These two signals were put into an analog-to-digital converter (ADC) located in a CAMAC system. The digital data was collected on a PC microcomputer running a custom written program in BASIC to control the CAMAC system. In later experiments a Macintosh II running LABVIEW was used. Triggers for the ADCs were synchronized with the laser triggers so that data were digitized only after accelerated electrons had arrived at the detectors.

The detectors and preamplifers were located in a double shielded enclosure to reduce electromagnetic interference. X-ray noise on the detectors due to low energy electrons, from the linac being dumped or hitting various surfaces, could be reduced to a level much below the single electron noise using lead shielding. X- ray noise from the high power lasers occurred many milliseconds before the electron pulses arrived at the detectors, and thus did not interfere with detection.

Appendix D

Comments on the Osaka University Beatwave Acceleration Experiment

In this appendix we examine the results of the Osaka University's CO_2 beatwave experiment in which electrons were reported to be accelerated from "initial energies less than 10 MeV to 20 Mev or even more than 20 MeV".[97] [98] The results of the experiment will be analyzed using the 1-D computational tools presented in Chapter 2. The parameters of the experiment were $\gamma_p \approx 10\%$, $n_1/n_o \approx 3\%$, length of wave $\approx$ 3 mm, and total plasma length $\approx$ 7 mm. The plasma was produced by laser irradiation (9.569 and 10.591 mm) of H_2 gas which was injected via a puff value into a vacuum chamber. The beatwave was detected concurrently with accelerated electrons. No electrons were injected externally. The accelerated electrons apparently came from the background plasma. The stimulated Raman scattering (SRS) instability was also reported to have been detected. SRS was given as the explanation for the boost in energy of the background electrons (100 ev) up to as much as 10 MeV. It is well known that SRS can produce high energy electrons from background plasma.[99] In the Osaka report, the electron trapping threshold was estimated to be about 2.4 MeV, maximum energy gain was 11 MeV, and acceleration distance was about 3 mm. In order to attain energies up to 20 MeV, the report suggested that multiple stage acceleration may have occurred.

First we examine the energy evolution and acceleration distance of an electron injected at the bottom (zero phase) of the plasma wave's potential. Our calculations show that the trapping threshold for a $\epsilon \approx 3\%$, $\gamma_p \approx 9.86\%$ plasma wave is $\gamma \approx 3.53$ (1.26 MeV) as shown in Table D.1. The values in Table D.1 were obtain using equations 2.2 and 2.3 of Chapter 2. Note that the Osaka report states that the trapping threshold is 2.4 MeV. We will examine both 1.3 MeV (an energy slightly greater than our calculated threshold) and 2.4 MeV electrons in order to cover both cases. Our Figure D.1(a) shows the energy versus acceleration distance for the 1.3 and 2.4 MeV electrons. Notice that as the injection energy increases, the maximum energy and distance to reach that energy decrease. The figure shows that a 1.3 MeV (or 2.4 MeV) electron would reach an energy of 3.5 Mev (or 4.2 MeV) in the Osaka experiment's 3 mm acceleration distance. To reach the Osaka experiment's 11 Mev energy, would require a 1.3 MeV to be accelerated for 20.5 mm, much longer than the Osaka plasma wave. A 2.4 MeV electron would not reach 11 MeV at all, and likewise for any electron with initial energy greater than 2.4 MeV, and injected at zero phase.

Next we consider electrons injected at all phases in the plasma wave, and the possibility of multistage acceleration. Depending on their injection phases, some electrons can be accelerated to higher energies than the electron injected at zero phase. Figure D.1(b) shows energies of electrons after 3 mm of acceleration versus initial phase of injection in the plasma wave. The heavy line at the bottom of the graph represents electron energies at the end of the first stage of acceleration for the electron injected with 1.3 MeV. The thin dotted line at the bottom represents the same for electrons injected with 2.4 MeV. The series of seven heavy (or dotted)

	γ		MeV	
n_1/n_0	Min	Max	Min	Max
0.01	5.35	18.2	2.18	8.6
0.02	4.22	23.2	1.61	11.1
0.03	3.56	27.8	1.28	13.4
0.04	3.10	32.2	1.05	15.6
0.05	2.76	36.1	0.88	17.7
0.06	2.50	40.5	0.75	19.7
0.07	2.29	44.5	0.64	21.8
0.08	2.12	48.6	0.56	23.8
0.09	1.98	52.6	0.49	25.8
0.10	1.86	56.6	0.43	27.8
0.11	1.75	60.6	0.38	29.8
0.12	1.67	64.5	0.33	31.8
0.13	1.60	68.5	0.30	33.7
0.14	1.53	72.4	0.26	35.7
0.15	1.47	76.3	0.23	37.7
0.16	1.41	80.3	0.21	39.6
0.17	1.37	84.2	0.18	41.6
0.18	1.32	88.1	0.16	43.5
0.19	1.29	92.0	0.14	45.5
0.20	1.26	95.9	0.13	47.5

Table D.1: Trapping threshold and maximum energy for the Osaka University experiment given in γ and MeV units (9.569 and 10.591 μm CO_2 lasers, $\gamma_p = 9.86$).

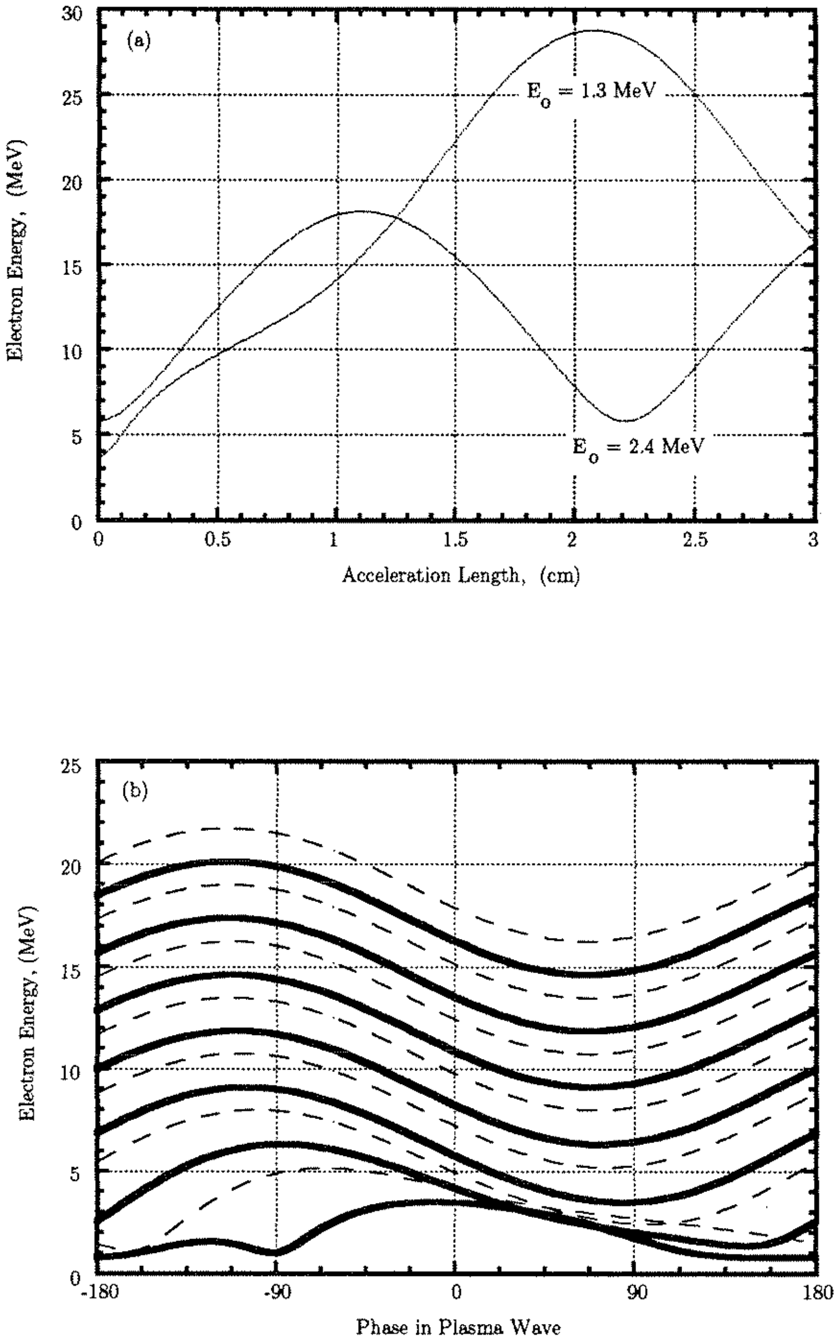

Figure D.1: Electron energy gain in the Osaka University beatwave acceleration experiment. (a) Energy versus distance and (b) energy gain for seven stages of acceleration.

lines represents the energies of electrons at the end of seven acceleration stages for initially 1.3 MeV (or 2.4 MeV) electrons. The peak energy at the end of the first stage is used as the injection energy for the second stage. The peak energy of each subsequent stage is the injection energy for the next stage up the series. Although the peak energy at the end of one stage occurs at a single phase, that energy is the injection energy for all the electrons between -180 and +180 degrees for the next stage. Figure D.1(b) shows that about 4 plasma wave stages covering about 12 mm are required to accelerate some of the electrons having threshold energy to about 10 MeV. About four stages are required to accelerate 10 MeV to 20 MeV. Even if staging could occur, the length of plasma wave required is much longer than the 3 mm measured in the Osaka experiment. The Osaka report said that about 11 MeV is gained per stage, but we found that only 3 to 4 MeV is gained per 3 mm stage. Based on this one-dimensional study, it appears that a $\epsilon \approx 3\%$, $\gamma_p \approx 10$, and 3 mm long plasma wave could not accelerate electrons from threshold to 10 MeV or from 10 MeV to 20 MeV.